MASTER

Robust spectral analysis of heart rate variability in non-invasive fetal ECG recordings

Warmerdam, G.J.J.

Award date:
2012

Technische Universiteit
Eindhoven
University of Technology

máxima
medisch centrum

Robust spectral analysis of heart rate variability in non-invasive fetal ECG recordings

Master Thesis
G.J.J. Warmerdam

August 24, 2012

Supervisors:
Dr.Ir. C. Van Pul
Dr.Ir. R. Vullings
Prof.Dr.Ir. P.F.F. Wijn

Author:
Guy Warmerdam

Abstract

In obstetrician units timely recognition of fetal distress is a great challenge. At present, cardiotocography is the widespread method for fetal monitoring. Unfortunately, the poor specificity of cardiotocography has led to an increase in unnecessary operative deliveries without improvement on the fetal outcome. Although additional techniques have been developed for fetal monitoring during labor, these techniques have only shown limited diagnostic value. Therefore, an urgent need exists to develop non-invasive techniques that provide complementary information on fetal wellbeing.

Besides techniques that are used in clinical practice, additional information might be provided by spectral analysis of the fetal heart rate variability. The heart rate variability is under control of the autonomic nervous system and, hence, is expected to reflect the modulation of the autonomic nervous system. To ensure accurate and reliable spectral analysis, the heart rate needs to be measured on a beat-to-beat basis. A technique that enables beat-to-beat recording of the fetal heart rate throughout the pregnancy is the non-invasive fetal ECG. To record the fetal ECG non-invasively, a monitoring system was developed at the Maxima Medical Center in collaboration with the Eindhoven University of Technology. However, the non-invasive recordings are severely contaminated with noise and reliable extraction of the fetal ECG is difficult. Despite numerous improvements in signal processing techniques, currently, no algorithm exists that allows for reliable automated extraction of the fetal heart rate from abdominal recordings.

In this thesis, an algorithm is developed that enables for automated extraction of the fetal heart rate in non-invasive fetal ECG recordings. For this purpose, the state-of-the-art techniques are evaluated and the best performing techniques are selected. The limitations of the existing techniques are overcome by newly developed implementations of these techniques and the development of additional processing techniques. All individual techniques are combined into a single algorithm that enables for reliable extraction of the fetal heart rate.

The performance of the developed algorithm is compared to state-of-the-art techniques and is evaluated based on manual annotation. Due to the improvements of the technique that is used to enhance the fetal ECG, the median (range: 5-95%) Signal-To-Noise-Ratio has increased from 8.2 (range: -6.0-18.3) to 12.3 (range: 3.6-20.6). Furthermore, the algorithm is able to distinguish between reliable and unreliable fetal ECG recordings, and the error rate for recordings with a reliable fetal ECG has

decreased from 17.2% to 6.5%.

Before spectral parameters can be used as diagnostic values, the development of spectral parameters should be examined in healthy fetuses throughout the pregnancy. The developed algorithm is used to obtain spectral parameters of the fetal heart rate variability in a longitudinal follow up study to investigate maturation of the autonomic nervous system in healthy fetuses. In comparison to previous studies of our group that used the same database, the percentage of measurements from which fetal heart rate is extracted for spectral analysis has increased from 16% to 44%. Due to the increase in usable fetal heart rate for spectral analysis, clear trends can be observed in the obtained spectral parameters. The observed changes in spectral parameters are in accordance with those seen in animal studies.

Acknowledgements

I would like to thank everyone who helped me during my graduation project. First of all, I would like to thank my supervisors Dr.Ir. Carola Van Pul, Dr.Ir. Rik Vullings, and Prof.Dr.Ir. Pieter Wijn. Carola, without your help I would have not been able to graduate this August. You have always kept an eye out for what was best for me and my graduation project, and made sure I started writing this report in time. A special thanks also to Rik, who has taken the time and effort to help me with all of my questions. What you explained to me in just a few minutes helped me do the work that would otherwise have taken me a week. In particular I would like to thank Pieter Wijn. Throughout my entire master you have given me great advise on choices concerning my education and future career. Not only have you introduced me into the interesting field of medical physics, you have always shown trust in me. Thank you for your advice and support.

Besides my supervisors, I would like to thank (almost Dr.) Judith Van Laar. Judith, I have enjoyed working with you and I am glad everything worked out with Florian and your PhD. You have given my work a direct clinical meaning. In this regard, I would also like to thank Dr. Peter Andriessen and Prof.Dr. Guid Oei for their contribution on the clinical aspect of my graduation project. Furthermore, I would like to thank Ir. Michiel Rooijakkers and Dr.Ir. Chris Peters who have both let me use their work and helped me with the implementation of certain algorithms.

Last but not least, I would like to thank my family and friends. In particular I would like to thank my parents for all their interest in my work and the support they have given me throughout my entire education. Furthermore thanks to my sister, who never stopped inviting me and whom I am definitely going to bother more often with my presence. Finally, I would like to thank my girlfriend Chantal. Chan, thank you for your love and patience, and for giving me the time I needed to finish my graduation report. I know I have always been able to rely on you and that has been a great mental support. With our trip to Africa and our moving in together, we have an exciting time ahead of us!

Contents

Chapter 1

Introduction

One of the great challenges for obstetrician units these days is to recognize fetal distress during labor. In this critical period, the fetus is exposed to temporal hypoxia, a deficiency of oxygen, caused by uterine contractions. Generally, a healthy fetus is capable of handling this kind of stress and will develop normally [1]. In contrast, an unhealthy fetus might be inadequate to respond and the risk of neonatal morbidity and mortality for this group is significant [2–4]. Additionally, the timing of medical interventions is of vital importance. On the one hand, unnecessary interventions result in unnecessary pre-term birth and can lead to infant death [5]. On the other hand, late or no intervention may cause fetal metabolic acidosis, a low acid-base status (pH value) in the tissue, that is also associated with severe brain damage [3,6]. The main goal in fetal monitoring is to aid obstetricians in their decision making.

1.1 Fetal monitoring

The introduction of cardiotocography (CTG) in the 1960s, has enabled continuously monitoring of the fetal heart and uterine contractions. This simultaneous monitoring allows for interpretation of variations in the fetal heart rate based on the stress experienced by a fetus during a contraction. An example of such a measurement is shown in Fig. 1.1. In current obstetrical units, CTG has become the worldwide standard for fetal monitoring during labor. However, the use of CTG appears to have limited diagnostic value [7]. Since the interpretation of the CTG is based on visual pattern recognition, the inter- and intra-observer variability is high [8]. Furthermore, despite its high sensitivity, its specificity is rather poor (30-40%) [7]. The use of CTG has even resulted in an increased rate of unnecessary operative interventions, without a noticeable improvement on the fetal outcome [7]. For these reasons, CTG requires diagnostic tests to be additionally performed in case of CTG abnormalities. To provide this extra information, fetal scalp blood sampling (FBS) and STAN (Neoventa Medical, Gothenburg, Sweden) [9] have been introduced in the clinic.

FBS measures the pH value of a blood sample, obtained from the fetal scalp during labor. This invasive method requires rupture of the fetal membranes (reported

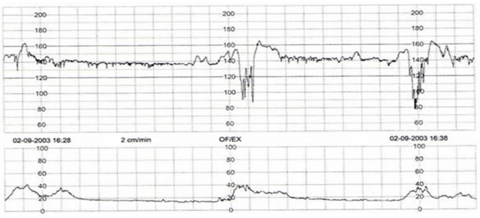

Figure 1.1 – *Example of a cardiotocogram. Upper line: fetal heart rate. Lower line: uterine contractions.*

with an overall incidence of complication of 6% [10]) and the blood sample can be contaminated with maternal blood or amniotic fluid. Furthermore, it only provides instantaneous information and needs to be repeated in case of persisting CTG abnormalities. With regard to the implementation of FBS, some clinical studies have reported a reduction in unnecessary interventions [10], but the evidence for this is not undisputed [11]. Besides, other studies did not show an improvement in fetal outcome [7].

Besides the pH value obtained from FBS, additional information might also be obtained from the fetal electrocardiogram (ECG). The ECG provides information about the electrical activity of the heart during a cardiac contraction and several studies have associated changes in the shape of the ECG waveform with hypoxia [12–16]. As an alternative to the instantaneous information provided by the FBS technique, STAN continuously monitors changes in the fetal ECG (fECG). More specifically, STAN analysis changes in the ST-segment, the part of the ECG that is associated with relaxation of the cardiac muscle. Since STAN invasively records the fECG by a single electrode attached to the fetal scalp, it can only be used during labor.

A recent meta-analysis showed that CTG in combination with STAN reduced the number of operative vaginal deliveries and the requirement for FBS [17]. Despite these improvements, no significant difference was seen in the rate of severe metabolic acidosis at birth, the number of caesarean sections or the neonatal outcome [17]. Furthermore, it cannot be used adequately in clinical practice without the availability of FBS [18]. The fact that ST-events occur at a similar frequency for normal and abnormal CTG patterns [19] further emphasizes the need for additional information.

Besides fetal blood pH values and ECG waveform analysis, more information might be gained from fetal heart rate variability (HRV). For the interpretation of the CTG, the fetal HRV has already been reported to be an important parameter [20–23]. The fetal heart rate is controlled by the cardiac regulation of the autonomic nervous system (ANS) [24, 25]. A normal fetal HRV is indicative for fetal well-being [21], whereas decreased fetal HRV is associated with low pH value [26], low Apgar score [27] and perinatal death [21, 22].

To quantify these changes in HRV, spectral analysis might provide a more objective classification compared to the visual pattern recognition in the interpretation of the CTG. Recent studies have already shown that spectral parameters of the HRV are correlated with severe metabolic acidosis at birth [28] and might be indicative for fetal distress in an early stage of labor [29].

Before spectral analysis can be used as a diagnostic tool for fetal monitoring, more insight needs to be gained in normal development of the ANS. At present, limited research has been done on fetal HRV in the frequency domain during the second and third trimester of the pregnancy, the period in which the autonomic cardiac control system develops [30–32]. In these studies an increase is seen in the overall frequency power of the fetal HRV with gestational age (GA). This increase is thought to be a result of ANS maturation [30, 31]. However, the studies are in disagreement concerning changes in the spectral parameters of the HRV. This can be explained from the fact that only absolute frequency power spectra were investigated and fetal rest-activity cycles [33], associated with typical fetal heart rate patterns [31,34], were not distinguished.

1.2 Non-invasive fetal heart rate recording

To perform spectral analysis on the fetal heart rate, the methods for spectral analysis are subject to certain criteria. Firstly, the fetal heart rate recordings should be obtained non-invasively, allowing for measurement throughout the entire pregnancy. Secondly, the heart rate needs to be measured on a beat-to-beat basis to ensure accurate and reliable spectral analysis [35, 36]. Currently, Doppler ultrasound (US), the magnetocardiogram (MCG) [37, 38] and the fECG [39, 40] are the most important methods to determine the heart rate non-invasively. Of these methods, US is already widely used in clinical practice [41]. Unfortunately, US is unsuited for frequency analysis because the heart rate is averaged over 2.5 seconds. This in particular obscures the high frequency parameters [42]. Furthermore, US cannot be used for prolonged measurements since this technique transmits energy into the fetal body, potentially endangering the fetal health.

Recordings of the fetal MCG and ECG both have the possibility to measure the heart rate on a beat-to-beat basis and have the potential to provide a fetal cardiogram for a morphological analysis [43]. ECG measure the electric activity of the fetal heart on the skin and MCG measures the magnetic fields generated by the electric currents within the fetal heart [43]. The main advantage of using the magnetic over the electric signals is that it does not suffer from the isolating effect of the vernix caseosa, an isolating layer surrounding the fetus that forms between the 28th and 32 week of GA [44, 45]. However, MCG requires a heavy magnetically shielded room [43] and cannot easily be used in clinical practice. In contrast to MCG, the measurement of the ECG only needs a small recording device [46], making it most suited for longitudinal studies and perhaps even for usage outside a clinical environment [46, 47].

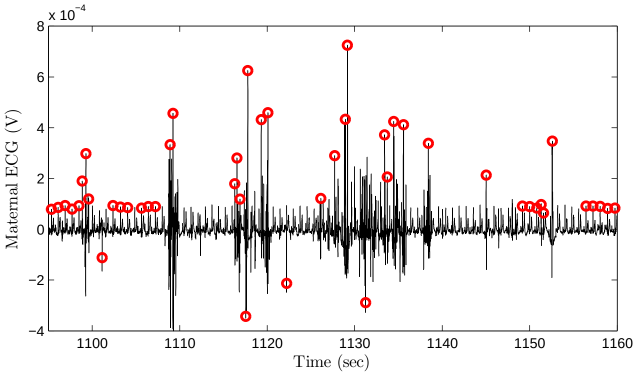

Figure 1.2 – *Example of an abdominal recording that is severely contaminated by artifacts. The (at times incorrectly) detected mECG complexes are displayed in red circles. Note, that the artifacts already disturbs detection of the relatively large maternal ECG and this disturbance will be even more prominent for the fECG detection.*

The non-invasive ECG recordings used throughout this thesis are obtained from electrodes attached to the abdominal surface. The monitoring system is called Non-invasive Electrophysiological Monitor for Obstetrics (NEMO) and was developed at the Maxima Medical Center (MMC), in collaboration with the Eindhoven University of Technology (TU/e) and Maastricht Instruments BV. From these recordings, it is not possible to extract the fECG information directly, due to strong contamination by unwanted electrical signals and low Signal-To-Noise-Ratio (SNR) of the fECG complexes. Ever since the initial development of the NEMO, numerous improvements have been made regarding artifact reduction [48], SNR [49], and correct detection of the ECG-complexes [50, 51].

Despite these efforts, there is still a relatively large percentage of falsely detected ECGs [49]. The reason for this is that current ECG detection methods assume that the ECG signal is detectable at all times. Although this assumption is reasonable in thoracic recordings, this is different for abdominal recordings. The latter are often contaminated with large amplitude artifacts that even exceed the maternal ECG (mECG) amplitude (Fig. 1.2). This is even more the case for fECG detection, since the noise amplitude is of the same order of magnitude as the fECG amplitude. Hence, the fECG will often be overshadowed by artifacts, in which case no reliable heart rate data can be obtained. Furthermore, part of the recordings does not contain any measurable fECG information because the electric signal produced by the fetal heart is to weak to reach the abdominal surface, either due to immaturity of the heart or the presence of the vernix caseosa.

1.3 Goals of this thesis

The first goal of this thesis is to optimize all signal processing techniques that aim to extract fetal heart rate from non-invasive fECG recordings. Secondly, the individual techniques have to be combined into a single algorithm that enables automated extraction of the fetal heart rate information. This algorithm should be able to distinguish between usable signal and signal that is severely contaminated by artifacts or signal in which the fECG is virtually absent. The final goal is to obtain spectral parameters in a large follow-up study group to investigate maturation effects of the ANS on the fetal HRV.

Chapter 2

Physiological background

Before explaining the details of the signal processing techniques used for the extraction of the fetal heart rate this section covers the basic physiological background of the origin of the ECG signal. Besides a brief introduction in the physiology of the heart, this section also provides information on the physiological principles behind the heart rate regulation.

2.1 Adult heart

The heart functions as a pump to provide all vital organs and peripheral tissue with blood. The cardiovascular system in human adults consists of two parts, the pulmonary and the systemic circulation. In the pulmonary circulation, oxygen-depleted blood is pumped from the right side of the heart into the pulmonary arteries, to the lungs. The oxygenated blood is then returned back to the left size of the heart via the pulmonary veins. In the systemic circulation, oxygenated blood is pumped from the left side of the heart into the aorta, through the peripheral organs, and returns depleted blood to the right side of the heart via the vena cava [52, 53] (Fig. 2.1a). Each side of the heart consists of two chambers, the atrium and the ventricle. The function of the atrium is to regulate the blood flow into the ventricle. In its turn, the ventricle is the main pump and has to supply sufficient pressure for the blood to flow, either through the pulmonary or the systemic circulation [52, 53]. Since the systemic circulation is larger than the pulmonary circulation, the left ventricle has to generate a larger pressure and requires a larger muscular mass compared to the right ventricle.

The contraction of the heart is regulated by a specialized nervous system that conducts electrical impulses (action potentials) rapidly throughout the myocardium, the muscular layer of the heart [52], as shown in Fig. 2.1b. This system functions such that the atrial contraction takes place prior to the ventricular contraction. This ensures that the ventricles are entirely filled before they thrust the blood into the aorta or pulmonary arteries. Secondly, to optimize the effective pressure generated by the ventricular contraction, all parts of the ventricles need to contract almost simultaneously.

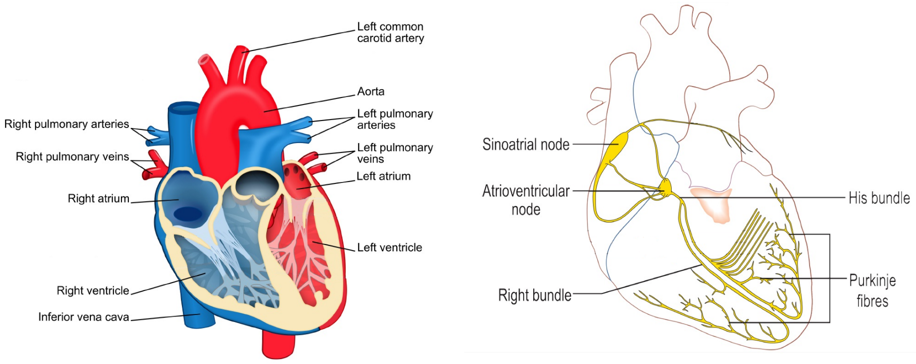

(a) (b)

Figure 2.1 – *(a) Schematic representation of an adult heart. (b) Electric conduction system of the heart.*

The impulses that cause cardiac contractions are generated by self-excitation of the cardiac muscle cells. In theory, because all of these cells are capable of self-excitation, any cardiac muscle cell can initiate a contraction. Of these cells, the pacemaker cells, located in the sinoatrial (SA) node, have the highest self-excitation rate and, hence, determine the heart rate [52]. After each excitation, the cells exhibit a refractory period, in which no new impulses can be generated or propagated.

The action potentials generated in the SA-node first propagate through both atria, causing them to contract. Before the ventricles contract, the central fibrous body, tissue located between the atria and the ventricles, prevents the direct spread of the action potentials into the ventricles. This oblies the propagation of the action potentials to proceed through the atrioventricular (AV) node, into the bundle of His [53]. The delay in propagation caused by the AV node and the bundle of His, allows the atria to empty their content into the ventricles, before ventricular contraction occurs. After the bundle of His, the nerve fibers split into left and right bundle branches and continue towards the left and right ventricle respectively [52, 53]. Finally, these bundle branches break down into the Purkinje fibres that connect to the cardiac muscle cells in the ventricles. To produce maximal effective pressure during ventricular contraction, the action potentials have to reach the cardiac muscle cells simultaneously. For this purpose, the Purkinje fibers are relatively large compared to the cardiac muscle fibers and the action potentials are transmitted at approximately six times the transmission velocity of the transmission through the cardiac muscle fibers [52].

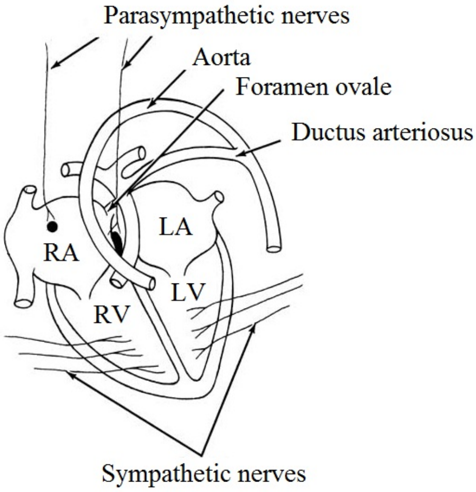

Figure 2.2 – *Schematic representation of a fetal heart. Foramen ovale and ductus arteriosus are indicated. Also the connections of the parasympathetic (vagus nerves) and sympathetic nerve system to the fetal heart are indicated.*

2.2 Fetal heart

The fetal cardiovascular circulation differs from the adult circulation [54–56]. In contrast to adults, the intake of oxygen and the secretion of carbon-dioxide does not takes place in the lungs, but in the placenta [57]. In this case, the blood from the right ventricle is not pumped into the lungs to acquire oxygen and instead both ventricles pump the blood through the entire body (including the lungs) [58]. For this purpose, two interconnections, the foramen ovale and the ductus arteriosus, link the atria and the outgoing arteries of both the ventricles [57], as illustrated in Fig. 2.2. Since both the left and right ventricle have to generate equal pressure, their muscular mass is approximately equal. Often, the mass of the right ventricle is even slightly larger [54,56]. Despite these differences in mechanical function between the adult and fetal heart, the fetal nervous system causing the propagation of the action potentials is rather similar to that of adults.

2.3 Electric activity

The membrane of cardiac muscle cells exhibits a potential difference between intracellular and extracellular fluid, mainly controlled by the distributions of Sodium (Na^+), Potassium (K^+) and Calcium (Ca^{2+}) ions [52, 53]. At rest, the membrane potential is -90mV with respect to the extracellular fluid. The presence of an action potential can increase the membrane potential up to -60mV, initiating a cycle to activate the cell. The membrane potential as a function of time during such a cycle is

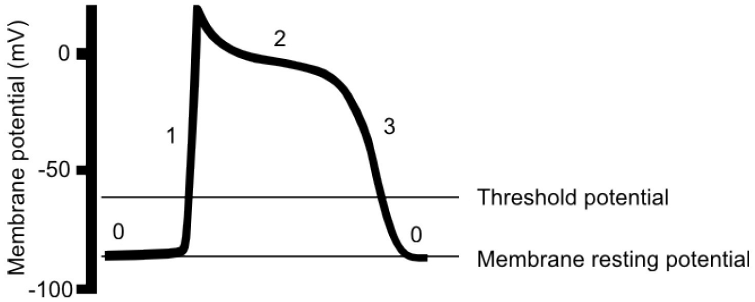

Figure 2.3 – *The membrane potential versus time during cell depolarization and repolarization. The membrane potential is initially at rest of -90 mV (0). By the presence of an action potential the membrane potential increases to above a threshold potential of -60 mV, followed by depolarization (1). After depolarization, the membrane potential initially remains at a plateau (2) and finally repolarizes to rest membrane potential (3). [59]*

shown in Fig. 2.3. At first, the increased membrane potential will increase the Na^+ permeability through the cell membrane. This generates a rapid influx of Na^+ that inverses the membrane potential (*depolarization*). Besides an increased Na^+ permeability, also a more graduate inflow of Ca^{2+} and an outflow of K^+ takes place. The exchange of Ca^{2+} and K^+ causes the membrane potential to remain at a plateau. Finally, the membrane potential returns to its rest value due to persisting outflow of the K^+ (*repolarization*). When the cell has returned to its rest phase, the Na^+ ions will leave the cell, while the K^+ ions re-enter.

The actions potentials are able to propagate from cell to cell during the depolarization phase [60]. There are two mechanisms at hand that enable this intercellular propagation. Firstly, gap-junctions, interconnections between the cardiac muscle cells, provide channels for the transportation of positive ions from the activated cell to adjacent rest cells. Secondly, the depolarization of a cell will locally lower the concentration of positive ions in the extracellular fluid. Both these mechanisms lower the membrane potential of the neighboring rest cells and initiate the depolarization in these cells. As a consequence of this cell-to-cell activation, the stimulus is able to propagate in any given direction and creates activation waves. At the wavefront, the depolarized cells will have an increased potential compared to the rest cells and the boundary between these cells will act as a dipole.

The actual contraction of the cardiac muscle originates from the conversion of an action potential into mechanical activity inside the cardiac muscle cells [53]. First, the action potential causes a chemical process to release large amounts of Ca^{2+} ions. In turn, the large concentration of Ca^{2+} ions initiates an attractive force inside the cardiac muscle cell, causing it to contract.

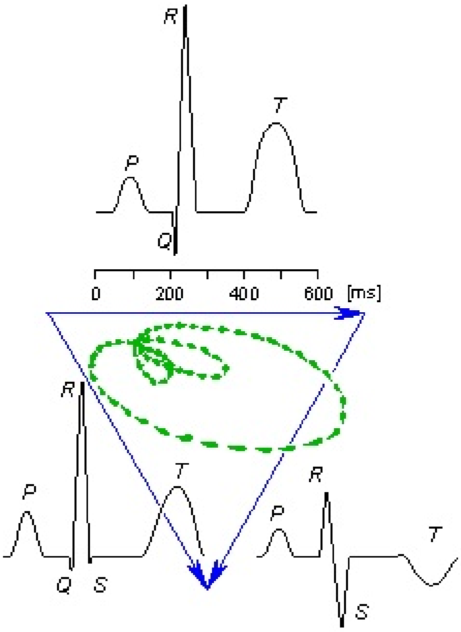

Figure 2.4 – *The VCG is shown in green. The biggest loop represents the QRS complex, and the two smaller loops the P and T wave. The ECG obtained by projection of the VCG onto the leads of the traditional Einthoven triangle [65] are displayed in black. [63]*

2.4 The vectorcardiogram

The tissue surrounding the cardiac muscle acts as a conductor, allowing for a spread of the electrical currents generates by the individual dipoles. The coherent activation of numerous cells at the dipole wavefront will generate electrical fields that, due to the impedance of the skin, result in measurable potential differences at the body surface [61]. In a first order approximation, the entire electrical activity can be described by a single field vector [62,63] and the time path of this vector in three-dimensional space is called the vectorcardiogram (VCG) [64].

The characteristic VCG of an adult consists of three closed loops, as displayed in Fig. 2.4 [66]. The first loop is associated with atrial depolarization, followed by the largest loop which is associated with ventricular depolarization. Since atrial repolarization and ventricular depolarization occur simultaneously, the atrial repolarization is obscured. The third loop is associated with repolarization of the ventricles. The repolarization wave of the ventricles propagates in opposite direction compared to its depolarization wave and has inverted sign. Therefore, the associated path is oriented in similar direction as the depolarization loop of the ventricles. The maximum amplitude of the VCG is seen during the ventricular depolarization because the largest simultaneous activation of the muscles fibers is involved in the ventricular contrac-

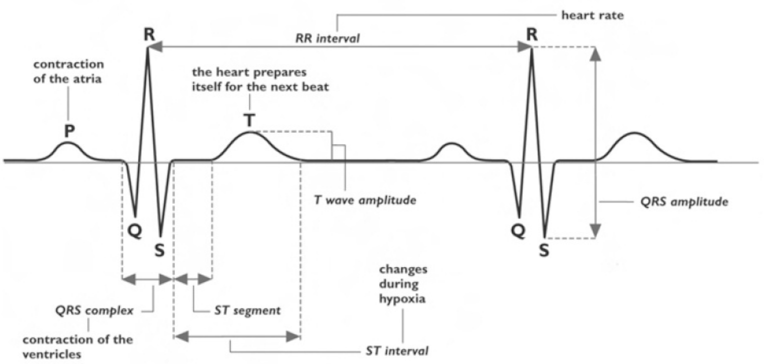

Figure 2.5 – *If the amplitude of the VCG at a particular point in time is positive in the direction of the lead vector the recording will be positive and visa versa. The amplitude is also correlated with the amplitude on the recording.*

tion. The electrical axis of the heart is then defined in the direction of the maximum amplitude of the VCG [52] and, for the adult heart, points towards the left ventricle. The VCG of the fetal heart looks slightly different due to the difference in mechanical function of the heart, as explained in section 2.2. Since the muscular mass of the right ventricle is larger than that of the left ventricle, the electrical axis points towards the right ventricle [50, 55].

2.5 The electrocardiogram

Despite its conceptual simplicity to visualize the activation of the myocardium, the VCG cannot be measured directly. The created potential differences, however, can be detected by means of electrodes on the skin. The representation of these potential differences as a function of time is called the electrocardiogram (ECG) [52]. The ECG can be regarded as a one-dimensional projection of the three-dimensional field vector (described by the VCG) onto the lead vector of two electrodes [63]. An example of the VCG projections onto the lead vectors of the traditional Einthoven triangle [65] is displayed in Fig. 2.4.

A typical ECG consists of a PQRST-complex [52,53], as schematically illustrated in Fig. 2.5. The initial wave, the P-wave, is associated with the depolarization of the atria (first loop in the VCG). This is followed by the QRS-complex caused by the depolarization of the ventricles and, finally, the T-wave that is associated with the repolarization of the ventricles [52, 53]. As mentioned in section 2.4, the repolarization of the atria occurs simultaneous with the depolarization of the ventricles and cannot be distinguished in the ECG. Furthermore, in the same manner as for the VCG, the T-wave will have the same polarity as the QRS-complex.

Before the fetal heart signal reaches the abdominal skin, the signal has to propagate through several layers of tissue, which together determine the overall conductivity [67]. Changes in composition of these layers throughout the gestation (e.g. increase in amniotic fluid [68, 69], placenta and fetal volume [70]) directly influence the overall conductivity. In particular the formation of the low conductive vernix caseosa layer, during the 28th and the 32th week of gestation [44, 45, 66], is expected to strongly attenuate the signal. This layer will slowly dissolve in the 37th week to the 38th week [58, 71].

2.6 Heart rate variability

The fetal response to oxygen deficiency and other changes in circumstances is under regulation of the autonomic nervous system (ANS), and entails several protective mechanisms [52]. The goal of these mechanisms is to maintain sufficient oxygen supply to the central organs.

The initial stage of oxygen deficiency is hypoxemia and the typical fetal response is to optimize oxygen uptake in the placenta. If oxygen deficiency persists, the fetal activity is reduced [1, 12]. In case of long-lasting hypoxemia the growth rate is reduced and the development of the organ system is affected. The fetus is able to handle hypoxemia for several weeks. In case the oxygen level further decreases, the fetus may enter the hypoxia state. In this state, vasoconstriction, the narrowing of the blood vessels, reduces the blood flow to peripheral tissue and the blood circulation is redistributed to the central organs [72–75]. In addition, the heart rate increases to maintain cardiac output and umbilical blood flow [75, 76] and anaerobic metabolism, the creation of energy through combustion of carbohydrates in the absence of oxygen, occurs in the peripheral tissue [72, 77, 78]. Finally, the fetus enters the state of asphyxia, in which metabolic acidosis and anaerobic metabolism might also occur in the central organs.

Throughout the pregnancy, the fetus develops mechanisms that protect the fetus against hypoxemia and hypoxia. The ability of the fetus to respond to the hypoxemia and hypoxia experienced during labor, strongly depends on the development of these protective mechanisms. If these mechanisms have already been used or have not been fully developed, e.g. due to long-lasting hypoxemia prior to labor, the risks of fetal morbidity and mortality are significant. The fetal heart rate variability (HRV) might provide information on the activity and development of the fetal ANS, and its ability to respond to the stress experienced during labor.

2.6.1 Autonomic cardiac control

The autonomic nervous system consists of two essentially different parts, the parasympathetic nervous system (PSNS) and the sympathetic nervous system (SNS) [79]. The stimulation of the PSNS has a direct effect on the heart rate and this allows for a beat-to-beat variation. This beat-to-beat variation is not possible for the relatively slow stimulation of the SNS. For this reason, high frequency fluctuations (0.15-1.5Hz) of the heart rate are solely associated with PSNS control, whereas low frequency fluctuations (0.04-0.15Hz) are associated with both PSNS and SNS control [25, 80].

Both the SNS and the PSNS are composed of preganglionic and postganglionic neurons. The cell bodies of the preganglionic neurons is located in the Central-Nervous-System (CNS) and they synapse, electrically connect, with the post ganglionic neurons that are located close to or are embedded in their target organs. The postganglionic neurons in turn, synapse with the effectors of the target organs [79].

The transmission of action potentials along the ganglia of the PSNS and SNS is governed by different neurotransmitters. For the PSNS both the transmission from the pre- to postganglionic neurons and the transmission from postganglionic nerves to the effectors of the target organ is governed by acetylcholine (ACh). In case of the SNS, the transmission from pre- to postganglionic nerves is also mediated by ACh, however, now the activation of the target synapse is mediated by either noradrenaline or adrenaline.

The postganglionic cells of the PSNS used in cardiac regulation are located either on the epicardial surface, the outer surface of the heart, or within the walls of the heart. Most of their associated cardiac target cells are located near the SA node and the AV node (Fig. 2.2). The activation of the PSNS has a direct effect on the heart rate. The ACh, the neurotransmitter used for propagation from PSNS postganglionic cells to its target cells, directly influences the permeability of K^+ ions in the membranes of the cardiac cells. Furthermore, the effect of PSNS stimulation decays relatively quick because the SA and AV node are rich in cholinesterase, an enzyme that breaks down ACh. This direct control mechanism enables the PSNS to exert a beat-to-beat control on the heart rate.

The pre- and postganglionic nerves of the SNS synapse in the stellate ganglia, in front of the neck of the first rib. The postganglionic fibers are distributed to the various chambers of the heart (Fig. 2.2). Activation of the SNS increases the myocardial contractility and the heart rate [81].

In comparison to the rapid decay and stimulation due to parasympathetic activation, the effect of sympathetic activation is slow. The release of norepinephrine, the neurotransmitter involved in activation of the SNS target cells, is relatively slow and the effect of the norepinephrine on the cardiac cells is indirect. Additionally, the decay of the sympathetic activity is also relatively slow, since the concentration of norepinephrine is only reduced by either absorption in the target nerve terminals or by the blood stream.

2.6.2 Changes in fetal autonomic regulation due to maturation

The contributions of the PSNS and the SNS to the cardiovascular control change throughout the pregnancy due to the maturation of the fetal ANS [30–32]. Early in the pregnancy, the heart has not yet been fully developed and the heart rate is autoregulated [82, 83]. In sheep studies, it has been shown that the cardiac SNS becomes functional prior to the PSNS [84,85] and the SNS is expected to dominate the control of the cardiovascular functions while the fetus is inside the uterus.

Besides the effect of maturation on the heart rate regulation, fetal activity also influences the heart rate. Whereas spontaneous body movement can be observed randomly over time from 7 weeks of gestation [86], these fetal movements become clustered in rest-activity cycles from 23 weeks of gestation onwards [33]. During the second half of the pregnancy, rest-activity episodes become increasingly associated with fetal heart rate patterns and eye movements, and eventually result in behavioral states. After 34 weeks of gestation, these behavioral states are fully developed [87] and their presence is seen as an indication of maturity of the ANS [88].

Behavioral states are commonly classified into four groups [89]. The first state (1F) is the quiet sleep, or non-REM sleep. In this stage, no body or eye movements occur and the fetal heart rate is stable with a relatively small oscillation bandwidth. The second state (2F) is active sleep, or REM-sleep, in which repeated body movements and continues eye movements are present. The heart rate pattern now shows large fluctuations under influence of rapid changes in ANS activity. The final two states, the quiet awake (3F) and the active awake (4F), are of less importance since they seldom occur [90, 91] and will not further be discussed.

2.7 Summary

In this chapter, the physiological background of the fetal heart and the electrical cardiac activity have been discussed. In the next chapter, state-of-the-art signal processing techniques are discussed that exploit these physiological properties to extract the fetal heart rate from non-invasive abdominal recordings.

Chapter 3

Technical background

The abdominal recordings are strongly contaminated by unwanted electrical signals, such as the mECG, the electrical activity of the abdominal muscles and uterus, power line interference, and noise. The low amplitude of the fECG with respect to amplitude of these disturbances makes the extraction of the fECG difficult.

Of the interferences in the abdominal recordings, the dominant interference is the mECG. The separation of the mECG and the fECG is the first important signal processing step. The separated fECG still contains other corruptions and, due to the small amplitude of the fECG, the SNR is often insufficient for direct extraction of the fECG [92,93]. Therefore, additional processing steps are required to enhance the SNR. This chapter explains the state-of-the-art processing techniques that concern extraction of the fECG from the abdominal recordings [48–51] and their limitations.

3.1 Maternal ECG subtraction

In the literature, several techniques have been proposed for suppression of the mECG from abdominal recordings, as briefly summarized in [48]. The majority of these techniques uses a template, an estimation of a mECG complex that can vary in time. This template is used to subtract the mECG from the recordings. However, for these template subtraction techniques, correct estimation of the mECG is important. Inaccuracies in the template result in residuals of the mECG in the recordings that easily exceed the amplitude of the fECG.

The challenge for these template subtraction methods lies in correct estimation of the strong variations in the waveform of the mECG. Respiration of the mother causes motion of the maternal abdomen and the orientation of the lead vectors of the electrodes relative to the cardiac electric field vary over time. This results in variations in the typical waveform of the ECG.

In the technique called Weighted Averaging of mECG Segments (WAMES) [48], a mECG template is generated for each individual wave (the P-, QRS-, and T-wave). By generating a template for the individual waves, the morphological variability can be accounted for more accurately. Furthermore, the accuracy of template subtraction

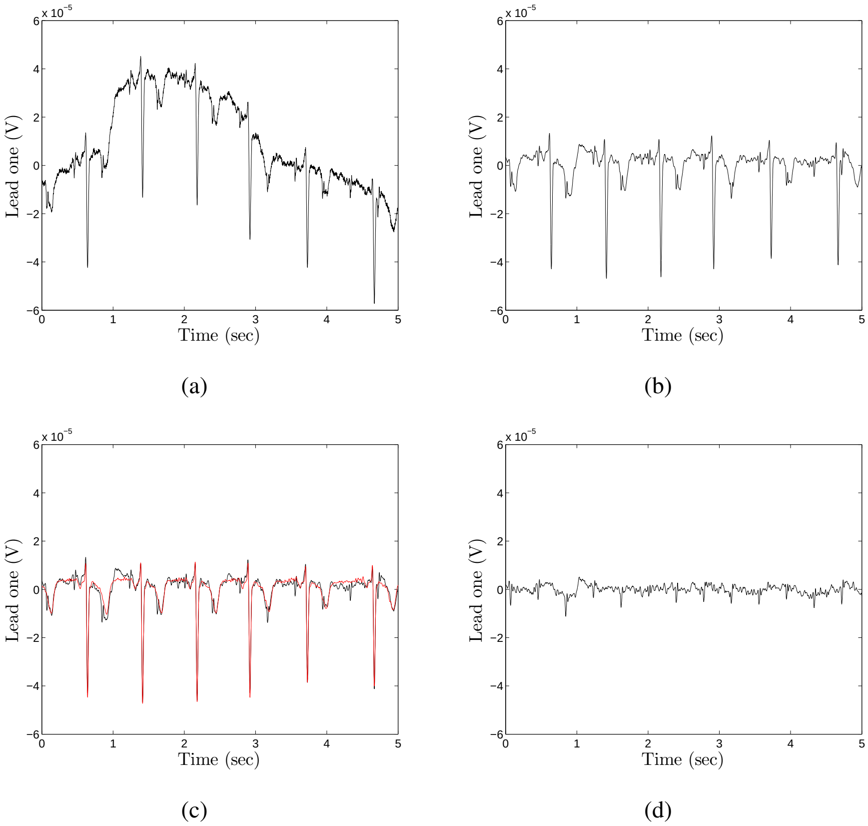

(a) (b)

(c) (d)

Figure 3.1 – *The subtraction of the mECG from the abdominal recordings by WAMES. (a) The raw abdominal recording. (b) Abdominal recording after pre-processing by means of linear filtering. (c) Pre-processed abdominal recording (black) and estimated mECG (red). (d) Remaining fECG after maternal subtraction.*

often suffers from artifacts and the presence of fECG complexes. For this purpose, WAMES only includes preceding waves in the averaging that are not contaminated with artifacts. An example of the mECG suppression by WAMES is shown in Fig 3.1.

WAMES has been shown to be superior to other existing techniques and is chosen as the method for the subtraction of the mECG throughout this thesis [48]. It is important to note that since the publication of the algorithm, a newer version has become available that is less computationally complex. Although this is not part of the work done in this thesis, the description of WAMES is discussed in more detail in the next section and slightly differs from the description in [48].

WAMES

In the first step of the mECG subtraction, other unwanted interferences are suppressed by filtering. First, the power line interference (50 Hz) is filtered by means of a fourth order Butterworth band-stop filter with stop-band between 49 and 51 Hz. The low frequency motion artifacts are suppressed by a fourth order Butterworth high-pass filter with cutoff frequency of 1.5 Hz. Finally, a fourth order Butterworth low-pass filter with cutoff frequency of 70 Hz is used to suppress higher harmonics of the power-line interference and part of the noise that originates from muscular activity. The low-pass cutoff value is chosen equal to the upper limit of the spectral content of the fECG [94].

The next step in the WAMES algorithm is to dynamically estimate a template of the mECG. In the template, each individual wave Z_i (with $Z = \{P, QRS, T\}$) is estimated individually by the weighted averaging of the waves of n preceding mECG complexes (Z_{i-k}). Before the averaging, the mECG complexes are synchronized based on their R-peak location. Since the R-peak has the highest amplitude in the ECG-complex, it is easiest to detect.

First, the part of the signal at the location of the new mECG complex is determined based on the R-peak location. Note that, besides the mECG complex Z_i, this part also contains disturbances from noise and the fECG. The goal is to only subtract complex Z_i from the recording.

A sanity check is then performed for each preceding mECG complex Z_{i-k}, to determine wether it is not too severely corrupted by noise. This is done by calculation of the mean difference between Z_{i-k} and the newly found Z_i

$$D_k = \overline{(Z_i - Z_{i-k})^2} \tag{3.1}$$

If a waveform of Z_{i-k} strongly deviates from the new complex, it is excluded from further estimation of the template.

After these strongly corrupted complexes have been excluded, an initial estimate of Z_i is obtained (Z_{ave}), defined as the average of the remaining preceding complexes. This allows for the detection of possible artifact samples within the new complexes Z_i. Artifact samples are identified with the Mean Squared Error (MSE) between Z_i and the average Z_{ave}

$$E(j) = \frac{1}{M}\sum_{j}^{M}(Z_{i,j} - Z_{ave,j})^2 \tag{3.2}$$

where $E(j)$ is the MSE in the j^{th} sample and M the length of wave. If the error of a sample j exceeds 1.5 times the mean error, that sample is indicated as an artifact and is not taken into account for further calculation.

Besides artifacts in the preceding complexes and within the new complex, respiration causes changes in the DC component and amplitude of Z_i with respect to the

DC component and amplitude of Z_{i-k}. Correct estimation of the mECG is further limited by the finite sampling frequency. As a solution to this problem, time-shifts smaller than this frequency are compensated for by interpolation. For these reasons, the initial estimate Z_{ave} has to be scaled (a), time-shifted (b), and DC offset compensated (c). The optimized waves Z_{temp} is found by minimizing the MSE between Z_i and Z_{ave}, with respect to the parameters a,b, and c:

$$\vec{\nabla}\left(\frac{1}{M'}\sum_{j\in F_{i-k}}(Z_{i,j}-aZ_{ave,j+b}+c)^2\right)=0 \tag{3.3}$$

with $\vec{\nabla}$ the gradient $(\frac{\partial}{\partial a},\frac{\partial}{\partial b},\frac{\partial}{\partial c})$, F_{i-k} the set of samples that do not contain artifacts, and M' the number of samples in F_{i-k}.

Finally, the individual waves of Z_{temp} are combined into one template of the entire ECG complex and the template is subtracted from the recordings.

3.2 Fetal ECG optimization

After subtraction of the mECG, the recordings are still unsuited for direct fECG extraction. Besides residuals of the mECG, the recordings are also corrupted by other interferences and noise that easily exceed the low amplitude fECG. To enable detection of the QRS complexes, additional processing steps are required.

Several techniques have been proposed to exploit the spatial correlation between the electrode leads to enhance the SNR of the fECG [49, 95, 96]. Of these techniques, [95, 96] are purely mathematical techniques in which the fECG signals are combined in such a way that the resulting combinations exhibit either maximum variance (Principal Component Analysis, PCA) or maximum statistical independency (Independent Component Analysis, ICA). Important to remember is that in these techniques, no a priori knowledge on the physiology of the system is necessary and they are so called Blind-Source-Separation (BSS) techniques. Due to this lack of physiological basis, BSS techniques are less effective in separating the fECG from the noise in case of low SNR. Hence, it frequently occurs that the BSS techniques are not capable of extracting the fECG. As an alternative to the BSS techniques, Vullings et al. proposed a physiological-based source separation (PBSS) technique [49].

The PBSS has shown to perform equally as good or better compared to the BSS techniques and is used throughout this thesis. However, despite its relative good performance compared to the other techniques, the PBSS still resulted in numerous mis-detections. These mis-detections have a negative influence on the spectral analysis of the fetal heart rate and hence improvement of the PBSS technique is required. For the explanation of these improvements, a good understanding is required of the PBSS technique.

PBSS

The PBSS spatially combines the abdominal fECG, based on knowledge about the positions of the recordings electrodes. This information can be used to obtain the three-dimensional (3D) VCG (section 2.4). As schematically shown in Fig. 2.4, the typical time-path of the VCG during on cardiac contraction is of elliptic shape, with the highest amplitude pointing in the direction of the electrical heart axis. Since the ECG can be seen as the projection of the VCG onto a certain lead, projection along the direction of the electrical axis is expected to exhibit the largest amplitude of the QRS complex.

In the PBSS technique, the signals of the individual leads are combined into the VCG after which an ellipse fit is used to determine the direction of the electrical heart axis. Then, all information of the VCG is projected onto this axis to enhance the QRS complexes. An example of the processing steps in the PBSS is displayed in Fig. 3.2.

In the original PBSS technique, as described in [49], calculation of the VCG is done in 3D space. Instead, this thesis only uses a 2D representation of the VCG (in the coronal plane). Although the use of a 2D representation inevitably leads to a loss of some spatial information, it simplifies the calculation and makes the ellipse fit (hence the estimation of the electrical heart axis) less susceptible to artifacts.

For future reference, the VCG is represented by the $[2 \times T]$ matrix $\mathbf{S}$. The rows represent the VCG of length T in the Right-Lateral direction (RtLat, $\vec{x}$) and the Inferior-Superior direction (IS, $\vec{y}$). The N abdominal fECG recordings are represented by the $[N \times T]$ matrix $\mathbf{V}$ (Fig. 3.2a). Since $\mathbf{V}$ is measured, the goal is to determine $\mathbf{S}$ based on $\mathbf{V}$. The relation between $\mathbf{S}$ and $\mathbf{V}$ is given by:

$$\mathbf{V} = \mathbf{DS} \tag{3.4}$$

with transformation matrix $\mathbf{D}$ the $[N \times 2]$ matrix that contains all spatial information concerning the electrode configuration. The values of the $\mathbf{D}$ are estimated by means of a photograph of the electrode positions. Furthermore, the elements of $\mathbf{D}$ are normalized to make $\mathbf{D}$ invariant under transformation of coordinate system. Since $\mathbf{D}$ is not a square matrix, it cannot be inverted directly. The matrix is squared by multiplying both sides with the transpose of $\mathbf{D}$

$$\mathbf{D}^T\mathbf{V} = \mathbf{D}^T\mathbf{DS} \tag{3.5}$$

The matrix $\mathbf{S}$ can now be expressed in terms of $\mathbf{V}$

$$\begin{aligned}
(\mathbf{D}^T\mathbf{D})^{-1}\mathbf{D}^T\mathbf{V} &= (\mathbf{D}^T\mathbf{D})^{-1}\mathbf{D}^T\mathbf{DS} && (3.6)\\
(\mathbf{D}^T\mathbf{D})^{-1}\mathbf{D}^T\mathbf{V} &= \mathbf{IS} && (3.7)\\
\mathbf{D}^\dagger\mathbf{V} &= \mathbf{S} && (3.8)
\end{aligned}$$

where **I** is the unity matrix and $\mathbf{D}^{\dagger}$ represents the Moore-Penrose inverse of the matrix **D** [97]. An example of the 2D representation of the VCG is shown in Fig. 3.2b.

Since only 10% of the data contains information about the QRS complex (assuming a QRS complex of about 40ms [98] and a heart rate of 150 beats per minute), not all data should be included in the ellipse fittings. Therefore, the top 10% of the data points of the VCG are retained (Fig. 3.2c). Furthermore, to prevent potentially present artifacts from affecting the ellipse fit, the upper 1% is also omitted. The 10% and 1% boundary are determined based on the distance from the origin as the $\sqrt{S^2}$.

The ellipse fit used to find the electric heart axis is based on a least square fitting. Although this does not guarantee an optimal fit [99], other methods require an iterative approach and have significantly larger computation times. In the used approach, the ellipse is described by the conic equation in 2D:

$$f(\vec{x},\vec{a}) = a_1x^2 + a_2xy + a_3y^2 + a_4x + a_5y + a_6 = 0 \tag{3.9}$$

Only for points $\vec{x}_i$ that lie exactly on the ellipse, Eq. 3.9 will be zero. Any deviation will yield a measure for the error, ε, in the ellipse fit. Minimizing ε gives the optimal estimate of $\vec{a}$ (Fig. 3.2c).

$$\varepsilon = \frac{1}{T}\sum_{i=1}^{T}(a_1x^2 + a_2xy + a_3y^2 + a_4x + a_5y + a_6)^2 \tag{3.10}$$

In the final step of the algorithm, **S** is projected onto the long axis of the ellipse. The mixing matrix M_{PBSS}, that maps the abdominal fECG onto the long axis can be expressed as

$$\mathbf{M_{BPSS}} = \vec{r}_{long}\mathbf{D}^{\dagger} \tag{3.11}$$

with $r_{\vec{long}}$ the vector in the direction of the long ellipse axis. The vector $r_{\vec{long}}$ is determined as the furthest point on the ellipse measured from the ellipse center. From this, the S_{PBSS} is subsequently directly obtained from **V** by (Fig. 3.2d)

$$S_{PBSS} = \mathbf{M_{BPSS}}\mathbf{V} \tag{3.12}$$

Since S_{PBSS} exhibits an improved SNR compared to the fECG in the individual leads, S_{PBSS} can be used for further analysis of the fetal heart rate. For this purpose, the fetal R-peak locations are detected in S_{PBSS}. There are several algorithms available and these will be discussed in the next section.

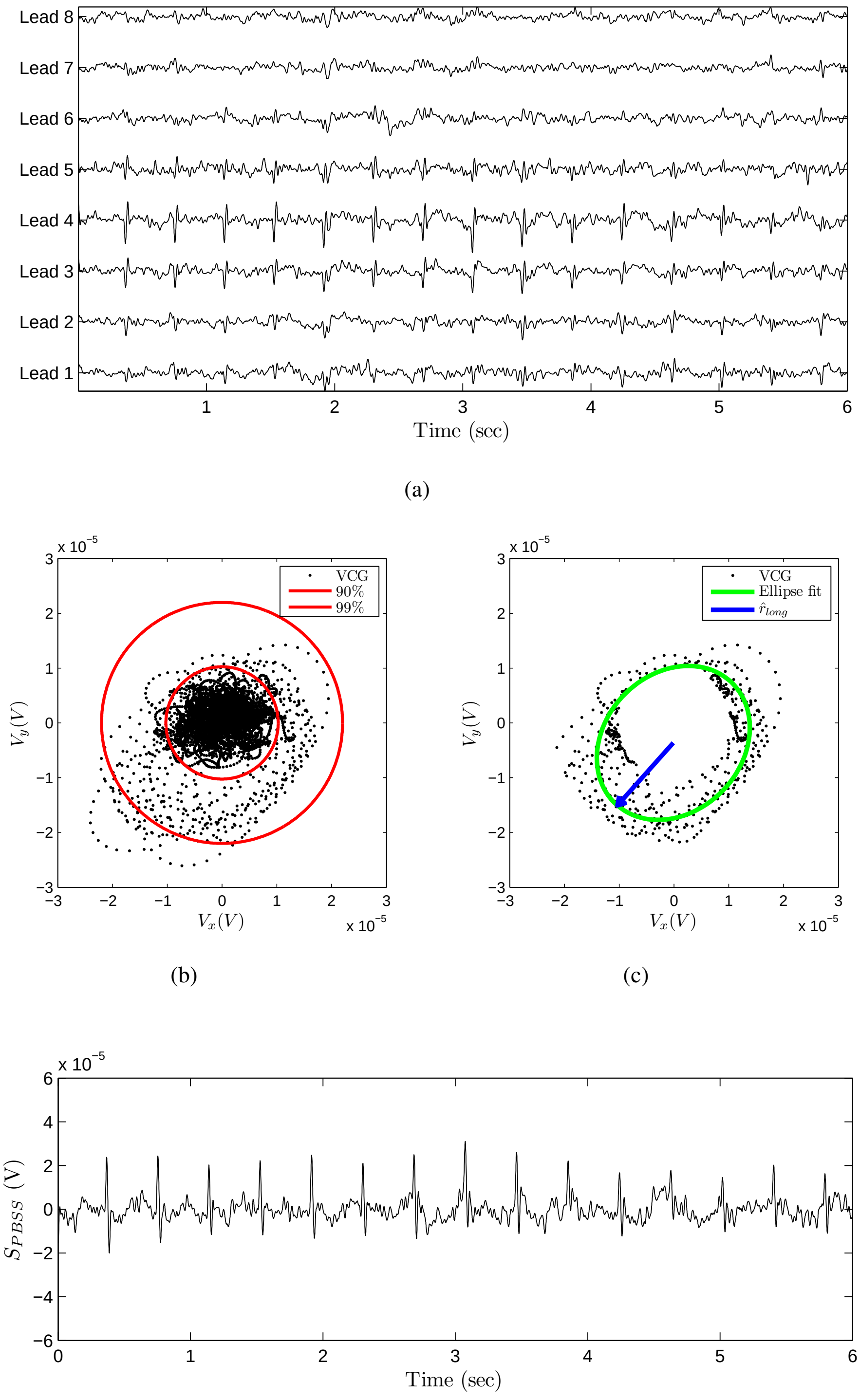

(a)

(b)

(c)

(d)

Figure 3.2 – *Processing steps of the PBSS technique are displayed. (a) The fECG in all individual leads. (b) The signals in the individual leads are combined into the 2D VCG with Eq. 3.8. The red circles indicate the 90% and 99% boundaries. (c) Before ellipse fitting, part of the data points are omitted. The electrical heart axis is determined as the long axis (blue) of the ellipse fit (green). (d) All data of the VCG are projected onto the elliptic long axis with Eq. 3.12.*

3.3 R-peak detection

The importance of correct R-peak detection for mECG subtraction becomes clear from the fact that the mECG complexes, used for the template estimation, are synchronized on their R-peak position. Incorrect detection, thus incorrect mECG subtraction, results in remaining artifacts in the fECG. Besides accurate peak detection in the mECG, the spectral analysis of the heart rate of the fECG also requires accurate peak detection [100]. An overview of different algorithms for peak detections is provided in [101], of which the most promising are summarized in [51].

Typically, peak detection algorithms consist of two parts. First, the QRS complexes are optimized based on linear and/or non-linear filtering. These filtering techniques usually use some a priori knowledge about the properties of the QRS complexes. The optimization is followed by a decision phase, in which the actual peaks are detected in the filtered signal using certain criteria, e.g. a threshold amplitude.

This section briefly discusses the peak detection algorithm proposed by Vullings et al. (used in WAMES and PBSS) [50] and the algorithm proposed by Rooijakkers et al. [51]. The latter is of interest, since it has shown to outperform other algorithms for both maternal and fetal QRS-peak detection.

3.3.1 Vullings

For the optimization phase, Vullings et al. uses a length-transformation that exploits knowledge about the amplitude, gradient, and length of the QRS complex. The interesting part of the algorithm is the decision phase, in which an optimal threshold amplitude is estimated, based on the statistical properties of the signal. The threshold value is derived analytically, using Bayesian probability theory. Due to this analytic approach, no information about the actual QRS peak position is required.

Signal optimization

Prior to the detection of the QRS complexes, the SNR of the ECG is enhanced using known properties of the QRS complexes. Firstly, the ECG is band-pass filtered exploiting knowledge about the frequency content of the QRS complex. The dominant frequency band for the maternal QRS complex is 10-25 Hz, while for the fetus this is 10-30 Hz [94]. Secondly, due to the physiological origin of the QRS complex, its amplitude and gradient are expected to be large compared to those of other parts of the ECG. Additionally, the length of the QRS complexes (90 ms in adults and 45 ms in fetuses [102]) distinguishes them from most artifacts that generally last much shorter.

In order to enhance the QRS complexes and to suppress the noise, a length transformation is used. In this transformation, the ECG ($V[i]$) is differentiated. Then, the absolute values of the gradient of the $V[i]$ are summed, by using an integrating window with the length that corresponds to the length of the QRS complex. This exploits the relatively large amplitude of the QRS complex. The resulting signal is commonly known as the sum of absolute differences (SAD) [103]:

$$S[n] = \sum_{i=1}^{M_{QRS}} |V[i+1] - V[i]| \tag{3.13}$$

with $S[n]$ the SAD at sample n and M_{QRS} the time window that corresponds to the length of a QRS complex.

Bayesian thresholding

QRS detection is usually based on an amplitude threshold value. The R-peak locations are identified by the part of the signals that exceed this threshold. The amplitude of the QRS-complexes can vary substantially and abruptly, hence the use of a dynamic threshold is favored over a fixed threshold.

The goal of the Bayesian approach is to design an adaptive threshold, of which the amplitude is updated according to the previous and new statistical information provided by the SAD. The instantaneous threshold ($\xi_{i,t}$), that is determined directly from the instantaneous statistical information provided by the SAD at each instant t, is defined by:

$$\xi_{i,t} = g \max\{|SAD_\tau|\} - (1-g) \min\{|SAD_\tau\} \tag{3.14}$$

with $|SAD_\tau| = |SAD[t-\tau]|, \ldots |SAD[t]|$, τ a time interval that contains at least one heart beat and g a constant that is experimentally determined. This instantaneous threshold, however, is based on the SAD that is most likely corrupted by noise. Furthermore, this non-optimal threshold does not use any prior information of previously determined thresholds. Therefore, in this Bayesian approach, an optimized threshold ($\xi_{o,t}$) is estimated using the statistical instantaneous and previous information of the signal.

The connection between the instantaneous threshold $\xi_{i,t}$ and the optimal threshold $\xi_{o,t}$ can be described by the following state-space model (Fig. 3.3)

$$\begin{cases} \xi_{o,t+1} & = \xi_{o,t} + \nu_t \\ \xi_{i,t+1} & = \xi_{o,t+1} + \eta_{t+1} \end{cases}$$

Here, ν_t represents the variation between the optimized threshold values $\xi_{o,t+1}$ and $\xi_{o,t}$, and η_{t+1} describes the contribution of artifacts to the instantaneous threshold $\xi_{i,t+1}$. In order to create an analytic solution and small computational complexity for the threshold, both ν_t and η_{t+1} are assumed Gaussian distributed with zero mean and variances $\sigma^2_{\nu,t}$ and $\sigma^2_{\eta,t+1}$ respectively.

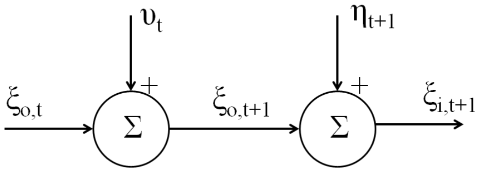

Figure 3.3 – *Illustration of the state-space model that describes the evolution of the optimized threshold for QRS detection.*

The goal is to estimate the new optimal threshold value $\xi_{o,t+1}$, given the available statistical information of the SAD ($\xi_{o,t}$, $\sigma^2_{\nu,t}$, $\sigma^2_{\eta,t+1}$, and $\xi_{i,t}$). The solution to these type of problems, can be found by Bayesian probability theory. The details of this derivation are found in Appendix A and this section only discusses the results. Due to the Gaussian behavior of ν_t and η_{t+1}, the estimation of the optimized threshold can be derived as

$$\hat{\xi}_{o,t+1} = \hat{\xi}_{o,t} + K_t(\xi_{i,t+1} - \hat{\xi}_{o,t}) \tag{3.15}$$

in which $\hat{\xi}_{o,t+1}$ represents the estimation for $\xi_{o,t+1}$. The variance of this estimation is given as

$$\sigma^2_{\hat{\xi}_{o,t+1}} = \sigma^2_{\hat{\xi}_{o,t}} + \sigma^2_{\nu,t} - K_t(\sigma^2_{\hat{\xi}_{o,t}} + \sigma^2_{\nu,t}) \tag{3.16}$$

The evolution of Eq. 3.15 and 3.16 is described by the Kalman gain K_t:

$$K_t = \frac{\sigma^2_{\hat{\xi}_{o,t}} + \sigma^2_{\nu,t}}{\sigma^2_{\hat{\xi}_{o,t}} + \sigma^2_{\nu,t} + \sigma^2_{\eta,t+1}} \tag{3.17}$$

Equations 3.15-3.17 allow to intuitively understand the behavior of the threshold $\xi_{o,t}$. If the signal is under influence of large artifacts, this results in a relatively large $\sigma^2_{\eta_t+1}$ compared to $\sigma^2_{\hat{\xi}_{o,t}}$ and $\sigma^2_{\nu,t}$. Therefore, the value of K_t will be low. As a consequence, the new estimated threshold value $\hat{\xi}_{o,t+1}$ in Eq. 3.16 is mainly determined by $\hat{\xi}_{o,t}$ and not by the instantaneous threshold $\xi_{i,t+1}$ (which is corrupted by the large artifact). On the other hand, if the noise level is low, $\sigma^2_{\eta_{t+1}}$ is low compared to $\sigma^2_{\hat{\xi}_{o,t}}$ and $\sigma^2_{\nu,t}$. Hence, the resulting K_t will be approximately one. In this case, the new estimate threshold $\hat{\xi}_{o,t+1}$ will solely be determined by the instantaneous threshold value $\xi_{i,t+1}$ (which is not influenced by noise).

3.3.2 Rooijakkers et al.

Alternative to the length transformation, Rooijakkers et al. uses a wavelet transformation to enhance the QRS complex. The wavelet transformation, in particular the continuous wavelet transformation (CWT), has already shown promising results [104]. The wavelet used by Rooijakkers et al. is specifically chosen to match the form of the QRS complex. After optimization by the wavelet transformation, the decision phase is based on information about the heart rate, the amplitude of previously found QRS complexes, and the local SNR.

Continuous Wavelet transformation

The fundament of the wavelet transformation lies in the use of wavelet functions. Throughout this thesis, only real wavelets will be used. A real function ψ can be classified as a wavelet if certain mathematical criteria are satisfied [105]:

1. A wavelet must have finite energy. Hence, the energy E

$$E = \int_{-\infty}^{\infty} |\psi|^2 dt \leq \infty \tag{3.18}$$

2. A wavelet has no zero frequency component. In other words, the mean of the wavelet $\psi(t)$ is zero.

Typically, a wavelet is defined as a mother wavelet ψ, with a family of *daughter* wavelets $\psi_{\tau,s}$. These daughter wavelets are obtained by scaling and translating the mother wavelet

$$\psi_{\tau,s} \equiv \frac{1}{\sqrt{s}}\psi^*(\frac{t-\tau}{s}) \tag{3.19}$$

The parameter τ is the *translational* parameter that gives the location of the wavelet in time, and the parameter s is the *dilation* parameter that scales the wavelet. The mother wavelet is contracted and dilated by changing the scale parameter s. The factor $\frac{1}{\sqrt{s}}$ is a normalization factor, that ensures the energy of the wavelet remains constant for all scales. An example of a wavelet is shown in Fig. 3.4.

A mother wavelet function has its own characteristic frequency content and peak frequency f_p. This peak frequency is defined as the frequency at which the Fourier transform of the mother wavelet $\Psi\omega$ is maximal. The relation between the peak frequency f_c (hence the frequency content) of a daughter wavelet at scale s is given by

$$f_c = \frac{f_p}{s} \tag{3.20}$$

Intuitively this can be understood from the fact that a large scale corresponds to a wide wavelet, thus a low frequency. On the other hand, a high scale wavelet corresponds to a narrow wavelet and high frequencies.

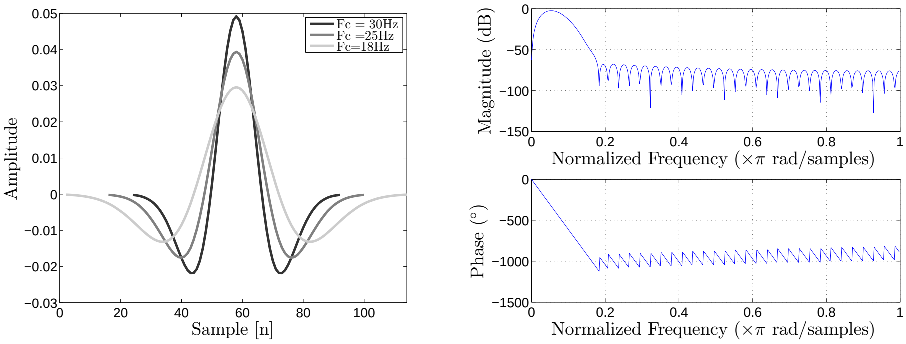

(a) (b)

Figure 3.4 – *(a) Plot of three Mexican Hat daughter wavelets. The associated peak frequencies are 18 (blue), 24 (red), and 30 (black). As can be seen from the figure, the central frequency determines the width and scale (and thus the frequency content) of the daughter wavelet. (b) The frequency response (upper graph) and phase shift (bottom graph) of the Maxican Hat with* $F_c = 30$.

The frequency content of each daughter wavelet is thus associated with a certain frequency band. The wavelet transformation uses this property, by comparing a certain daughter wavelet $\psi_{\tau,s}$ with a signal $x(t)$. The CWT of $x(t)$ is defined as [105–107]

$$W_{x;\psi}(\tau,s) = \frac{1}{\sqrt{s}} \int_{-\infty}^{\infty} x(t)\psi^{*}(\frac{t-\tau}{s})dt \tag{3.21}$$

with $W_{x;\psi}(\tau,s)$ the wavelet transformed signal and ψ^{*} the complex conjugate of the wavelet. Note that the used wavelets are real and the $*$ indication will be left out for further calculations. As a consequence of this convolution, the wavelet transformation defined in Eq. 3.21 can be seen as a band-pass filter.

In digital processing, the discrete-time continuous wavelet transform (DT-CWT) is used. Based on Eq. 3.21, the DT-CWT of a discrete signal $x[n]$ is given by

$$DTCWT_{x;\psi}[\tau,s] = \frac{1}{\sqrt{s}} \sum_{n=-\inf}^{\inf} x[n]\psi[\frac{n-\tau}{s}] \tag{3.22}$$

Similar to Eq. 3.21, $\psi[\frac{n-\tau}{s}]$ describes the mother wavelet, τ is the translational parameter, and s the dilation parameter.

Thinking of the wavelet transformation as a convolution of the mother wavelet with the ECG, the wavelet that mimics the waveform of the QRS complex is expected to perform optimal. Typically, the QRS complex exhibits a waveform similar to a Mexican Hat (Fig. 3.4). The use of a Mexican Hat wavelet as an optimal filter was confirmed by Rooijakkers et al. [51]. The Mexican Hat wavelet is described by the function

$$\psi[n] = (1-n^2)e^{-\frac{1}{2}n^2} \tag{3.23}$$

The scaling parameter fully determines the frequency content of the Mexican Hat wavelet and thus its filter properties. The choice of the daughter wavelet, defined by s, depends on the frequency content of the maternal and fetal QRS complexes. The optimized signal is then obtained by convolution of the created wavelet with the (maternal or fetal) ECG.

Peak detection

The detection algorithm proposed by Vullings et al. does not require any information about the actual peak locations. In contrast, Rooijakkers et al. take the peak location, peak amplitude and local SNR into account for the calculation of a threshold. The R-peaks are detected in an iterative manner that consist of four consecutive stages: 1) segment selection, 2) threshold determination 3) peak detection 4) SNR estimation.

The segment selection in each iteration is chosen such that it is expected to contain exactly one R-peak. The limits of the next segment (δS) are related to the previously found R-peak positions and a prior assumptions on the physiologically possible heart rate (for adults 32-210 beats per minute (BPM), for fetuses 50-255 BPM). The start of the segment (δS_s) is defined by the previous peak $p[n-1]$ and the minimum RR-interval (interval between two QRS complexes, calculated as $\frac{60}{BPM}$)

$$\delta S_s[n] = p[n-1] + RR_{min} \tag{3.24}$$

The end of the segment (δS_e) is chosen variable, based on the previous RR-interval (RR_{prev}) and is updated when no peak is found. The segment end is upper limited by the maximum RR-interval (RR_{max})

$$\delta S_e[n] = \delta S_s + \min\{\beta RR_{prev}, RR_{max}\} \tag{3.25}$$

where the factor β is empirically determined to 1.7, in order to reduce to number of false positive detections.

A threshold value (T) is determined for each segment δS, based on the previous threshold value (T_{prev}) and a new estimate threshold ($\hat{T}$). This threshold is defined as [51]

$$T = \alpha\hat{T} + (1-\alpha)T_{prev} \tag{3.26}$$

with α describing the contribution of $\hat{T}$ and T_{prev} to the new threshold. The estimation threshold $\hat{T}$ is based on the local noise level

$$\hat{T} = N_l S_{max} \tag{3.27}$$

in which N_l is the estimated local noise level and S_{max} the maximum value in the current preprocessed signal segment.

The definition of SNR in a classical sense is determined by

$$SNR = 10\log_{10}(\frac{P_s}{P_n}) \tag{3.28}$$

with P_s the signal power and P_n the noise power. In Rooijakkers et al., P_s is defined as the maximum power within fixed windows around a detected R-peak, and P_n as the maximum power in the segments between consecutive R-peaks. Since these powers are not measured in the same region, Eq. 3.28 does not measure the actual SNR. However, Eq. 3.28 does provide for a measure of the signal quality in the surrounding of a QRS complex and, hence, will be further denoted as Surrounding-Signal-Quality (SSQ). The parameter N_l in Eq. 3.27, is defined as [51]

$$N_l = \frac{6 - SSQ}{8} \tag{3.29}$$

A peak is identified as the part of the wavelet transformed ECG that exceeds the threshold. If no peak is found, the segment end δS_e is extended and the threshold value T is lowered for up to two more iterations. The segment end is updated by

$$\delta S_e = \begin{cases} \delta S_s + \frac{\beta RR_{prev} + RR_{max}}{2} & ;2^{\text{nd}} \text{ iteration} \\ \delta S_s + RR_{max} & ;3^{\text{nd}} \text{ iteration} \end{cases}$$

and the threshold value by

$$T = \alpha\hat{T} + (1-\alpha)\frac{T_{prev}}{2} \tag{3.30}$$

If after three iterations still no peak is found, a new search is started in a segment δS, which is moved forward by $1s$.

3.4 Spectral analysis of fetal heart rate variability

In order to analyse the fetal HRV, the spectral content of extracted fetal heart rate signal is evaluated. Traditionally, studies used the Fourier-Transformation (FT) for this purpose [28, 29, 108, 109].However, for reasons that will be explained in section 3.4.3, the use of FT does not seem satisfactory for the analysis of the HRV.

Recently, a new technique is developed based on the Continuous Wavelet Transformation (CWT) [100], which is already briefly introduced in section 3.3.2 for R-peak detection. The CWT allows for multi-resolution time frequency analysis and has been successfully applied for the analysis of the heart rate variability [110–112].

In [100], a comparison was made between the STFT and CWT for artifact corrected heart rate signals. The results indicated that, to obtain reliable spectral information, the STFT allowed only 5% percent artifact correction and the CWT up to 20% artifact correction. Although this result advocates the use of CWT over STFT, the study of [100] assumes that locations of artifacts within the heart rate signals are known. Besides known artifacts, the heart rate signals are also contaminated by unknown mis-detections. Furthermore, [100] does not discuss the influence of prolonged interpolation in the heart rate signal. In this thesis, a study is performed to examine the influence of undetected artifacts and consecutive interpolation on the performance of the STFT and the CWT (section 4.4). For this reason, both analysis techniques are discussed here.

3.4.1 Preprocessing of the heart rate signals

The signal that needs to be analyzed consists of the R-R intervals, the distance between two consecutive R-peaks. These heart rate values can only be determined at times at which a heartbeat occurs. Due to this, measured heart rate values are not equidistantly distributed in time. In order to perform any spectral analysis, the set of determined heart rate values has to be transformed into an equidistant set of data points. The resampling technique employed in this work is based on the method already used in [28, 29, 100, 108, 109, 113]. In this method, interpolation is used to create heart rate values equidistantly distributed in time. This technique simply keeps a certain RR value until it encounters a new value and then holds this value. To obtain a continuous function, the interpolated RR values are convoluted with a square function.

3.4.2 Fourier Transformation

The Fourier Transformation is the most commonly known method to analyze a time signal for its frequency content. In the FT, the time signal is decomposed into trigonometric basis functions. The transformed signal $X_{FT}(f)$ gives the frequency distribution of the time signal $x(t)$ as follows

$$X_{FT}(f) = \int_{-\infty}^{\infty} x(t) \exp -i2\pi f t dt \tag{3.31}$$

In case of discrete time signals (as is the case in our signal processing) the discrete FT becomes

$$X_{DFT}[f] = \frac{1}{N} \sum_{k=0}^{N-1} x[k] \exp -i2\pi k \Delta T \tag{3.32}$$

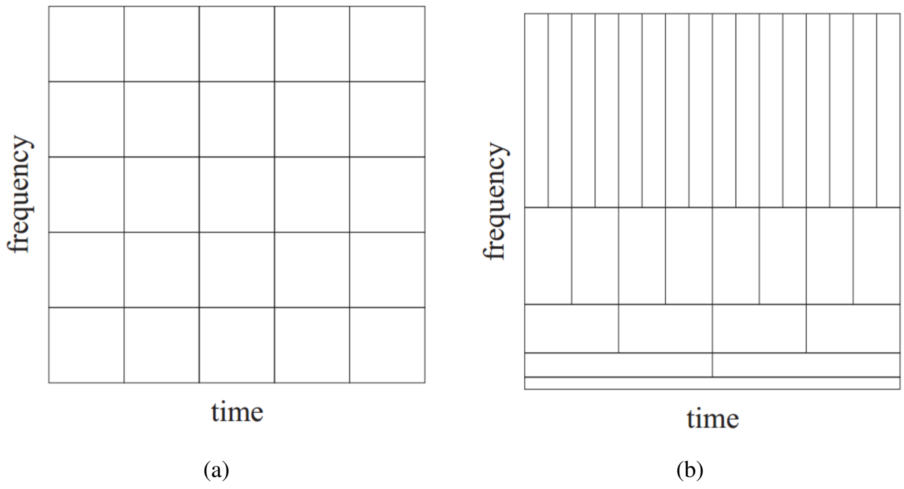

(a) (b)

Figure 3.5 – *(a) Constant resolution in the Time-frequency plain of the STFT. (b) Multi-resolution time frequency plane of the wavelet transformation.*

in which N is the number of samples of the time signal and ΔT the time of each sample.

Since the FT retrieves the global frequency content, it is only useful for stationary and pseudo-stationary signals. In order to obtain more local information, the Short Time Fourier Transformation (STFT) can be used. The STFT is able to retrieve both frequency and time information from a signal. The STFT calculates the FT of a windowed part of the original signal, where the window $g(t)$ shifts along the time axis. A FT is taken of the windowed signal which gives the frequency content in the windowed time interval. In order to prevent spectral leakage in the windowed time interval, a window-function is used. The STFT is denoted as

$$X_{STFT}(\tau, f) = \int_{-\infty}^{\infty} x(t) g^{*}(t-\tau) \exp -i2\pi f t dt \tag{3.33}$$

with $(*)$ indicating the complex conjugate of g and τ the center of the window.

The resolution in time and frequency is determined by the Heisenberg inequality [114], which states that

$$\Delta t \times \Delta f \geq \frac{1}{4\pi} \tag{3.34}$$

A time-frequency plot will hence be divided into block of equal size $\Delta t \times \Delta f$, as shown in Fig. 3.5a. The total frequency power is obtained by integration over time and frequency.

3.4.3 Wavelet Transformation

The constant resolution shown in Fig. 3.5(a) does not seem satisfactory for the current study. Low frequency components usually last a long period of time, so a low time resolution can be obtained. High frequency components on the other hand often appear as short bursts, invoking the need for a higher time resolution. Besides, the artifacts in the heart rate signals mainly affect the higher frequencies. Therefore, a higher time resolution in the high frequencies would limit the duration of the influence of artifacts. Hence, the need for multi-resolution analysis.

A technique that allows for multi-resolution analysis is the wavelet transformation. The wavelet analysis calculates the correlation between the signal and a wavelet function $\psi(t)$. The similarity between the signal and the analyzing wavelet function is computed separately for different time intervals, resulting in a two dimensional representation called a *scalogram*. An example of a scalogram is shown in Fig. 3.5b.

The properties of a wavelet function have already been discussed in section 3.3.2. The CWT of a function $x(t)$ is given by

$$W_{x;\psi}(\tau,s)=\frac{1}{\sqrt{s}}\int_{-\infty}^{\infty}x(t)\psi^{*}(\frac{t-\tau}{s})dt \tag{3.35}$$

Each of the daughter wavelets $\psi^{*}(\frac{t-\tau}{s})$ is a scaled and time shifted version of the mother wavelet. The relation between the peak frequency of the mother wavelet (f_p) and the peak frequency of a scaled daughter wavelet (f_c) is given by

$$f_c=\frac{f_p}{s} \tag{3.36}$$

Besides that scaling changes the central frequency of the wavelet, it also affects the length of the wavelet and thus the length of its analyzing window. Since the Heisenberg inequality of Eq. 3.34 still has to hold, the time resolution (determined by the length of the wavelet) limits the width of the frequency band. A long wavelet (low time resolution) imposes a high resolution in the frequency band, whereas a short wavelet (high time resolution) imposes a low frequency resolution.

In case discrete values are used for τ and s, each daughter wavelet can thus be associated with a Heisenberg box. The width in time and frequency are determined by the scaling parameter. All boxes have equal surfaces due to the Heisenberg inequality.

Due to the scalable time and frequency resolution of the CWT, it qualifies for analysis of non-stationary signals and therefore has been successfully applied for the analysis of the heart rate variability [110–112]. In analogy with the FT, the scalogram allows to determine the power content in each Heisenberg box and the frequency power is calculated by integration over time and frequency.

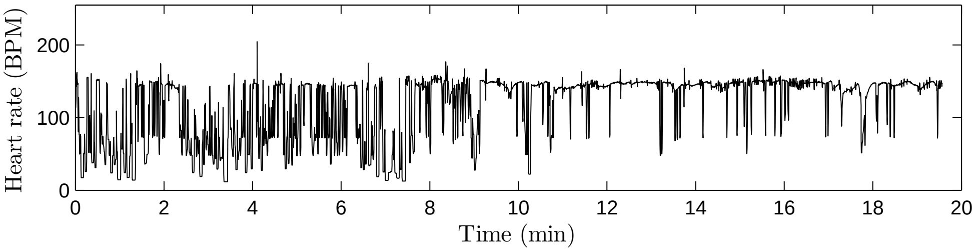

Figure 3.6 – *An example of the extracted fetal heart rate of a 20 minute measurement after processing with PBSS in combination with the peak detection algorithm of Rooijakkers et al. Only around 12 minutes some potentially reliable heart rate is seen.*

3.5 Limitation of existing algorithms

The WAMES [48] and PBSS [49] technique have shown to outperform other techniques for the subtraction of the mECG and Source-Separation of the fECG in multi-lead abdominal recordings. The main improvement compared to other techniques is that both WAMES and PBSS are designed to exploit physiological knowledge of the mECG and the fECG. Besides WAMES and PBSS, the peak detection algorithm of Vullings et al. [50] and Rooijakkers et al. [51] have shown promising results regarding the maternal and fetal R-peak detection.

Although PBSS and the peak detection algorithms have improved extraction of the fetal heart rate considerably, the combined use of these state-of-the-art techniques still frequently results in unreliable fetal heart rates. An example of such an unreliable extracted fetal heart rate from a 20 minute abdominal recoding after processing by WAMES, PBSS and Rooijakkers et al. is shown in Fig. 3.6. This section discusses the main limitations of the PBSS and the peak detection algorithms that cause to the unreliable extraction of the fetal heart rate.

PBSS In order to extract the fECG from abdominal recordings, using PBSS, correct estimation of the electrical heart axis is crucial since this is directly related to the quality of the QRS complexes in the projected signal (S_{PBSS}, Eq. 3.12). The ellipse fit, and thus the estimation of the electrical heart axis, does assume some level of the quality of the fECG. Firstly, PBSS operates under the assumption that, by combining the lead signals V into the VCG, the noise is inhibited and the QRS complexes are enhanced such that the amplitude of the QRS complexes exceeds the amplitude of the noise in the VCG. Hence, the noise is assumed to only appear in the lower 90% of the VCG. Secondly, artifacts of amplitude larger than the QRS complexes are assumed to occur less than 1% of time. If either one of these assumptions is false, e.g. due to a relatively large noise amplitude in the VCG or the presence of numerous artifacts, the estimation of the electrical heart axis will deviate from the actual electrical heart axis and the SNR of the QRS complexes in S_{PBSS} is lowered. Fig. 3.7 displays the

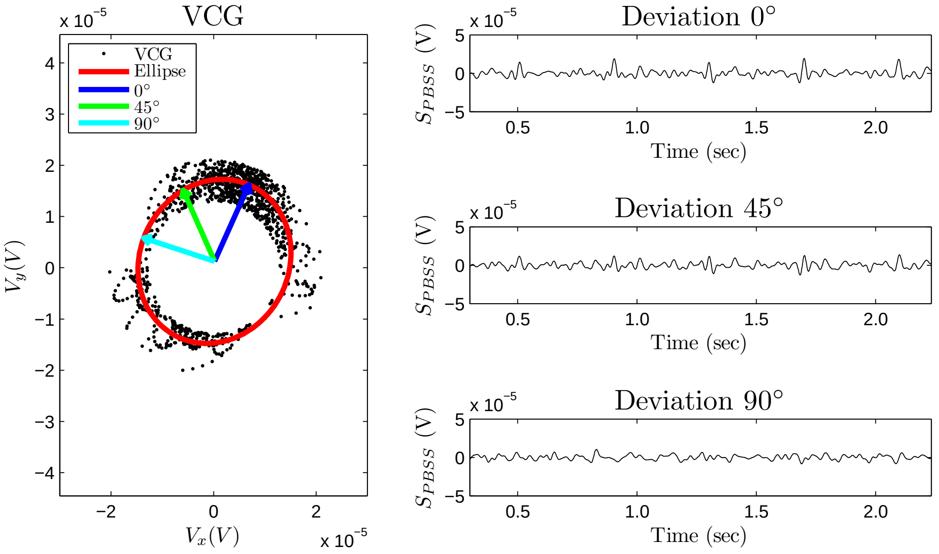

Figure 3.7 – *The effect of incorrect estimation of the electrical heart axis on the presentation of the QRS complexes in S_{PBSS}. The left graph display the VCG with the correct projection axis, and the projection axis rotated by* 45° *and* 90°. *The graphs on the right show S_{PBSS} corresponding to the different orientations of the projection axes.*

effect of incorrect estimation of the electrical heart axis on S_{PBSS} by projecting V_2 on projection axes with different orientations.

Peak detection The peak detection algorithms of Vullings et al. and Rooijakkers et al. are both based on amplitude thresholding, and the part of the optimized signal (S_{opt}, either the SAD in Eq. 3.13 or the wavelet-transformed in Eq. 3.21 mECG or fECG) that exceeds the threshold amplitude is identified as a R-peak. For the mECG, the R-peak practically always exceeds the noise amplitude. Besides, large and rapid fluctuations can be seen in the maternal heart rate, since the adult ANS is fully developed. For these reasons, R-peak detection based on an amplitude threshold in combination with allowance of a wide spread in consecutive heart rate values seems the appropriate choice.

In contrast to the mECG, the R-peak amplitude of the fECG is of the same order of magnitude as the noise amplitude. Therefore, it is more likely that noise overshadows the fetal R-peak. An example of the effect of noise on the mECG and the fECG is displayed in Fig. 3.8. Current R-peak detection algorithms operate under the assumption that it is always possible to detect the fetal R-peak. In practice, however, the fetal R-peak amplitude is not always large enough to be detected. The appearance of noise that exceeds the R-peak and the presence of artifacts, often leads to a large number of mis-detections of R-peaks and thus disturbances in the heart rate signal.

An important limitation of current R-peak detection algorithms is the absence of an analysis of the legitimacy of the detected R-peaks and their corresponding QRS complexes. Although usually some sanity check is performed on the location of a newly found R-peaks, this is only based on previously found R-peaks and a wide expectation region is allowed for a new R-peaks to occur (as for the maternal R-peak detection). As a consequence, numerous noise peaks with an amplitude larger than the fECG are incorrectly identified as an R-peak.

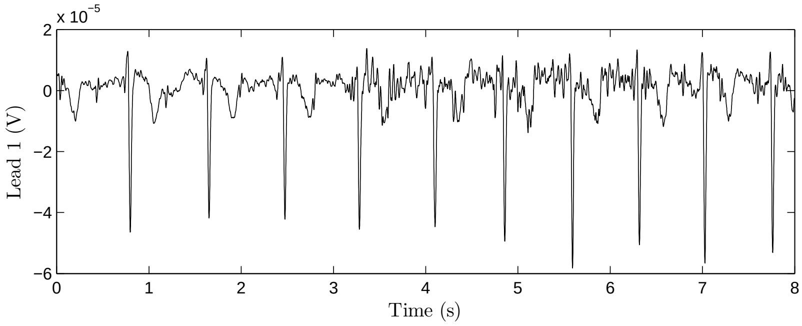

(a) Maternal ECG

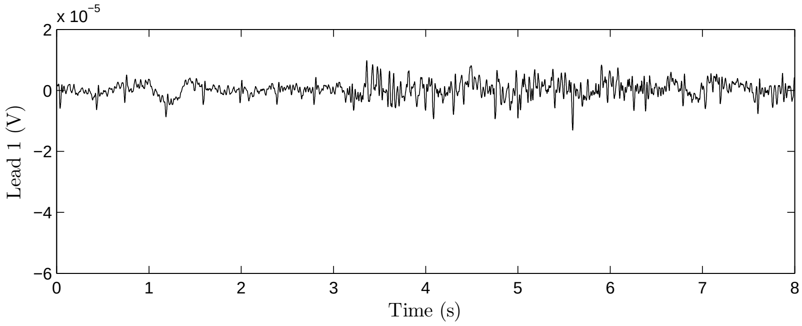

(b) Fetal ECG

Figure 3.8 – *The effect of noise interference on the mECG and the fECG. Whereas the noise is insignificant for mECG detection (a), it severely disturbs the fECG (b).*

3.6 Summary

Despite numerous improvements of newly developed processing techniques that regard the extraction of fECG from abdominal recordings, at present, these techniques are unsuited for automated fECG extraction due to the limitations that are discussed in section 3.5. In this thesis, an attempt is made to overcome these limitations by improved implementation of the existing techniques. Furthermore, a new algorithm is developed that ensures reliable extraction of the fECG by a combination of the improved existing techniques and newly additionally developed techniques.

Chapter 4

Materials and methods

In the previous chapter, state-of-the-art techniques in the field of fECG extraction have been discussed. Despite the numerous improvements of these techniques, they still do not allow for reliable automated fECG extraction. This chapter discusses the work done in this thesis regarding the development of a new algorithm that is meant to overcome the limitations of the current techniques and that enables reliable automated fECG extraction. The outline of this chapter is illustrated by the flow chart in Fig. 4.1. Firstly, the acquisition of the data used to optimize and evaluate the algorithms developed in this thesis is explained. Secondly, improvements to existing techniques and the newly developed algorithms that are used for extraction of the fECG from the acquired data is explained. This chapter also includes a description of the methodology for the implementation and evaluation of the developed algorithms. Finally, criteria for fetal heart rate signals are determined that ensure reliable spectral parameters for STFT and CWT. The clinical study of the spectral parameters of the fetal HRV is not discussed in this chapter but is discussed separately in chapter 7. The end of this chapter also contains an intermezzo that discusses a feature of the developed algorithm, regarding the detection of arrhythmias of the heart rate.

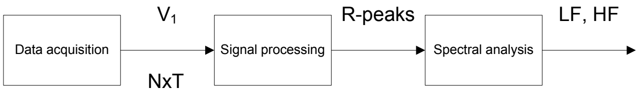

Figure 4.1 – *Schematic illustration of the outline of this chapter. First, the acquisition of the data used throughout this thesis is explained. The output* V_1 *are the* N *lead abdominal recordings of length* T*. After the data acquisition, the newly developed algorithm for fECG extraction is explained in the signal processing. The found fetal R-peak locations by the fECG extraction algorithm are used for spectral analysis. In the final section of this chapter, the criteria that enable reliable spectral analysis of STFT and CWT are determined.*

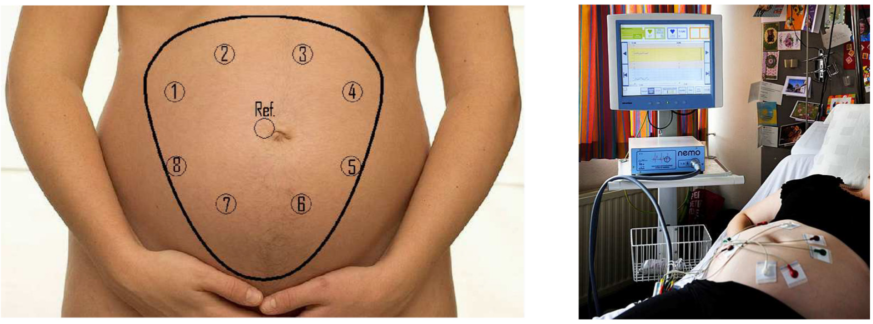

(a) (b)

Figure 4.2 – *(a) Schematic illustration of the electrode configuration on the maternal abdomen used for the IHDB. (b) The NEMO system used to perform the abdominal measurements*

4.1 Data acquisition

Throughout this thesis, an in-house database (IHDB) is used to evaluate the performance of the developed algorithms. The IHDB consists of abdominal recordings in a longitudinal study conducted throughout the pregnancy. The study was approved by the Medical Ethics Committee of the MMC and patients were included in the study after informed consent. Inclusion criteria for the patients were healthy women above 18 years of age with an uncomplicated singleton pregnancy of at least 14 weeks of gestation. In total 41 patients were included in the study.

Measurements were conducted around 14, 18, 22, 24, 26, 30, 34, 36, 38, 40, 41 and 42 weeks of gestation. However, for some women, not all measurements were performed due to various reasons. The recording time for each measurement varied from about 45 minutes to 60 minutes. In total, 304 measurements were performed with a total measurement time of approximately 236 hours. Due to memory issues concerning the mECG subtraction each measurement is divided into recordings of 15 minutes, resulting in 1076 files for analysis.

The recordings of the IHDB consist of 8 bipolar signals with the electrodes in a circular configuration and the reference electrode in the center, as displayed in Fig. 4.2a. The electrode configuration is chosen such that the entire uterine area can be monitored. The configuration ensures that, independent of the fetal position within the uterus, at least some electrodes are close to the fetal heart and thus record the fECG with sufficient amplitude. The abdominal signals are recorded at a sample frequency of 1 kHz by the NEMO system, shown in Fig. 4.2b.

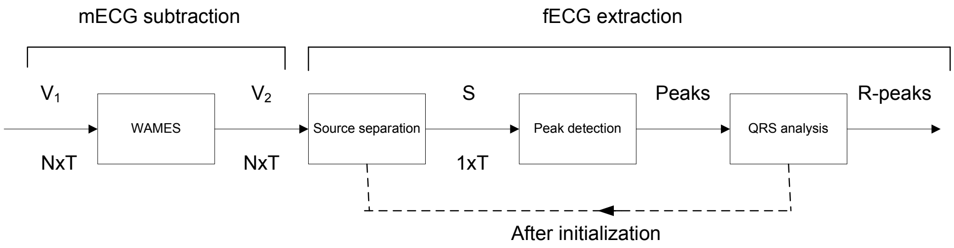

Figure 4.3 – *Flow chart of the algorithm used to extract the fECG from abdominal recordings. The mECG is subtracted with WAMES, prior to processing steps used for fECG extraction.*

4.2 Signal processing: Fetal ECG extraction

The algorithm developed to extract the fECG consists of a combination of existing processing techniques and additional processing techniques developed in this thesis. The used existing techniques (WAMES, PBSS, and the peak detection algorithms of Vullings et al. and Rooijakkers et al.) are chosen based on their performance and have been explained in the technical background. The new additional processing algorithms are developed to overcome the limitations of these existing techniques. A flowchart of the entire algorithm is displayed in Fig. 4.3. Each block of the flowchart is discussed in a separate section, with headers that correspond to the name of the blocks.

First, WAMES (section 3.1) is used to subtract the mECG from the abdominal recordings (V_1). The remaining abdominal signals after the mECG subtraction (V_2) are then spatially combined by Source-Separation-techniques into S (Eq. 3.8) to enhance the SNR of the fECG. For this purpose, the PBSS technique of section 3.2 is used in combination with a newly developed improved extension of the PBSS technique. Peak detection is performed on S by either the algorithm of Vullings et al. or Rooijakkers et al., depending on their performance (discussed in section 4.3). Finally, an analysis algorithm is developed that evaluates the found R-peaks based on their corresponding QRS complexes.

4.2.1 Source separation

After WAMES is used to subtract the mECG from V_1, PBSS is used to combine the leads recordings of V_2 in order to enhance the fECG. The strength of PBSS lies in the fact that V_2 is combined based on physiological principles and that, therefore, PBSS is more effective in case of low SNR compared with Blind-Source-Separation techniques [49].

In order to extract the fECG from the measurements, using PBSS, correct estimation of the electrical heart axis is crucial since this is directly related to the quality of the QRS complexes in the projected signal (S_{PBSS}, Eq. 3.12). To account for changes in the orientation of the electrical heart axis due to fetal movement, the implementation of the algorithm described by the flow-chart is done in an iterative manner. In this iterative process, a buffer segment $V_{2,buf}$ is defined with a length of 30 seconds and in each iteration two seconds of new data is evaluated. Note that the length of the buffer and the update rate are chosen such as to match the buffer length and the update rate used in WAMES, and only the final 15 seconds of $V_{2,buff}$ is used to compute the VCG.

The main limitation of PBSS regards incorrect estimation of the electrical heart axis as a result of a relatively large noise amplitude or artifact disturbances in the VCG, as is described in section 3.5. To overcome this limitation, improvements are developed as an extension to the PBSS. The improved PBSS is further denoted as PBSSi.

PBSSi

Since PBSS does not require any prior information about the location of fetal QRS complexes, this technique is used for estimation of the electric heart axis in case no QRS complexes have been identified. However, once sufficient QRS complexes have been identified, these QRS complexes can be used to improve the estimation of the electrical heart axis, in particular if the noise amplitude exceeds the QRS amplitude in the VCG or numerous artifacts disturb the VCG.

In PBSSi, previously found QRS complexes are used to produce the VCG and to generate the projection signal S_{PBSSi}. The width of a QRS-complex is assumed 50ms [**?**], and the QRS complex (Z_i) is defined based on its R-peak location (P_i) as

$$Z_i = \{P_i - 25\text{ms}, ..., P_i + 25\text{ms}\} \tag{4.1}$$

Due to the dependency of PBSSi on QRS complexes, PBSSi is only activated after sufficient QRS complexes have been identified by an initialization phase (explained in section 4.2.3). Furthermore, if no QRS complex is identified for a prolonged period of time, the information of previously found QRS complexes about the orientation of the electrical heart axis might be outdated due to fetal movement. Therefore, if any of the QRS complexes used for the estimation of the electrical heart heart axis is located prior to the start of $V_{2,buf}$, the traditional PBSS is again used as Source-Separation technique. The potential feedback from previously found QRS complexes to the Source-Separation is indicated as a dotted line in the flow chart of Fig. 4.3.

As a second improvement of the original PBSS technique, the movement of the projection axis in each iteration ($\hat{\vec{r}}[n+1]$) is damped with respect to the orientation of the projection axis in the previous iteration ($\hat{\vec{r}}[n]$). In order to provide a more robust estimation of the electrical heart axis, damping is implemented by means of a learning rate C_{LR}. The learning-rate imposes a damping on the step-size of the orientation of the new projection axis. The orientation of the new projection axis is given by

$$\hat{\vec{r}}[n+1] = \mathbf{R}(C_{LR} \cdot \theta)\hat{\vec{r}}[n] \tag{4.2}$$

with $\mathbf{R}(x)$ the (2D) rotation-matrix of x radians. In Eq. 4.2, θ describes the angle between $\hat{\vec{r}}[n]$ and the newly found projection axis $\vec{r}[n+1]$. An example of the effect of C_{LR} is shown in Fig. 4.4a. The introduction of C_{LR} ensures that the projection axis only fully rotates towards the new orientation if this orientation lasts for several iterations. The value of C_{LR} is a trade-off between sensitivity to fetal movement and robustness against artifacts, and is chosen $\frac{1}{3}$.

Finally, it can occur that the amplitude of the R-peak in the VCG is equal to the amplitude of the S- or Q-peak in the VCG. This might cause the orientation of $\vec{r}[n+1]$ to be in opposite direction with respect to that of $\hat{\vec{r}}[n]$ ($\theta \geq 90°$, Fig. 4.4). As a result, if the VCG were to be projected onto $\vec{r}[n+1]$, the sign of the new S_{PBSS} would be inverted with respect to the S_{PBSS} of the previous iteration. Although this does not influence the peak detection, an estimation of the average QRS waveform (used in the QRS analysis in section 4.2.3) is no longer possible because this average QRS complex will tend to zero. Therefore, if θ exceeds 90°, $\vec{r}[n+1]$ is inverted, after which $\hat{\vec{r}}[n+1]$ is calculated with Eq. 4.2.

An example of the VCG and a corresponding S_{PBSS} and S_{PBSSi} is shown in Fig. 4.5.

4.2.2 Peak detection

In the original implementation of WAMES and PBSS, the peak detection algorithm of Vullings et al. is used for both maternal and fetal R-peak detection. In a recent study of Rooijakkers et al., however, an algorithm is developed that has shown to outperform the peak detection algorithm of Vullings et al. for both maternal and fetal R-peak detection [51]. Despite these promising results of Rooijakkers et al., it came to the authors attention the implementation of the peak detection algorithm of Vullings et al. in previous studies [48,49,51] deviates from its theoretical description and does not perform optimal.

As explained in section 3.3.1, the estimated optimal threshold value is determined by means of Eq. 3.15, 3.16 and 3.17. In previous studies, however, the variance $\sigma^2_{\nu,t}$ is not taken into account. Due to this different implementation, the estimated threshold $\hat{\xi}_{o,t}$ is unable to rapidly decrease back to normal values after an artifact with an amplitude higher than the R-peak amplitude has occurred. This is effect is shown in Fig. 4.6. The exact reason why the optimized threshold is unable to rapidly

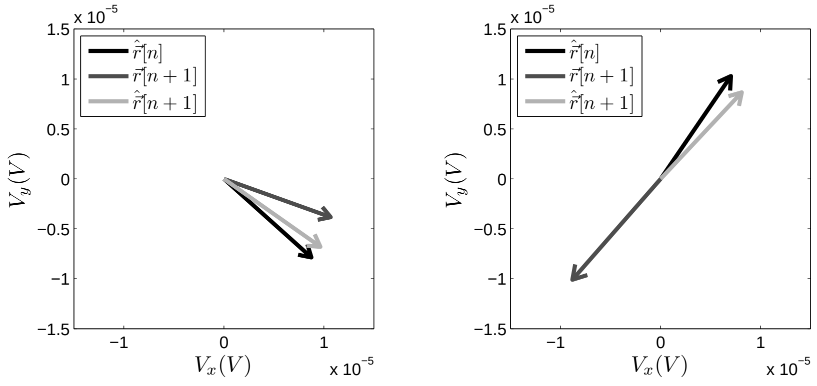

(a) C_{LR} (b) Inverse axis

Figure 4.4 – *Both graphs display the orientation of the projection axis for consecutive iterations. (a) The effect of damped movement of the projection axis by the learning rate* C_{LR}*. (b) If the angle between* $\hat{\vec{r}}[n]$ *and* $\vec{r}[n+1]$ *is over 90°, the orientation of* $\vec{r}[n+1]$ *is inverted.*

decreased back to normal values with this previous implementation is explained in Appendix A.3.

To allow for a rapid adaptation of the optimized threshold after a large artifact, the variance $\sigma^2_{\nu,t}$ is included in the implementation. Since in Eq. 3.3.1 the parameter ν represents the change in consecutive optimized thresholds $\xi_{o,t}$ (i.e. the first derivative of $\xi_{o,t}$), the variance of ν is estimated as the second derivative of $\xi_{o,t}$. After implementation, the optimized threshold value is able to adjust rapidly after an artifact, as shown in Fig 4.6.

Due to the improved implementation of the peak detection algorithm of Vullings et al., the performance of the peak detection algorithms of Vullings et al. and Rooijakkers et al. has to be reevaluated for maternal and fetal R-peak detection, as will be discussed in section 4.3. The best performing detection algorithm for maternal and fetal R-peak detection is used for mECG subtraction and fECG extraction, respectively.

4.2.3 QRS analysis

Despite the improved implementation of the peak detection algorithm of Vullings et al., both Vullings et al. and Rooijakkers et al. are limited regarding the reliability of detected peaks, in particular for the fetal R-peak detection. This limitation is explained in detail in section 3.5 and mainly arises from the fact that these peak

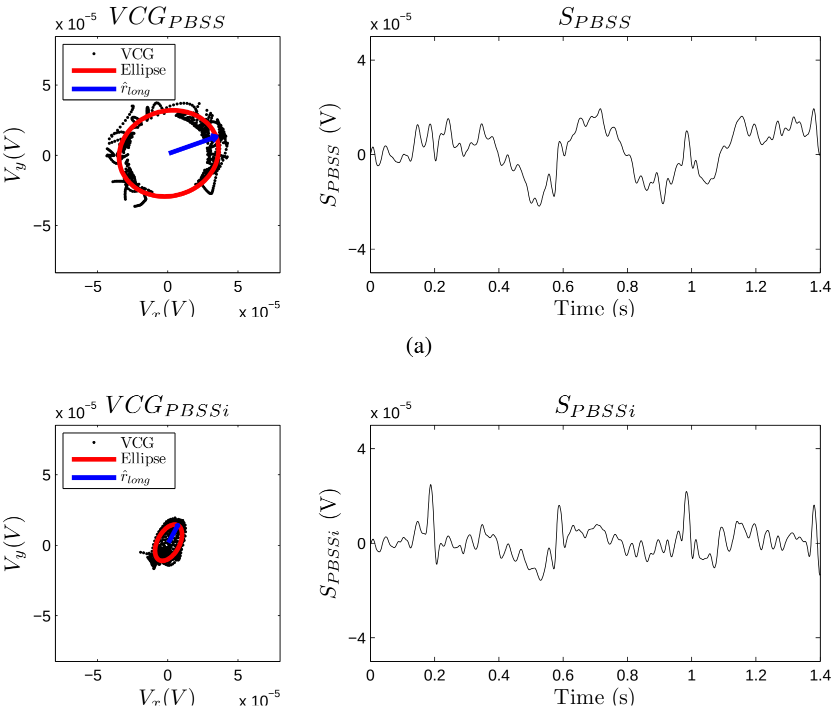

(a)

(b)

Figure 4.5 – *Comparison between PBSS (a) and PBSSi (b) for the estimation of the electrical heart axis. The left graphs show the VCG and the estimated electrical heart axis with PBSS and PBSSi. The corresponding S_{PBSS} and S_{PBSSi} are displayed on the right. The difference in amplitude of the VCG of PBSS compared to PBSSi is caused by an artifact (not displayed) that disturbs the VCG in PBSS. The presence of the artifact does not disturb the VCG of the PBSSi. The combined effect of using only QRS complexes for the estimation of the electrical heart axis and the damping of the movement of the electrical heart axis, results in improved quality of the QRS complexes in S_{PBSSi} with respect to the QRS complexes in S_{PBSS}. The angle between the estimated projection axis of PBSS and PBSSi is* 43°.

detection algorithms operate under the questionable assumption that it possible to detect the fetal R-peak at all times.

To overcome this limitation, an automated QRS analysis algorithm is developed. This algorithm analyses a newly found QRS complex Z_{i+1} based on the quality of the optimized signal (S_{opt}) in the surroundings of Z_{i+1} (SSQ, determined with Eq. 3.28), and compares the R-R interval and the QRS waveform of Z_{i+1} to a running average of the R-R interval and the QRS waveform (Z_{ave}).

In the QRS analysis, if either the R-R interval, the QRS waveform or the QRS energy content of Z_{i+1} deviates too strongly from the running average of these values, Z_{i+1} is regarded as incorrect. To evaluate the QRS waveform of Z_{i+1}, the inproduct

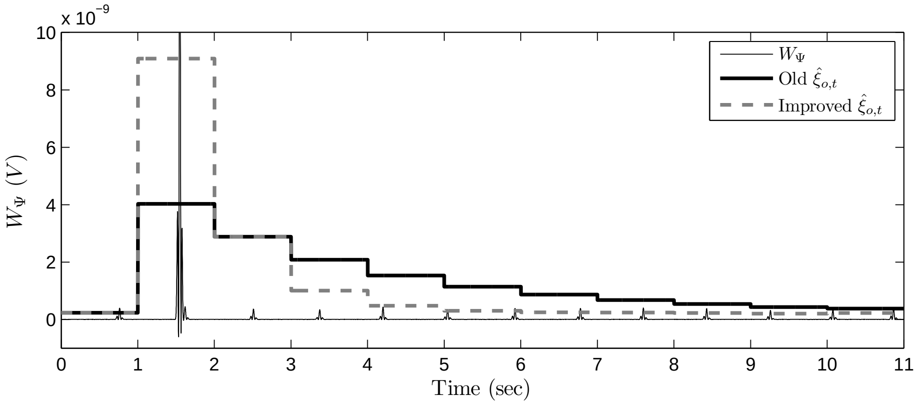

Figure 4.6 – *The effect of an artifact on the original and improved threshold $\xi_{o,t}$ of the peak detection algorithm of Vullings et al. In the implementation of previous studies, $\xi_{o,t}$ is unable to rapidly return to the basal threshold value after the artifact (rigid line). After correct implementation, $\xi_{o,t}$ is able to rapidly return to basal threshold value (dotted line).*

of Z_{i+1} is taken with Z_{ave}. Furthermore, the energy of Z_{i+1} is compared to the energy of Z_{ave}. The maximum allowed deviation from the average R-R interval is denoted as C_{RR}, the minimum required inproduct with Z_{ave} as C_I, and the maximum allowed deviation from the energy of Z_{ave} as C_E. Since little is known in the literature about the values of C_{RR}, C_I, and C_E, and the latter two are dependent on the used Source-Separation technique, these values have yet to be determined. The estimation of these values is discussed in more details in section 4.3.3.

The R-R interval and the QRS waveform in S might strongly vary per measurement and throughout a measurement. Since this information is not a priori known, an initialization phase is required to obtain a first estimation of the average R-R interval and Z_{ave}. The initialization phase searches for m consecutive peaks for which all individual R-R intervals are within the physiological R-R boundaries (50-255 BPM in accordance with the values used in [51]) and no R-R interval exceeds over C_{RR} percent of their average value. After m QRS complexes have been identified, these QRS complexes are stored in a buffer. The buffer QRS complexes are then used to generate S_{PBSSi}, after which Z_{ave} is determined. If no m QRS complexes are found that meet these criteria in an entire measurement, the measurement is not used for subsequent (spectral) analysis. The choice for the value of m is a trade-off between rapid activation of PBSSi on the one side and robustness against mis-detections on the other side, and is chosen 15.

After m buffer QRS complexes are found by the initialization, the first of the buffer QRS complexes is used as a starting point for further analysis. If a new legitimate QRS complex Z_{i+1} is identified by the QRS analysis, Z_{i+1} replaces the oldest buffer QRS complex in order to update the average R-R interval and Z_{ave}.

Each newly encountered QRS complex is first evaluated for its waveform and energy content. To compare the waveform of Z_{i+1} to Z_{ave}, both Z_{i+1} and Z_{ave} are normalized and base-line fluctuations are is suppressed by a fourth order Butterworth high-pass filter with cutoff frequency of 1.5 Hz. The pre-processed QRS complexes $\hat{Z}_{i+1}$ and $\hat{Z}_{ave}$ are then compared by means of their inproduct:

$$I_{i+1} = |\hat{Z}_{i+1} \cdot \hat{Z}_{ave}^{T}| \tag{4.3}$$

Due to the normalization of Z_{i+1}, any information regarding the energy content is lost in $\hat{Z}_{i+1}$. Therefore, besides the inproduct, a separate evaluation is performed for the energy of Z_{i+1}. If I_{i+1} is less than the minimum required inproduct C_I, or the energy of Z_{i+1} is either larger than C_E or smaller than $\frac{1}{C_E}$ times the energy of Z_{ave}, the complex Z_{i+1} is marked as false and is discarded.

Besides a sanity check of the QRS waveform and QRS energy, an expectation region is defined in which a new QRS complex should be present based on the location of the last previously determined correct QRS complex Z_i. The width of this expectation region is chosen as a percentage of the average R-R interval and is dependent on the Surrounding-Signal-Quality (SSQ in Eq. 3.29) in S_{opt} of the detected QRS complex Z_{i+1}. The effect of a variable expectation region is schematically shown in Fig. 4.7a and b. If the SSQ is high ($N_l \leq 6/8$ [51]), a wide expectation region can be used, since it is fairly certain that the fetal R-peak exceeds the noise and hence Z_{i+1} is a legitimate QRS complex. On the other hand, if the SSQ of Z_{i+1} is low ($N_l \geq 6/8$ [51]), it is much more likely that noise exceeds the fetal R-peak and causes a mis-detection. In this case a narrow expectation region is chosen. Note that the SSQ might also be high in case an artifact is detected as R-peak, however, these artifact peaks have already been discarded in an earlier stage by the energy evaluation.

To determine the width of the expectation region, two average R-R intervals are used. The first average is the temporal R-R interval (RR_{temp}), defined as the average R-R interval of the last 5 buffer complexes. The second average is the base-line R-R interval (RR_{base}), defined as the average R-R interval of all m buffer complexes. The temporal character of RR_{temp} allows for a good sensitivity to rapid heart rate fluctuation, however, RR_{temp} is also strongly influenced by mis-detections that causes incorrect estimation of the actual heart rate. In case RR_{temp} increases over two times the actual average R-R interval due to mis-detections, two R-peaks could be present within the expectation region, leading to a missed R-peak. To prevent RR_{temp} to exceed over two times the actual average R-R interval, RR_{base} is used to provide an upper boundary for RR_{temp}.

The start (δS_s) and end (δS_e) of the expectation region are given then by

$$\delta S_s = Z_i + \max\{(1 - \beta C_{RR}) \cdot RR_{temp},\ RR_{min}\} \tag{4.4}$$

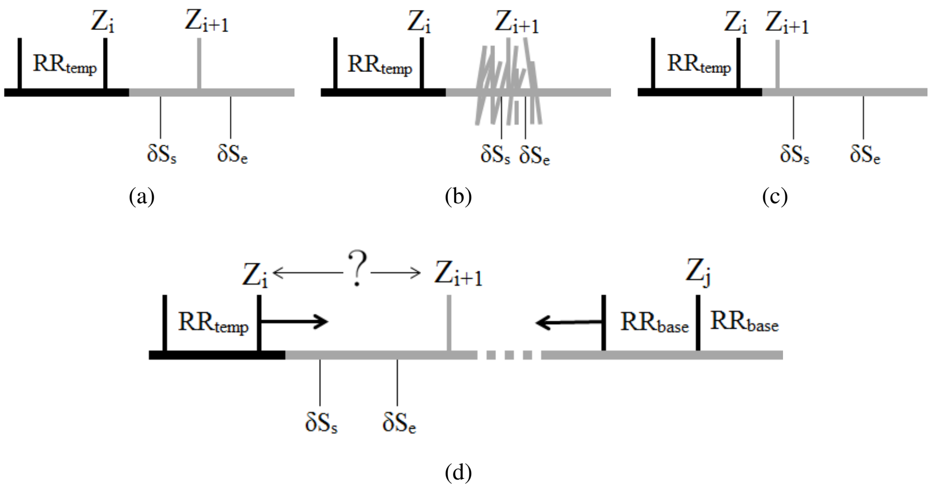

(a) (b) (c)

(d)

Figure 4.7 – *Schematic illustration of the QRS analysis algorithm. The region that has already been analysed is indicated in black and the region to be analysed in gray. (a) The next QRS complex Z_{i+1} is located within the expectation region and the QRS analysis continues using Z_{i+1} as a starting point. (b) The SSQ of Z_{i+1} is low ($N_l \geq 6/8$) and a narrow expectation region is used. (c) Z_{i+1} is located prior to δS_s, either due to an extra-systole or due to a mis-detection. (d) Z_{i+1} is located after δS_e. A future correct QRS complex Z_j is found, and the region between Z_i and Z_j is investigated for an arrhythmia or a missed peak.*

$$\delta S_e = Z_i + \min\{(1+\beta C_{RR}) \cdot RR_{temp},\ \ (2-C_{RR}) \cdot RR_{base},\ RR_{max}\} \tag{4.5}$$

where RR_{min} and RR_{max} are the minimal and maximal physiologically possible R-R intervals (based on $50-255$ BPM). The factor β depends on SSQ and is set to

$$\beta = \begin{cases} 1\ ;\ N_l \geq 6/8 \\ 2\ ;\ N_l \leq 6/8 \end{cases}$$

The following scenarios can occur: either the next QRS complex Z_{i+1} is found before, within or after the expectation region (Fig. 4.7 c, a, and d respectively). Note that both peak detection algorithms of Vullings et al. and Rooijakkers et al. already assume a minimal R-R interval from the refractory period of the pacemaker cells and it is impossible that multiple peaks are found within the expectation region.

- In case Z_{i+1} is found within the expected region, it is identified as legitimate and the QRS complex is added to the buffer. The location of Z_{i+1} is subsequently used as the last previous correct QRS complex and the analysis is repeated with Z_{i+1} as a new starting point.

- If the location of Z_{i+1} is in front of δS_s, this could be due to an extra-systole, which is discussed in the intermezzo concerning arrhythmias at the end of this chapter. If Z_{i+1} is not an extra-systole, it is discarded and Z_i is again used as starting point.
- In case Z_{i+1} is found after δS_e, this can either be due to an abnormal increase of the RR interval or due to a missed peak. The case of a sudden substantial increase in R-R interval is already described by Van Leeuwen et al. [115] and is discussed in the intermezzo concerning arrhythmias at the end of this chapter.

Despite the possibility of arrhythmia, the cause for an abnormal increase in R-R interval are most likely missed QRS complexes. Since either multiple QRS complexes might have been missed or the HRV in the region is high, the distance between Z_i and Z_{i+1} may significantly deviate from $a \cdot RR_{temp}$, with a an integer. Therefore, little is known about the correctness of the position of Z_{i+1} and, before a local search for missed QRS complexes, the algorithm searches for a new future correct QRS complex (Z_j). The complex Z_j has to meet the criteria that, besides correct waveform and energy, both the R-R interval prior to Z_j and the R-R interval after Z_j are within C_{RR} percent of RR_{base}. This is schematically shown in Fig. 4.7d. Although defining the Z_j extends the region that needs to be examined for missed QRS complexes (since $j \geq i+2$), this does ensures that the analysis eventually resumes at a correct location. If no Z_j is found within $V_{2,buf}$, $V_{2,buf}$ is updated.

For the residual region between Z_i and Z_j a search for local maxima in S_{opt}. The window of the local search is based on a multiple of RR_{temp} and the width of the window is chosen $C_{RR} \cdot RR_{temp}$. For each potentially missed QRS complex, the waveform and energy is compared to Z_{ave}. If no legitimate QRS complex is found, a peak is interpolated on the expected location of the missed QRS complex. Any QRS complex that is identified as a legitimate QRS complex but is located in between two interpolated QRS complexes, is discarded. After the entire region between Z_i and Z_j is examined, Z_j is used as starting point for further analysis.

4.3 Methodology of implementation and evaluation of developed algorithms

This section discusses the implementation and evaluation of the peak detection algorithms of Vullings et al. and Rooijakkers et al., the QRS analysis, and the PBSSi. Since annotation is used for both the implementation and the evaluation of all developed algorithms, this section first discusses the annotation procedure and the used evaluation criteria. Then, the implementation of the peak detection algorithms and QRS analysis is discussed. Finally, the methodology of evaluation of each of the developed algorithms is discussed separately.

4.3.1 Annotation and inter-observer variability

The annotation of two databases is described here. The first database is used for the optimization and evaluation of peak detection algorithms for maternal R-peak detection and consists of the adult ECG recordings of the MIT/BIH arrhythmia database (MITDB) [116]. The second database is used for the implementation and evaluation of the algorithms involved in fECG extraction and consists annotated fECG recordings of a subset of the IHDB (section 4.1).

MITDB The MITDB consists of 48 visually annotated thoracic measurements of 30 minutes and contain a two lead adult ECG. Of these two leads, only the first lead is used in the our evaluation. The heart rate in the MITDB are assumed to be representative for the maternal heart rate. In the MITDB, annotation is performed independently by multiple cardiologists and disagreements were resolved to obtain approximately 110,000 annotations. The heart rates in the MITDB are assumed to be representative for the maternal heart rates

Subset of the IHDB The second annotation set consists of a subset of the IHDB. To ensure that the fECG for all gestational ages is present in the subset, measurements of the entire IHDB are divided into six groups, based on the weeks of gestation (weeks+days of gestation):

- group 1: 17+0 - 20+6
- group 2: 21+0 - 24+6
- group 3: 25+0 - 28+6
- group 4: 29+0 - 32+6
- group 5: 33+0 - 36+6
- group 6: 37+0 - 40+

Per group four patients are randomly selected, with the additional criteria that of each patient only one measurement can be included in the subset. From each measurement, a segment of 200 seconds is randomly selected and used for annotation. Hence, the subset consists of 24 recordings with a total length of 80 minutes. The observer is unaware of the patient or the weeks of gestation.

For the entire subset, the mECG is subtracted from the data by WAMES and PBSS is used to generate the projected signal S_{PBSS}. Annotation is performed in three stages by an single observer that is familiar with the fECG in the abdominal recordings. A flow chart of the annotation process is displayed in Fig. 4.8. Firstly,

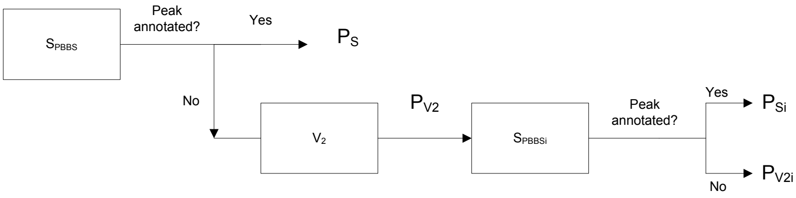

Figure 4.8 – *Flow chart of the annotation process. A first annotation is performed in the projection signal generated by PBSS. These peaks are denoted as P_S. In regions where no P_S is found, annotation is performed in the lead signals V_2. Peaks in the lead signals are denoted as P_{V_2}. A final annotation is also performed in the projection signal generated by PBSSi, in the regions where no peak is found in S_{PBSS}. The peaks that are found in S_{PBSSi} and not in S_{PBSS} are denoted as P_{Si}.*

an entire segment is annotated in S_{PBSS}. Peaks found in S_{PBSS} are denoted as P_S. Secondly, for any residual regions where no P_S was found, annotation is performed in V_2. The peaks that are found in V_2 are denoted as P_{V_2}. A final annotation is performed in the projection signal generated by PBSSi, in the regions where no P_S is found. The peaks annotated in S_{PBSSi} in the final annotation are denoted as P_{Si} and the peaks that are still only found in V_2 as $P_{V_{2i}}$. The reason for this annotation procedure becomes clear from the used evaluation criteria that are explained in section 4.3.2.

To determine the inter-observer variability for the annotation of the subset of the IHDB, the S_{PBSS} of 12 of the 24 segments are annotated by a second independent observer. Whereas the first observer is already familiar with the abdominal recordings and the processing techniques, the second observer is an expert in neonatology. The Cohen's Kappa test is used to evaluate the inter-observer agreement. The details of this statistical test are explained in Appendix B.

4.3.2 Evaluation criteria

The criteria used to evaluate all developed algorithms are discussed in separate paragraphs. Which of these criteria are used for the evaluation of each individual algorithm, is discussed in section 4.3.4.

Peak location The performance of the developed algorithms is described by the number of True-Positives (nTP, correctly detected peaks), False-Positives (nFP, falsely detected peaks) and False-Negatives (nFN, missed peaks). In line with previous studies [51, 117, 118], a peak is considered to be correct if it is located within a 100ms interval around an annotated peak.

To quantify the performance, three measures are used: the Sensitivity (Se), the

Positive-Predictive-Value (PPV) and the Error-Rate (De)

$$Se = \frac{nTP}{nTP+nFN} \tag{4.6}$$

$$PPV = \frac{nTP}{nTP+nFP} \tag{4.7}$$

$$D_e = \frac{nFP+nFN}{nTP+nFN} \tag{4.8}$$

The Se is a measure for the number of missed peaks, whereas the PPV is a measure for the number of falsely detected peaks. The D_e provides a measure for the overall performance of the algorithm, as it gives the ratio between the total number of false detections (FP and FN) and the total number of annotated peaks (TP and FN). High Se and PPV, and low D_e indicate good performance.

WAMES processing errors Although the annotation of the MITDB provides objective measure for the performance of peak detection algorithms for features of the mECG (e.g. heart rate variations), the thoracic recordings of the MITDB are not necessarily representative for the characteristics of the abdominal recordings of the IHDB (e.g. SNR and artifacts). Since processing errors involving the mECG subtraction in WAMES typically originate from non-physiological values that are caused by incorrect maternal R-peak detection, the number of processing errors in WAMES is used as an objective measure for the performance of peak detection algorithms for the maternal R-peak detection in the IHDB.

Annotation of P_{V_2} Due to the limitation of visual annotation in the subset of the IHDB, some peaks that are not annotated in S_{PBSS} and only in V_2 might have been found by a developed algorithm. Since the number of found P_{V_2} might differ per algorithm, found P_{V_2} cannot be accounted for to obtain an objective measure of Se, PPV, and D_e. In the calculation of the Se, PPV, and D_e, these peaks are thus identified as FPs if the developed algorithms are compared to P_S, although they are actually TPs. Therefore, the number of found P_{V_2} is displayed separately in the results.

Annotation of P_{Si} The number of P_{V_2} that is initially not annotatable in S_{PBSS} but that is annotatable in S_{PBSSi} is a directly related to the improvements on the Source-Separation.

SNR Improvements on the Source-Separation can also be quantified by the SNR. The exact SNR is difficult to measure. For example, Rooijakkers et al. defined the SNR as the ratio between the R-peak amplitude and the maximum amplitude in the surroundings of the R-peak [51] in the wavelet-transformed fECG. This, however, is not a true measure of SNR, since the amplitudes are determined in a transformed signal. Besides, with this method, an artifact that is falsely identified as an R-peak and has a large amplitude compared to an actual fetal R-peak, will give a high SNR, although this is obviously not true.

Vullings et al. measure SNR by comparing an running average QRS complex $\hat{Z}_{ave}$ in S_{PBSS} to the individual QRS complexes $\hat{Z}_i$ in S_{PBSS} [48]. This measures the actual ratio between S_{PBSS} with and without the QRS complexes. In case of a mis detection, the false QRS complex does not correlate well with the average QRS complex and a low SNR is obtained. Since this measurement is more related to the true SNR, this is used to calculate the SNR. The SNR of Z_i ($\Psi_{SNR,i}$) is calculated as

$$\Psi_{SNR,i}(dB) = 10\log\frac{\hat{Z}_{ave}\cdot\hat{Z}_{ave}^T}{(\hat{Z}_i-\hat{Z}_{ave})(\hat{Z}_i-\hat{Z}_{ave})^T} \tag{4.9}$$

4.3.3 Implementation of developed algorithms

The implementation of the peak detection algorithms of Vullings et al. and Rooijakkers et al., and the QRS analysis requires to experimentally determine multiple parameters. This section discusses the parameters of interest and the method used to determine their values.

Parameter optimization for peak detection

Optimal settings for the peak detection algorithms of Vullings et al. and Rooijakkers et al. are found by minimization of D_e. Due to the difference in features of the mECG and the fECG, optimal settings for the peak detection algorithms are determined separately for the maternal and fetal R-peak detection. To find the optimal settings for maternal R-peak detection, the peak detection algorithms are compared to the annotation of the MITDB. Optimal settings for fetal R-peak detection are found by comparing the peak detection algorithms to P_S of the annotated subset of the IHDB.

The parameters that need to be optimized the algorithm of for Vullings et al. for the length-transformation are the length of the integrating window M_{QRS}, the cutoff value of the high-pass filter HP, and the cutoff value for the low-pass filter LP. The parameters of the Bayesian thresholding are the constant g used to calculate the instantaneous threshold, and the lower and upper limit of the Kalman Gain K^{min} and K^{max}. All starting values of the optimization parameters are displayed in Table 4.1. To limit the number of iteration required to simulate all combinations of these parameters, the optimal settings for the length-transformation are estimated first, while using the literature values for thresholding parameters ($g = 0.3$, $K^{min} = 0.3$ and $K^{max} = 0.7$). The best performing values for the parameters of the length transformation are then

Table 4.1 – *Parameters used for the optimization of the peak detection algorithm of Vullings et al. In total, 531 and 423 combinations of starting values are used for the optimization of Vullings et al. for maternal and fetal R-peak detection, respectively.*

Vullings	Maternal	Fetal	Step size
M_{QRS}	40-80 ms	30-60 ms	5 ms
HP	2.5-15 Hz	2.5-15 Hz	2.5 Hz
LP	20-40 Hz	50-70 Hz	2.5 Hz
g	0.1-0.9	0.1-0.9	0.1
K^{min}	0.1-0.5	0.1-0.5	0.1

Table 4.2 – *Parameters used for the optimization of the peak detection algorithm of Rooijakkers et al. In total, 99 and 189 combinations of starting values are used for the optimization of Rooijakkers et al. for maternal and fetal R-peak detection, respectively.*

Rooijakkers	Maternal	Fetal	Step size
Fc	15-25 Hz	30-50 Hz	1 Hz
α	0.1-0.9	0.1-0.9	0.1

used to find the optimal settings for the thresholding. Furthermore, K^{max} is chosen as $1 - K^{min}$.

For Rooijakkers et al. the central frequency F_c of the wavelet and the threshold constant α have to be optimized (Table 4.2).

Parameters for QRS analysis

In the literature, little is known about the parameters that are involved in the QRS analysis (C_{RR}, C_I and C_E), and part of these parameters depends on the used Source-Separation technique. The optimal values of C_{RR}, C_I and C_E are, therefore, experimentally obtained from the annotated subset of the IHDB.

Using the annotation of the subset of the IHDB, distributions are obtained for the ratio between the R-R interval and a running average R-R interval, the inproduct of individual QRS complexes with a running average QRS complex, and the ratio of the energy an individual QRS complex and a running average QRS complex. The values of C_{RR}, and C_E are estimated based on the 5% and 95% interval of the corresponding distributions. The value of C_I is estimated based on the 5% interval of the distribution of the absolute inproduct values.

Note that annotation of the subset of the IHDB is performed in the untransformed fECG recording (either in S_{PBSS}, V_2, or S_{PBSSi}), in contrast to the peak detection algorithms that use a transformed fECG (either SAD or wavelet-transformed). As a result, the annotation requires a certain quality of the shape of a QRS complex which might not be necessary in the algorithmic detection. In order to include correctly detected peaks that are difficult to identify visually in the untransformed fECG but might become distinct in the transformed ECG, the values for C_{RR}, C_I, and C_E are chosen more flexible than the found 5% and 95% values in the distributions.

To obtain a distribution for the ratio between the R-R interval of individual complexes and a running average of the R-R interval, the average of 5 consecutive annotated peaks is calculated (based on RR_{temp}). R-R intervals that exceed 430ms (140BPM) by at least 80% are not taken into account for calculation of RR_{temp}. To obtain a distribution for the absolute value of the inproduct, 15 consecutive QRS complexes are used to generate the running average QRS complex (Z_{ave}). The absolute value of the inproduct of each annotated QRS complex with Z_{ave} is then calculated. Z_{ave} is also used to obtain a distribution for the ratio of the energy of an individual QRS complex and the energy of Z_{ave}.

4.3.4 Evaluation of the developed algorithms

After settings are determined for the peak detection algorithms of Vullings et al. and Rooijakkers et al., and the QRS analysis, the performance of all developed algorithms is evaluated. Since different evaluation criteria and methods are used for different algorithms, these are discussed individually for each algorithm.

Peak detection The performance of the peak detection algorithms of Vullings et al. and Rooijakkers et al. for maternal R-peak detection is based on the S_e, PPV, and D_e in the MITDB. Besides the Se, PPV, and D_e, the number processing errors in WAMES serves as a second measure for the performance of the peak detection algorithms for maternal R-peak detection, and, therefore, both Vullings et al. and Rooijakkers et al. are used in WAMES to subtract the mECG from all the abdominal recordings of the IHDB.

For fetal R-peak detection, peak detection algorithms are compared to P_S of the subset of the IHDB and performance is based on the Se, PPV, and D_e. Besides, the number of found P_{V_2} by the detection algorithms is also considered in the results.

QRS analysis Similar to the performance of the peak detection algorithms for fetal R-peak detection, the performance of the QRS analysis is evaluated with respect to P_S (using the Se, PPV, D_e) and the number of found P_{V_2}.

Source-Separation A first measure to compare the performance of PBSSi to PBSS is provided by the number of P_{Si}. As a second measure, a comparison is made between the SNR of the QRS complexes in S_{PBSS} and S_{PBSSi}. The SNR is only calculated for QRS complexes that are both annotated and detected by the algorithm. Note that PBSSi is always used in combination with QRS analysis and only becomes operative after initialization. Hence, the comparison of PBSS and PBSSi is only performed in regions after these m consecutive peaks are identified by the initialization.

fECG extraction algorithm The goal of the fECG extraction algorithm developed in this thesis (illustrated by the flowchart in 4.3) is to detect all R-peaks, regardless whether peak are annotated in S_{PBSSi} or P_{V_2}. Therefore, unlike the evaluation of the peak detection algorithms and the QRS analysis, the performance of the fECG extraction algorithm is evaluated with respect to both P_{Si} and $P_{V_{2i}}$.

4.4 Performance of STFT and CWT

In [100], a comparison is made between the STFT and the CWT for the influence of artifact correction on the heart rate signal with interpolation. This study shows that the STFT only allowed for 5% interpolation, whereas CWT is still reasonably accurate for 20% interpolation. However, this study is limited to simulations of artifact corrections and assumes that the location of an artifact is known. Since, in practice, mis-detections often remain unidentified an disturb the heart rate signal, the influence of these mis-detections on the spectral parameters should also be addressed. Besides the influence of a mis-detection on the spectral parameters, [100] gives no indication about the influence of consecutively interpolated R-R intervals. In this thesis, the performance of STFT and CWT for heart rate signals that contain simulated mis-detections and heart rates with consecutively interpolated R-R intervals are evaluated.

To investigate the influence of unidentified mis-detections and consecutively interpolated R-R intervals on the spectral parameters of the STFT and the CWT, 10 artifact free fetal heart rate signals of 64 seconds are selected. The length of 64 seconds is based on the length of heart rate signals used in previous studies to determine spectral parameters of the fetal HRV [119].

The influence of one mis-detection in a 64 second segment is simulated by deviating one randomly selected peak from its actual position (Fig. 4.9a). The deviation is varied from -80ms to +80ms with a step size of 10ms. For each segment, this procedure is repeated 10 times with a different randomly selected artifact peaks. Hence, for each deviation value a total of 100 spectral values are obtain (10 iteration in 10 different files).

Besides the influence of one mis-detection, the influence of multiple mis-detection is investigated for up to 5 mis-detections (Fig. 4.9b). The deviation from the actual position of each mis-detection is randomly generated between ±50ms (minimum deviation of ±10ms). This is simulated 10 times for each segment. Hence, for each number of mis-detections, 100 values are obtained.

The influence of the number of consecutively interpolated R-R intervals is investigated for up to 15 consecutive R-R intervals (Fig. 4.9c). This procedure is repeated 10 times for each segment. Hence, for each number of consecutive interpolated R-R intervals, there are 100 simulations.

If either the 25th or the 75th percentile of the relative deviation of the spectral parameters exceeds 5% of the spectral parameters of the artifact free heart rate signal, this is defined as unacceptable.

Intermezzo: Arrhythmias

This intermezzo describes the detection of arrhythmias by means of the QRS analysis. There are numerous types of arrhythmias some of which are associated with pathological conditions. Arrhythmias, however, are beyond the scope of this thesis, and this intermezzo is only meant to show the potential for QRS analysis to detect arrhythmias. In this intermezzo two frequently occurring arrhythmias are discussed. Both of these arrhythmias occur in healthy fetuses and are not associated with any pathological condition. The first of the arrhythmia discussed here are extra-systole beats and the second is a sudden substantial increase in R-R interval. Criteria chosen in this preliminary detection of arrhythmias are experimentally determined and further study is required to obtain more accurate criteria.

The typically low SNR of the fECG does not always allows for the detection of arrhythmias, since mis-detections often show an R-R pattern similar to arrhythmias. To prevent false identification of arrhythmias, arrhythmias are only identified if certain conditions hold. To ensure that the starting point for the arrhythmia detection is a legitimate QRS complex (Z_i), a low HRV prior to the arrythmia is required (similar RR_{temp} and RR_{base}). Furthermore, the SSQ in the surrounding of all QRS complexes needs to be high (hence β is 2), all QRS complexes need to have a correct waveform and energy content, and no R-R interval between consecutive QRS complexes is allowed to exceed physiological boundaries of RR_{min} and RR_{max}. Imposing these conditions ensures a low probability of false identification of an arrhythmia, although it might also resolve in a lower sensitivity to detect arrhythmias.

Extra-systoles are caused by early muscular contraction of the ventricles, e.g. due to excitation in the AV-node [52]. Little is known about the exact sequence of extra-systoles and parameters for the detection of extra-systoles are hence chosen experimentally. A typical sequence of an extra-systole is a substantial decrease in R-R interval compared to a previous R-R interval (RR_{ref}), followed by a slight increase in R-R interval relative to RR_{ref}.

To identify a QRS complex Z_{i+1} as an extra-systole, the R-R interval between Z_{i-1} and Z_i is used as RR_{ref}. An extra-systole is defined if the R-R interval between Z_i and Z_{i+1} is less than $(1-C_{RR})\cdot RR_{ref}$ and the R-R interval between Z_{i+1} and Z_{i+2} is larger than RR_{ref}. As a final condition, the decrease in R-R interval prior to the extra systole needs to be at least a factor 1.2 larger than the increase in R-R interval (compared to RR_{ref}) after the extra systole. A case study of an heart rate contaminated with numerous extra-systoles is shown in Fig. 4.10.

Besides extra-systoles that are characterized by an abnormal decrease in R-R interval followed by a slight increase, an arrhythmia might also present itself as a sudden substantial increase in R-R interval. This sudden increase in R-R interval (over $(1+\beta C_{RR}) \cdot RR_{temp}$) is followed by a gradual decrease to the basal R-R interval and is thought to be caused by a block in the SA node. An example of such a sequence is displayed in Fig. 4.11.

Due to the characteristic gradual decrease to the basal R-R interval, these arrhythmias are easiest detected in a backwards manner. In the backwards analysis, the expectation region is defined in front of a previously analyzed QRS complex Z_{prev}. The start and end of the expectation regions are now given by

$$\delta S_s = Z_{prev} - \min\{(1+\beta C_{RR}) \cdot RR_{prev},\ ,(2-\beta C_{RR}) \cdot RR_{temp},\ ,RR_{max}\} \tag{4.10}$$

$$\delta S_e = Z_{prev} - RR_{min} \tag{4.11}$$

with RR_{prev} the R-R interval of Z_{prev}. By defining δS_s and δS_e as a percentage of RR_{prev} instead of as a percentage of RR_{temp}, the R-R interval is able to rapidly increase. Furthermore, δS_s is not allowed to exceed over two times the temporal RR_{temp}, since the risk still exists that QRS complexes are missed.

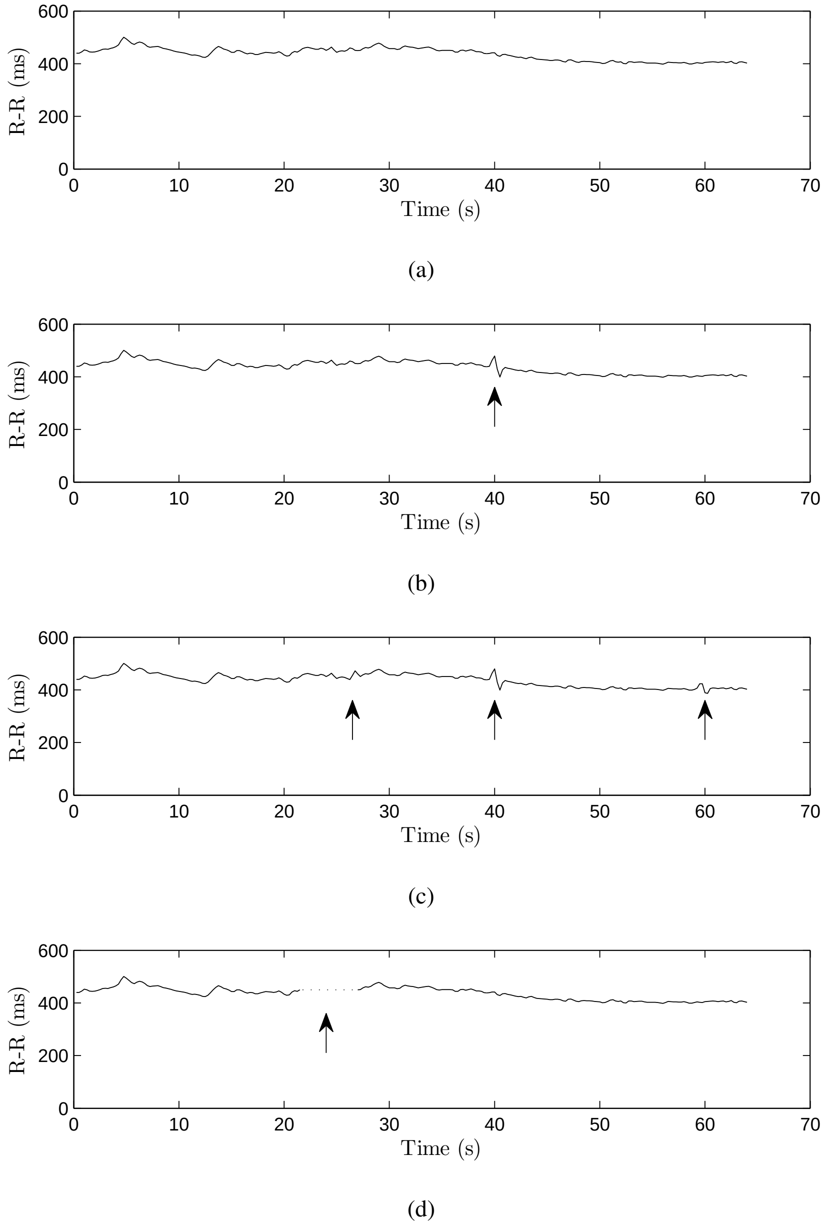

(a)

(b)

(c)

(d)

Figure 4.9 – *(a) Heart rate of an artifact free segment of 64 seconds. (b) The effect of a simulated mis-detection with a deviation of 40ms. (c) The effect of 3 simulated mis-detections with a deviation of -24ms, 37ms, and 41ms. (d) The heart rate with 10 consecutive interpolated peaks.*

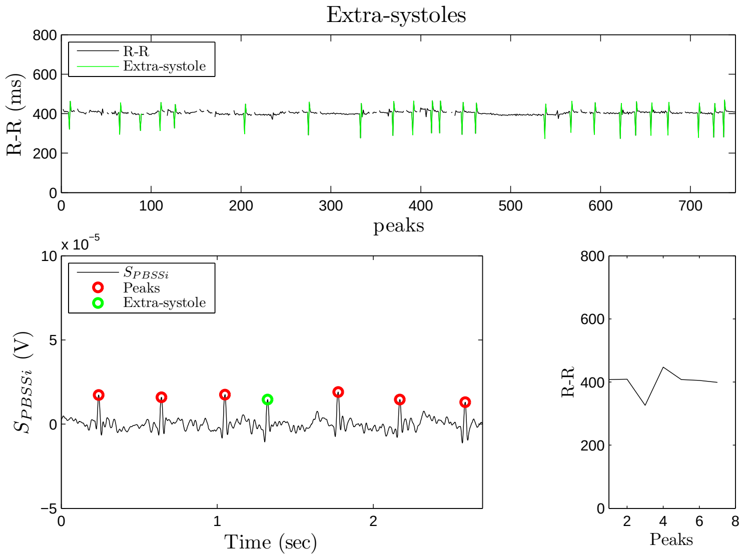

Figure 4.10 – *An example of a measurement that is contaminated with numerous extra-systolic beats (indicated in green). The upper graph displays the R-R interval of the measurement. An example of an extra-systole and its effect on the R-R interval is displayed in the bottom graphs.*

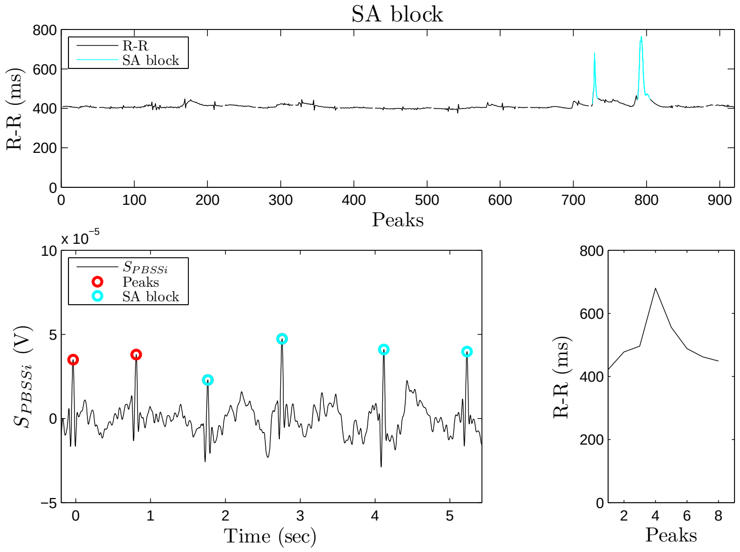

Figure 4.11 – *An example of a measurement that contained multiple SA-blocks (indicated in blue). The upper graph shows the R-R interval of the entire measurement. An example of an SA-block and the effect on the R-R interval is displayed in the bottom graphs.*

Chapter 5

Results

In this chapter the results are shown of the implementation and evaluation of the developed algorithms. Since annotation is used for the implementation and evaluation, the results of the annotation and the inter-observer variability are shown prior to the results of the implementation and evaluation. After the evaluation of the developed algorithms, the influence of simulated mis-detections and consecutively interpolated R-R intervals on the spectral parameters of the STFT and the CWT are displayed.

5.1 Annotation and inter-observer variability

To determine the inter-observer variability in the annotation of the subset of the IHDB, two observers have annotated 12 out of 24 files. The inter-observer agreement is quantified by the Cohen's Kappa test. The values used for the Cohen's Kappa test are shown in Table 5.1 and κ is found to be 0.73. According to the literature this means a good inter-observer agreement [120, 121]. Therefore, for further evaluation, the annotation of the observer that annotated all 24 files is used as the reference.

In the 24 recordings of the subset of the IHDB, in total 6377 peaks are annotated by observer one. Of these 6377 peaks, 4872 (76.4%) are annotated in S_{PBSS} and 1505 (23.6%) in the V_2. In 9 out of 24 (37.5%) files, less than 25 peaks are annotated (either P_S or P_{V_2}). The 15 files with more than 25 P_S are from here on denoted as *reliable*. In 2 (8.3%) files peaks are only found in the V_2 and not in S_{PBSS}. The distribution of the number of annotated peaks per GA group is displayed in Fig. 5.1.

5.2 Peak detection: results

5.2.1 Peak detection: implementation and optimization

To determine optimal settings for the maternal R-peak detection the entire MITDB is used, except for recording 207, which contains ventricular flutter episodes (heart rates over 200 BPM) [117] and is not representative for maternal heart rate patterns during pregnancy.

Table 5.1 – *Result of the annotation of 12 recordings of the subset of the IHDB performed by two observers. The values are used to determine the inter-observer agreement.*

	observer 2: Peak	observer 1: No peak
observer 1: Peak	2308	646
observer 1: No peak	105	2521

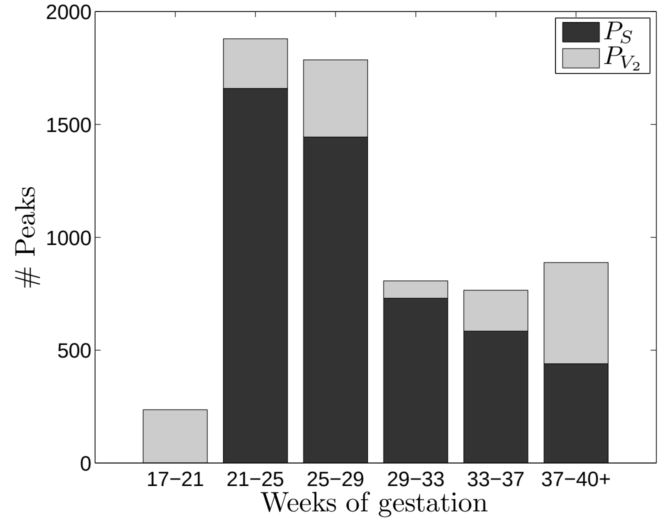

Figure 5.1 – *Distribution of the number of annotated peaks per weeks of gestation. Dark gray indicates peaks that are found in S_{PBSS} and light gray indicates the number of peaks that are only found in V_2.*

To determine optimal settings for the fetal R-peak detection, only reliable files are used. The optimal parameters for the peak detection algorithms of Vullings et al. and Rooijakkers et al. are displayed in Table 5.2. The literature value of each parameter is displayed between brackets after the found parameter in this thesis.

No difference is seen for changes in the value of K^{min} in the peak detection algorithm of Vullings et al. The value of K^{min} is, therefore, chosen equal to the literature value of 0.3.

5.2.2 Peak detection: evaluation

The peak detection algorithms for maternal R-peak detection are evaluated using the MITDB as reference. In addition, the number of processing errors in WAMES for mECG subtraction in the IHDB, as explained in section 4.3.4. The *Se*, *PPV*, and D_e for the MITDB are shown in Table 5.3. Of the 1076 files in the IHDB, WAMES is unable to subtract the mECG in 121 (11.25%) files with the original implementation of Vullings et al. With the improved implementation of the peak

Table 5.2 – *Optimal settings found for the peak detection algorithm of Vullings et al. (left) and Rooijakkers et al. (right). Literature values are displayed between brackets. For the peak detection of Vullings et al. no difference is found for changing K^{min} in both the maternal and fetal R-peak detection. Furthermore no difference is found for changing LP between 60 and 70Hz for fetal R-peak detection.*

Vullings	Maternal	Fetal
M_{QRS}	60 ms (65ms)	40 ms (40ms)
HP	2.5 Hz (2.5Hz)	12.5 Hz (20Hz)
LP	25 Hz (25Hz)	60-70 Hz (60Hz)
g	0.3 (0.3)	0.6 (0.3)
K^{min}	0.1-0.5 (0.3)	0.1-0.5 (0.3)

Rooijakkers	Maternal	Fetal
Fc	19 Hz (18Hz)	41 Hz (44Hz)
α	0.3 (0.3)	0.5 (0.3)

detection of Vullings et al., 94 (8.74%) files could not be processed and with the peak detection of Rooijakkers et al. 89 (8.27%) files could not be processed.

For the evaluation of the peak detection algorithms for fetal R-peak detection, the annotated subset of the IHDB is used. The Se, PPV, and D_e for the IHDB are shown in Table 5.4. The results if only reliable files are used are shown in the upper row and the results if all files are used in the bottom row. The number of P_{V_2} that are found by the detection algorithms is displayed in the right column.

The best performance for maternal R-peak detection is seen for Rooijakkers et al., because of the lowest D_e in the MITDB and the lowest number of processing errors in WAMES. Therefore, Rooijakkers et al. is chosen for mECG subtraction. Any residual processing error in WAMES is caused by the occurrence of non-physiological values in the estimation of the mECG due to the presence of artifacts. All processing errors are manually resolved in WAMES, leading to 0% processing errors in the mECG subtraction.

Besides the maternal R-peak detection, Rooijakkers et al. also performed best for the fetal R-peak detection if only the reliable files are accounted for and, hence, is used for fetal R-peak detection.

Table 5.3 – *Results for peak detection in the MITDB using the optimal settings of Table 5.2 for the original and improved implementation of Vullings et al., and Rooijakkers et al. The percentage of processing error in WAMES for the mECG subtraction in the IHDB is displayed in the right column.*

MITDB	$D_e(\%)$	$Se(\%)$	$PPV(\%)$	Error WAMES (%)
Vullings et al. original	0.66	99.57	99.76	11.25
Vullings et al. improved	0.60	99.62	99.78	8.74
Rooijakkers et al.	0.24	99.87	99.89	8.27

Table 5.4 – *Results for peak detection in the IHDB using the optimal settings of Table 5.2 for Vullings et al. and Rooijakkers et al. The peak detection algorithms are compared to P_S. The number of found P_{V_2} in addition to these results is shown in the right column.*

IHDB		$D_e(\%)$	$Se(\%)$	$PPV(\%)$	found P_{V_2} (%)
reliable	Vullings et al.	20.45	90.48	89.22	32.22
	Rooijakkers et al.	15.89	95.71	89.19	38.19
all	Vullings et al.	54.62	90.48	66.73	27.31
	Rooijakkers et al.	57.44	95.69	64.30	32.89

5.3 QRS analysis: results

5.3.1 QRS analysis: implementation

The values of C_{RR}, C_I, and C_E for the QRS analysis are estimated based on the distributions in Fig. 5.2. Note that the values for C_I and C_E are chosen more flexible compared to the values from the corresponding distributions for reasons explained in section 4.3.3.

The distribution of the R-R interval with respect to RR_{temp} is displayed in Fig. 5.2a, with a median (range: 5-95%) of 1.00 (range: 0.90-1.12). Based on the 5-95% interval, the value for C_{RR} is chosen as 10% of RR_{temp}.

The distribution of the absolute value of the inproduct of the individual QRS complexes with $\hat{Z}_{ave}$ is displayed in Fig. 5.2b, with a median (range: 5-95%) of 0.97 (range: 0.70-1.00). Based on the 5% boundary, to value is of C_I is chosen 0.6.

Finally, the distribution of the energy ratio of individual QRS complexes and $\hat{Z}_{ave}$ is displayed in Fig. 5.2c, with a median (range: 5-95%) of 1.14 (range: 0.53-3.03). Based on the 5-95% interval C_E is chosen 4.

5.3.2 QRS analysis: evaluation

The performance of the QRS analysis in addition to PBSS and Rooijakkers et al. is shown in Table 5.5.

Overall, the performance of QRS analysis in addition to Rooijakkers et al. for the reliable files is almost similar to Rooijakkers et al. However, it seems as if the

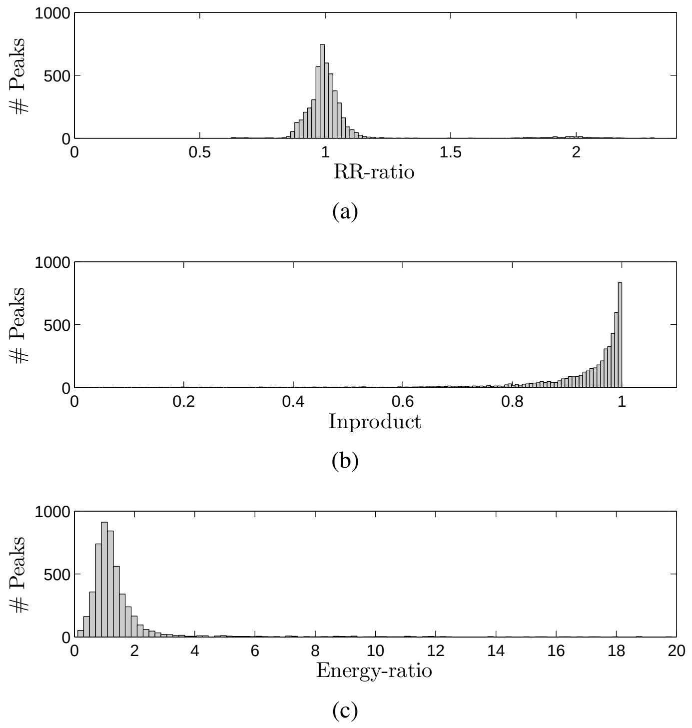

Figure 5.2 – *Distributions based on the peaks annotated in* S_{PBSS}*. a) Distribution of the ratio of the R-R interval of individual QRS complexes with a running average R-R interval. b) The inproduct of individual QRS complexes with* Z_{ave}*. c) The ratio between the energy content of individual QRS complexes and the energy content of* Z_{ave}*.*

Table 5.5 – *Performance of the QRS analysis in addition to Rooijakkers et al. Results are compared to* P_S *and the number of found* P_{V_2} *in addition to these results is displayed in the right column.*

IHDB		$D_e(\%)$	$Se(\%)$	$PPV(\%)$	found P_{V_2} (%)
reliable	QRS analysis	16.73	95.80	88.43	44.51
all	QRS analysis	19.63	95.78	86.14	28.50

PPV has decreased and the Se has slightly increased with respect to the results of Rooijakkers et al. for reliable files, despite the implementation of more restrictions by the QRS analysis. This decrease in PPV is caused by the increase in the percentage of P_{V_2} found by QRS analysis, which is not taken into account in the calculation of the D_e, Se, and PPV. If the number of found P_{V_2} is accounted for, the D_e is also slightly lower for the reliable files compared to Rooijakkers et al. (8.25% and 8.59%, respectively). The true contribution of the QRS analysis, however, becomes clear if all files of the subset of the IHDB are used, for which the D_e is substantially lower.

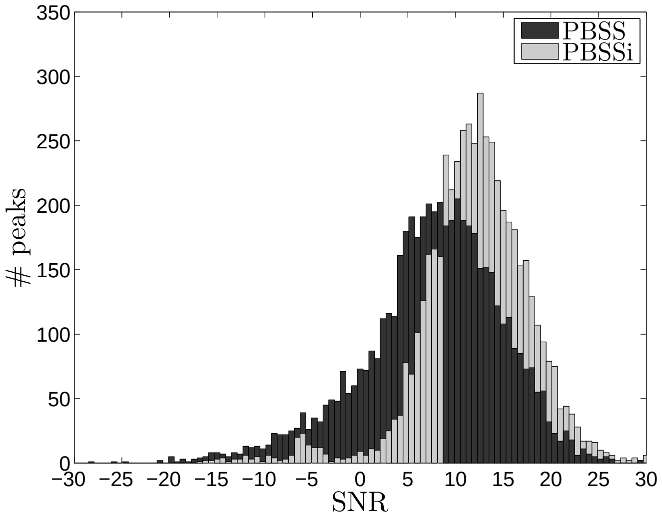

Figure 5.3 – *Distribution of the SNR for annotated peaks in S_{PBSS} and S_{PBSSi}. The distribution only contains peaks that are both annotated and detected by the algorithm.*

5.4 Source-Separation: results

The improvements of PBSSi compared to PBSS are quantified by two measures. In the regions after the initialization phase of the QRS analysis, 725 P_{V_2} are annotated in the first annotation. Of these, 559 (77.10%) are found in the S_{PBSSi} in the second annotation. The SNR distribution for both the annotated peaks in S_{PBSS} and S_{PBSSi} are displayed in Fig. 5.3. The median (range: 5-95%) of PBSS is 8.16 (range: −6.0-18.3) and for PBSSi 12.3 (range: 3.6-20.6).

The improvements of PBSSi compared to PBSS changes the distribution of the inproduct values of the individual QRS complexes and a running average QRS complex (not displayed). The new median (range: 5-95%) of the distribution of the inproduct for QRS complexes in PBSSi is 0.99 (range: 0.90-1.00). The value for C_I is, therefore, chosen 0.8.

5.5 fECG extraction algorithm: results

An example of the extracted fetal heart rate of a 20 minute recording that is processed by the state-of-the-art techniques of PBSS in combination with Rooijakkers et al. (also shown in Fig. 3.6), is shown in the upper graph of Fig. 5.4. The bottom graph displays the result of the same recording, processed by the fECG extraction algorithm developed in this thesis.

The performance of the PBSS in combination with Rooijakkers et al. and the performance of the algorithm developed in this thesis are shown in Table 5.7. Detected

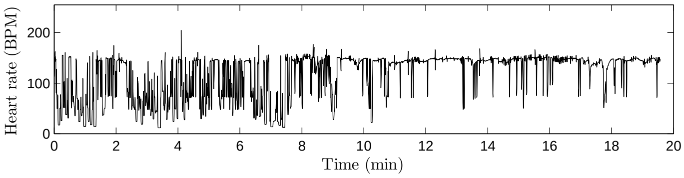

(a) PBSS + Rooijakkers et al.

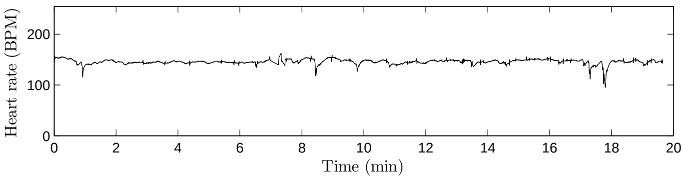

(b) PBSSi + QRS analysis

Figure 5.4 – *Example of the extracted fetal heart rate of the 20 minute measurement (also displayed in Fig. 3.6). (a) The result after processing with PBSS in combination with the peak detection algorithm of Rooijakkers et al. (b) The result after processing with the fECG extraction algorithm developed in this thesis.*

Table 5.6 – *Performance of the state-of-the art techniques (PBSS in combination with Rooijakkers et al.) and the algorithm developed in this thesis. Results are compared to both P_{Si} and P_{V_2} of the second annotation.*

New Anno IHDB		$D_e(\%)$	$Se(\%)$	$PPV(\%)$
reliable	PBSS + Rooijakkers	17.21	87.64	94.76
	This work	**6.52**	**94.02**	**99.44**
all	PBSS + Rooijakkers	51.56	81.27	71.23
	This work	**17.92**	**86.58**	**95.05**

peaks are compared to P_{Si} and $P_{V_{2i}}$.

5.6 Performance of STFT and CWT

The relative deviations of the spectral parameters for one simulated mis-detection, for multiple mis-detections, and for consecutively interpolated peaks in a 64 second segment are shown in Fig. 5.5, 5.6, and 5.7 respectively. The influence on the absolute and normalized LF power is displayed in the upper graphs, and the influence on the absolute and normalized HF power is displayed in the bottom graphs. The central point in each box is the median, the edges of the boxes in the graphs indicate the 25th and 75th percentiles, and the whiskers extend to the most extreme data points that are not considered outliers. Outliers are defined as data points that lie outsize $\pm 2.7\sigma$ (or 99.3%) when the data would be assumed normally distributed. Outliers are not dis-

Table 5.7 – *Table presentation.*

Technique	$Se(\%)$	$PPV(\%)$
Existing techniques	81.27	71.23
Newly developed algorithm	**86.58**	**95.05**

played. Furthermore, since the relative deviation of the HF and normalized HF power in Fig. 5.5 and 5.6 are of a different order of magnitude than the relative deviation of the LF and normalized LF power of the other graphs, the axes for HF and normalized HF are scaled differently with respect to the axes for LF and normalized LF.

For one mis-detection, the 25th or 75th percentile of the relative deviation of the spectral parameters with STFT does not exceed 5% for the absolute LF power. For the absolute HF power the 5% boundary is exceeded after a mis-detection of 10ms, for the normalized LF after 20ms, and for the normalized HF after 10ms. If CWT is used, the 25th or 75th percentiles of the relative deviation of the absolute LF power only exceed 5% for a mis-detection of 80ms. The 25th and 75th percentiles for all other spectral parameters are less than 5%.

For multiple mis-detections, the 25th or 75th percentile of the relative deviation of the spectral parameters with STFT does not exceeds 5% for the absolute LF power. For the other spectral powers this occurs after 1 mis-detection. If CWT is used, the 25th or 75th percentiles of the relative deviation exceed 5% after 4, 3, 3, and 3 mis-detections for the absolute LF and HF, and the normalized LF and HF, respectively.

For consecutively interpolated peaks, the 25th or 75th percentile of the relative deviation of the spectral parameters with STFT, exceed 5% for 11, 5, and 5 consecutively peaks for the respective absolute LF, absolute HF and normalized HF power. For the normalized LF power, the 25th or 75th percentile does not exceed 5% relative deviation. For the CWT, the 25th or 75th percentile of the relative deviation of the spectral power exceed 5% after 10, 10, and 15 consecutively interpolated peaks for the respective absolute LF, normalized LF, and normalized HF. The 25th and 75th percentiles for the absolute HF and the normalized LF are all less than 5%.

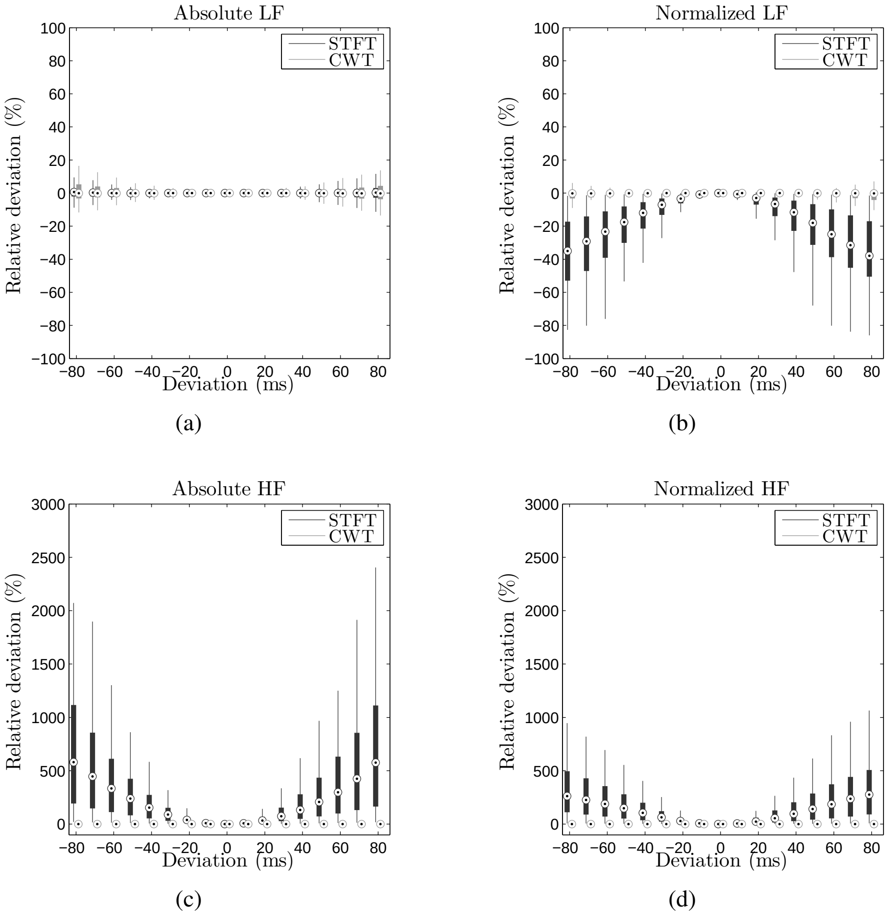

(a) (b)

(c) (d)

Figure 5.5 – *Deviation of the STFT and CWT spectral parameters for one mis-detection. The simulated deviation of the mis-detection from its original position is displayed on the x-axis.*

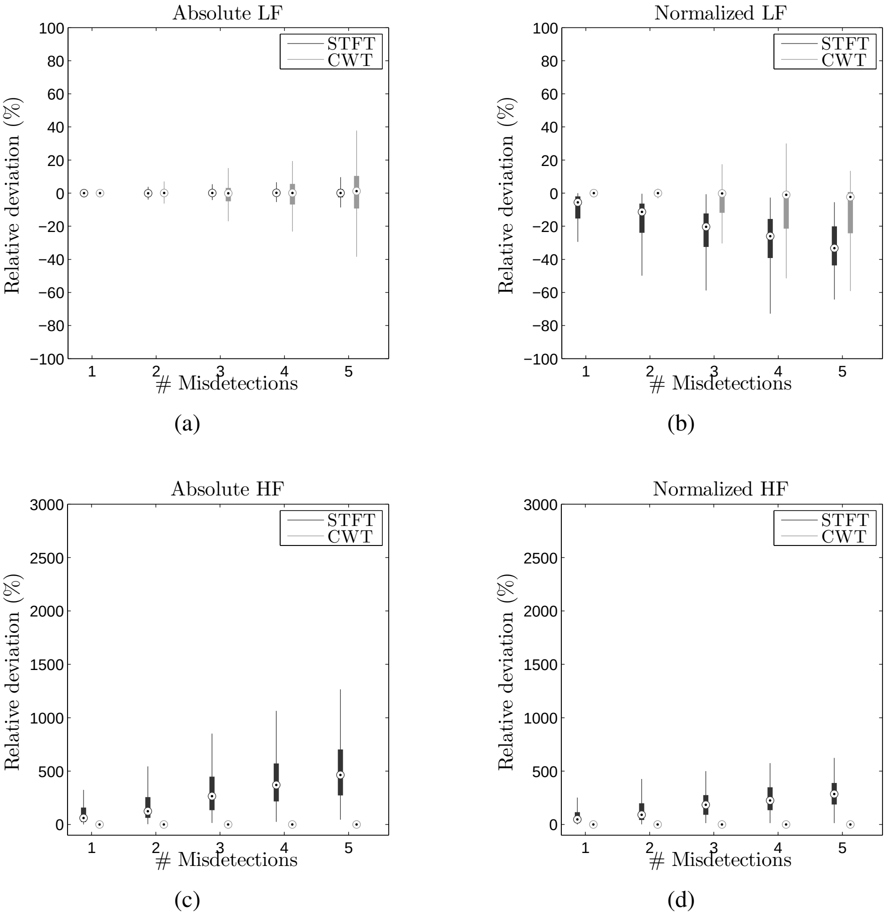

(a) (b)

(c) (d)

Figure 5.6 – *Deviation of the STFT and CWT spectral parameters for multiple mis-detections. The x-axis displays the number of mis-detections.*

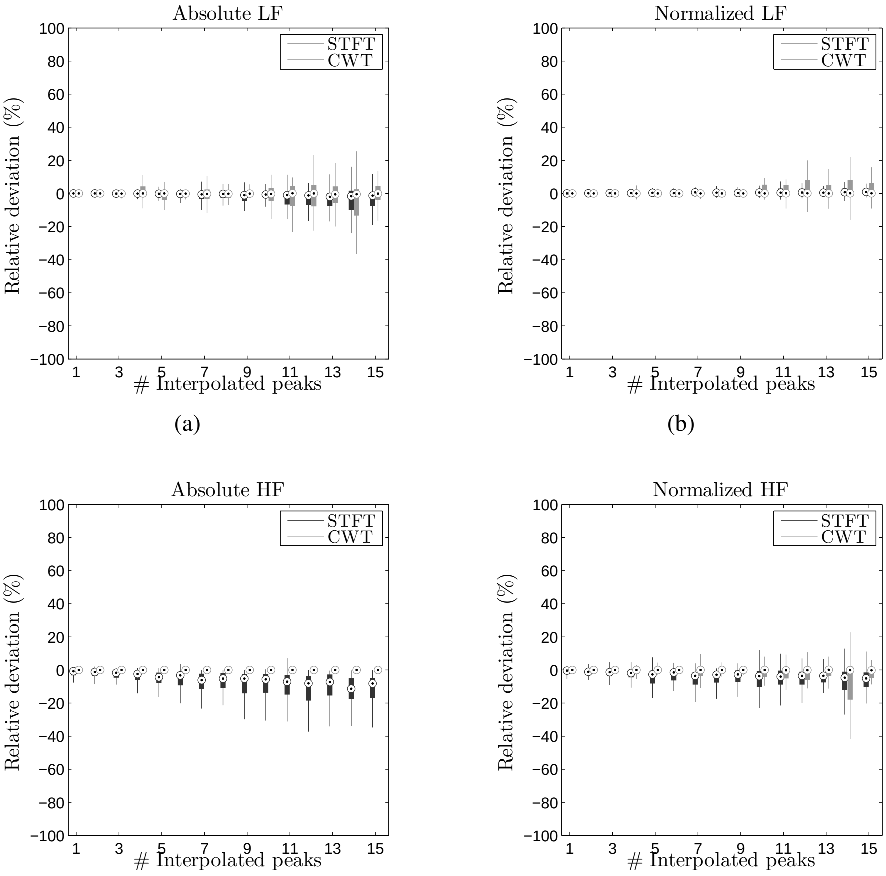

(a) (b)

(c) (d)

Figure 5.7 – *Deviation of the STFT and CWT spectral parameters for consecutively interpolated R-R intervals. The x-axis displays the number of consecutively interpolations.*

Chapter 6

Discussion

In this thesis, an algorithm is developed that enables reliable automated fECG extraction from abdominal recordings obtained throughout the pregnancy. For this purpose, the best performing techniques in the literature have been selected and optimized. Besides the use of the best performing techniques as a fundament for the developed fECG extraction algorithm, additional processing techniques have been developed to overcome the limitations of the existing techniques. Similar to the order used in chapter 5, this chapter first discusses the annotation, then the implementation and evaluation of developed algorithms, and finally the performance of STFT and CWT.

6.1 Annotation and inter-observer variability

In present research, annotation is used as the gold standard for the optimization and evaluation of algorithms that concern the detection of maternal or fetal ECG complexes. Although visual annotation is suited for this purpose since it allows to reevaluate and debate any found ECG complex, the annotation process is time consuming and subjective. Furthermore, in particular for the fECG, it is often difficult to visually distinguish the ECG complex from noise in a reliable manner. For these reason, an algorithmic approach seems more suited for standardized analysis of ECG databases. Annotation should be used to optimize and evaluate these algorithms.

Standardized annotated databases, such as the MITDB, can be used to some extend to objectively measure the performance of algorithms. Unfortunately such standardized databases are only available for the mECG and not for the fECG. Besides, these standardized databases are useful to evaluate the performance of an algorithm for the features of the mECG or the fECG (e.g. heart rate variations), however, they are not necessarily representative for the characteristics of the recordings themselves (e.g. quality of the recordings).

Unlike for the mECG, no standardized annotated database exists for fECG recordings throughout the pregnancy. Therefore, a randomized subset of the IHDB is generated for which the mECG is subtracted from the recordings with WAMES. Since the quality of the fECG and the fetal HRV have been reported to change throughout the pregnancy [**?**, **?**, 30–32, 50, 119], the randomized subset is generated such that fECG of the second and third trimester of the pregnancy is represented. To asses the inter-observer variability of the annotation of the subset of the IHDB, part of the subset is annotated by a second observer. The second observer is unfamiliar with the abdominal fECG recordings, however, is a specialist in neonatology.

The inter-observer agreement is established by means of the Cohen's Kappa test and a κ of 0.73 was found. In the literature this κ value is regarded as substantial [120] to good [121]. Whereas observer one had a one year experience with non-invasive fECG recordings as an engineer, observer two was an expert in neonatology. Note that the annotation is no performed by a gynaecologist, who might be more familiar with the fECG compared to a neonatologist. However, a gynaecologist is most presumably also unfamiliar with the non-invasive fECG recordings used in this thesis. Differences between observer 1 and 2 are mainly caused by the fact that observer 2 was unfamiliar with the quality of the fECG recordings and, hence, was more conservative in the identification of the fECG complexes. These differences, however, emphasize the need for an objective algorithmic approach over subjective annotation.

6.2 Peak detection: discussion

In the literature, numerous peak detection algorithm have been developed that perform reasonably well, among which [50, 51, 104, 122]. Of these, two promising detection algorithms have been evaluated in this thesis. The detection algorithm of Vullings et al. uses Bayesian probability theory to estimate an optimized threshold based on the statistical properties of the ECG recording and is used in both WAMES and PBSS. After the publication of WAMES and PBSS, a new detection technique has been developed by Rooijakkers et al., that has shown to outperform other peak detection algorithms [51]. In this thesis, however, it was found that the implementation of the peak detection algorithm of Vullings et al. in previous studies [48, 49, 51] deviated from its theoretical description and did not perform optimal. Furthermore, the evaluation of both peak detection algorithms for fetal R-peak detection in [51] is only performed on recordings at term, in contrast to the recordings in this thesis that are measured during the second and third trimester. For these reasons, both the improved peak detection algorithm of Vullings et al. and the peak detection algorithm of Rooijakkers et al. are reevaluated for maternal and fetal R-peak detection.

6.2.1 Peak detection: implementation and optimization

The literature values of the parameters for the transformation (SAD or wavelet-transformed) of the ECG (HP, LP, and M_{QRS} for the detection algorithm of Vullings et al., and Fc for the detection algorithm of Rooijakkers et al.) are mostly based on the common features of the mECG and the fECG. The literature values of the parameters for the dynamic behavior of the threshold (g, K^{min}, and K^{max} for the detection algorithm of Vullings et al., and α for the detection algorithm of Rooijakkers et al.) are experimentally determined and dependent on the used database. Since all parameters are expected to influence each other, in this thesis the optimal combination of settings is determined for the peak detection algorithm of the improved version of Vullings et al. and Rooijakkers et al. for the maternal and fetal R-peak detection.

Settings for the peak detection algorithms for fetal R-peak detection are determined base on all annotated files of subset of the IHDB and used for peak detection in all measurements of the IHDB, regardless of their GA. However, the quality of the fECG is expected to be dependent on the GA of the measurement. Early in the pregnancy the quality is reduced due to the small size of the fetal heart, whereas from 28-32 weeks of gestation the quality is reduced due to the presence of the vernix caseosa [44,45]. Therefore, future research should aim to obtain optimal settings for the peak detection algorithms that are specific for different GA.

Overall, the optimal settings found in this thesis for the maternal and fetal R-peak detection algorithms of Vullings et al., and Rooijakkers et al. are in good coherence with the literature values [50, 51], as shown in Table 5.2. The found value for the HP and LP in the peak detection algorithm of Vullings et al. and the Fc in the peak detection algorithm of Rooijakkkers et al. is supported by the frequency bands in which most spectral energy of the maternal and fetal QRS complex is contained (10-25Hz [101] and 20-60Hz range [94], respectively). The difference in the length of the integrating window in the length transformation for maternal and fetal R-peak detection is explained by the difference in the duration of the maternal and fetal QRS complex.

Besides the parameters concerning the transformation of the mECG and fECG, the optimal settings for the parameters of the dynamic behavior of the threshold constants g and α for maternal peak detection are also similar to the found literature values. For the fetal R-peak detection, however, the optimal setting for the g and α differs from their corresponding value found in the literature. These differences might be explained by the use of a different database. Whereas the database used in [51] only consisted of fECG recordings at term (all recordings around 40 weeks of gestation), the current studies used fECG recordings of the fetus during the entire second half of the pregnancy.

The increase in g of Eq. 3.14 results in an increase of the value of the instantaneous threshold ξ_i with respect to the noise value. Compared to the database used in [51], the R-peak amplitude is expected to be closer to the noise level in certain periods of the pregnancy than it is at term, e.g. due to the presence of the vernix caseosa which is mostly dissolved at term. Since the R-peak amplitude is less distinct from the noise amplitude, a higher value g is required for the fetal R-peak detection for recordings throughout the entire pregnancy.

The increase in α of Eq. 3.26 compared to the value found in the literature can also be explained as a result of a decreased quality of the fECG during the pregnancy. A larger value for α results in a smaller influence of a previously determined threshold value T_{prev} on a new threshold value T. In case the fECG is of less quality, it is more difficult to correctly estimate the electrical heart axis with PBSS or PBSSi. As a result, the appearance of the QRS complex, and thus the amplitude of the R-peak, in S_{PBSS} or S_{PBSSi} changes more frequently than for fetuses at term. Furthermore, less fetal movements are seen at term, leading to a more constant appearance of the QRS complex in S_{PBSS} and S_{PBSSi}. A combination of these effects might explain the higher value of α found in this thesis compared to the value found in [51].

For the implementation of the peak detection algorithm of Vullings et al. little influence is seen of changing the parameter of K^{min} on the D_e, both for the maternal R-peak detection in the MITDB and the fetal R-peak detection in the subset of the IHDB. The reason for the small influence of the value of K^{min} on the D_e is because differences due to changes in K^{min} only become effective after the infrequent event of a large artifact that disturbs the ECG recording. The value of K^{min} is, therefore, chosen based on the literature value and is set to 0.3, implying a value of 0.7 for K^{max}.

6.2.2 Peak detection: evaluation

If the original and the improved implementation of the peak detection algorithm of Vullings et al. are used for the MITDB, little difference is seen in the D_e. This is mainly because the influence of the improved implementation only establishes itself after the event of a large amplitude artifact has occurred, as explained in section 4.2.2. Since such a large artifact occurs infrequently in the MITDB, the improved implementation hardly influences the D_e. The true gain of the new implementation, however, can be seen from the reduced percentage of processing errors in WAMES. Solely by correct implementation of the detection algorithm, the number of processing errors has reduced by 22%.

The D_e found in this thesis for the MITDB with the original peak detection algorithms of Vullings et al. (0.66%) and the peak detection algorithm of Rooijakkers et al. (0.24%) are similar to the values found in Rooijakkers et al. (0.56% and 0.23%, respectively). Based on the results displayed in Table 5.3, Rooijakkers et al. showed the lowest D_e for the MITDB and the lowest number of processing errors for WAMES. Besides the better performance for the maternal R-peak detection for the MITDB and in WAMES for the IHDB, the main advantage of Rooijakkers et al. over Vullings et al. is that the peak detection algorithm of Rooijakkers et al. is specifically designed to have a low computational complexity [51]. Although computational complexity is not subject of this thesis, this does support the choice for Rooijakkers et al. for the maternal R-peak detection.

In contrast to recordings of the mECG, no standardized annotation database exists for fECG recordings to compare the performance of detection algorithm for fetal R-peak detection to literature values. The D_e found in [51] are based on a database of fECG recordings for which only (manually selected) files are included that contain a reliable fECG. Therefore, the D_e in Rooijakkers et al. should be compared to the D_e found in this thesis for reliable files.

The D_e values found in this thesis for reliable files for the peak detection algorithm of Vullings et al. (20.45%) and Rooijakkers et al. (15.89%), are slightly higher compared to the values found in [51] (19.23% and 9.42%, respectively). These differences, however, are presumably due to a different definition for reliable files. Despite the higher D_e for both detection algorithms, Rooijakkers et al. outperforms Vullings et al. for the IHDB and is, therefore, chosen for fetal R-peak detection.

6.3 QRS analysis: discussion

Peak detection algorithms developed in the literature mainly operate under the assumption that the fECG can be reliably detected at all times during a measurement. Although the fECG is always present in the recordings, the quality of the fECG differs over the course of the pregnancy and even throughout a measurement. The decrease in fECG quality in measurements early in the pregnancy is mainly caused by immaturity of the fetal heart, whereas the decrease in fECG quality later in the pregnancy is mainly due to the presence of the isolating layer of the vernix caseosa. Besides reduced fECG quality throughout the pregnancy, the fECG quality in S_{PBSS} might also differ throughout a measurement, e.g. due to incorrect estimation of the electrical heart axis in PBSS. Hence, even if part of the measurement has shown to contain a good quality fECG, there is no guarantee that the fECG remains detectable throughout the entire measurement.

The assumption current detection algorithms [50, 51, 104, 122] that the fECG is detectable at all times, results in numerous mis-detections in regions where the quality of the fECG is reduced. For this reason, the heart rates extracted from the IHDB with these detection algorithms all require a (subjective) manual selection of usable fetal heart rate segments [119, 123] (as seen in Fig. 3.6).

Another limitation of current peak detection algorithms arises from the fact that the fetal R-peak is of the same order of magnitude as the noise amplitude. As a result of the relatively low amplitude of the fetal R peak, it frequently occurs that the noise amplitude exceeds the fetal R-peak amplitude in the transformed fECG, even in case of a high fECG quality. Since in peak detection algorithms no extensive sanity check is performed on the identified QRS complexes, this inevitably leads to mis-detections that disturb extracted fetal heart rate signals that are potentially usable for the spectral analysis. Although these individual mis-detections do not disturb visual pattern recognition of the fetal heart rate, a substantial influence is seen on the spectral parameters of the fetal HRV (Fig. 5.5).

Finally, curent detection algorithms assume that the fetal R-peak always represents itself as the highest peak in the transformed fECG. However, since the fetal R-peak is often overshadowed by a noise peak in the vicinity of the actual R-peak, numerous R-peaks are missed.

To overcome the limitations of the current detection algorithms described above, a QRS analysis algorithm has been developed. First, this section discusses the choice for the parameters of the QRS analysis (C_{RR}, C_I, and C_E), after which the performance of the QRS analysis in addition to current peak detection algorithms is discussed.

6.3.1 QRS analysis: implementation

The values of C_{RR}, C_I, and C_E are estimated experimentally from the annotated subset of the IHDB. Since little is known about the exact value of these parameters and the value of C_I and C_E depends on the used Source-Separation technique, the found values cannot be related to literature values.

The choice of the value of C_{RR} is difficult. Namely, the value of C_{RR} is related to the width of the expectation region of consecutive QRS complexes (Eq. 4.4 and 4.5) and is, thus, directly related to the allowed beat-to-beat variation in the extracted fetal heart rate. Since the beat-to-beat variations influence the obtained spectral parameters (mainly HF), the choice of C_{RR} might cause a bias in the obtained spectral parameters. On the one hand, a small expectation region is desirable to minimize the probability of a mis-detection, on the other hand, a small expectation region could also result in a reduced variability of the extracted heart rates. Therefore, the limitation of the beat-to-beat variability is related to the SSQ (by means of the term β in Eq. 4.4 and 4.5). This ensures that, in general, larger fluctuations are allowed than have been found in the annotated files, except if the probability of a mis-detection is high. Note that the bias to obtain a low HRV in case of low SSQ is minimal, since the value of C_{RR} for low SSQ is based on the 5-95% interval. Therefore, 90% of the fluctuations found in the annotation can still be detected, even in case of low SSQ. Further research is required to examine the exact influence of C_{RR} on the obtained spectral parameters.

For the QRS complexes in PBSSi, it was found that the distribution of the absolute inproduct between the individual QRS complexes and an average QRS complex, differs substantially from the distribution in PBSS. The change in the distribution is explained from a more robust estimation of the electrical heart axis in PBSSi. The occurrence of incorrect estimations of the electrical heart axis in PBSS influences the appearance of the QRS complex in S_{PBSS} and results in a lower inproduct value of these QRS complexes with a running average QRS complex. Due to the more robust estimation of the electrical heart axis in PBSSi, these fluctuations in the QRS waveform that correspond to the lower inproduct values are seen less frequently.

Although the distribution of the ratio of the energy content of individual QRS complexes and a running average QRS complex is also related to the QRS waveform, this distribution remains unchanged after introduction of PBSSi. No difference, however, is expected in the energy content of the QRS complexes in S_{PBSSi} with respect to S_{PBSS}, since both are based on the same fundamental principles.

6.3.2 QRS analysis: evaluation

The additional value of the QRS analysis with respect to current peak detection algorithms is discussed in the light of the limitations that are described in the introduction of this section.

The inability of current R-peak detection algorithms to distinguish between high and low quality fECG becomes clear from the substantial increase in D_e for all files of the subset of the IHDB (54.62% and 57.44% for the peak detection algorithm of Vullings et al. and Rooijakkers et al., respectively), compared to the D_e for reliable files (20.45% and 15.89% for the peak detection algorithm of Vullings et al. and Rooijakkers et al., respectively). In contrast to this substantial increase, only a minor increase is seen in D_e if the QRS analysis is used (from 16.73% to 19.63%) compared to the substantial increase in D_e for Vullings et al. and Rooijakkers et al. (from 20.45% to 54.62% and from 15.89% to 57.44%, respectively). The relatively small increase in D_e found for QRS analysis shows the ability of the QRS complex to distinguish between high and low quality fECG.

The QRS analysis also enables to identify individual mis-detection in a high quality fECG. Since the number of the individual mis-detection relative to the total number of peaks is insignificant, this improvement is not reflected in a decrease in D_e. These small corrections, however, do ensure more usable fetal heart rate for spectral analysis.

Finally, the local search performed in the QRS analysis has resulted in a reduction of the number of missed peaks. This can be seen from the fact that the number of found P_{V_2} has increased. Since QRS analysis is performed in addition to the R-peak detection, any additionally identified QRS complex is due to the local search for missed peaks of the QRS analysis. Note that, as explained in section 4.3.2, all found P_{V_2} are identified as FP in the calculation for the D_e and an increase in found P_{V_2} results in a lower PPV, while this is actually an improvement. For this reason, the D_e for reliable files with QRS analysis is higher compared to the D_e without QRS analysis. If the number of found P_{V_2} is accounted for as True-Positive (TP), the D_e for reliable files is also lower with QRS analysis.

Despite a substantial improvement in D_e, the QRS analysis in combination with the peak detection algorithm of Rooijakkers et al. is limited for measurements below 20 weeks of gestation. In these measurements, the magnitude of the fetal R-peak is

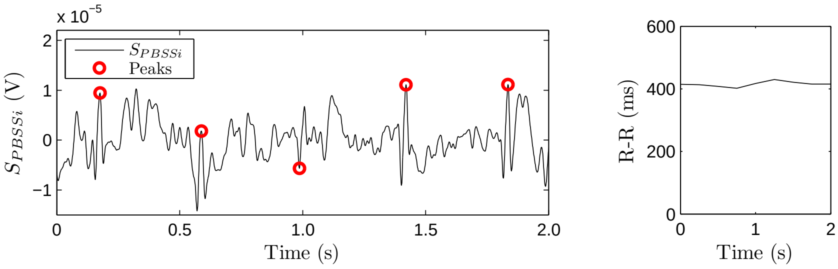

(a) (b)

Figure 6.1 – *(a) Example of a detected Q-peak in stead of the R-peak in a measurement below 20 weeks of gestation. (b) The influence of the mis-detected Q-peak on the R-R interval.*

often small and not always distinguishable from the Q-, or S-peak in the absolute wavelet transformed fECG which is used for the R-peak detection of Rooijakkers et al. If either the absolute value of the Q-, or the S-peak is larger than the R-peak, one of these peaks is identified instead of the R-peak, as is shown in Fig. 6.1a. These small mis-detections might cause disturbances in the estimation of a running average QRS complex and, as a result, reduce the value of the inproduct of any QRS complex with the running average QRS complex. Furthermore, a minor influence is also seen on the extracted heart rate (Fig. 6.1b) and the consecutively obtained spectral parameters as is seen in Fig. 5.6.

Since annotation of the QRS complexes this early in pregnancy was found difficult (seen in the relatively low number of annotated peaks in the group of 17-20+6 weeks of gestation in Fig. 5.1) and a peak is considered a TP if it is located within a 100ms interval around an annotated peak, these small mis-detections are not noted for the QRS analysis is compared to the annotation of the subset of the IHDB. Future research should aim to improve the QRS analysis algorithm such that it is robust against these mis-detections within a QRS complex. Besides improvements on the QRS analysis, this limitation emphasizes the need to obtain values for C_{RR}, C_I, and C_E that are specified for measurements of different gestational ages.

6.4 Source-Separation: discussion

In this thesis, a physiologically-based technique is chosen for the Source-Separation of the fECG recordings [49]. The PBSS technique has shown to outperform Blind-Source-Separation techniques [95,96], in particular for fECG recordings that exhibit a low SNR [49]. Despite a relatively good performance, the main limitation of the PBSS establishes itself in inaccuracies of the estimation of the electrical heart axis.

Since correct estimation of the electrical heart axis is directly related to the quality of the QRS complexes in the generated projection signal, improvements that are developed in this thesis mainly aim to provide a more robust estimation of the electrical heart axis. Improvements on the estimation of the electrical heart axis are governed by the use of previously identified QRS complexes for the computation of the VCG and by damping of the movement of the estimated electrical heart axis.

The advantage of the unrestricted orientation of the projection axis is that, in theory, for any orientation of the fetus the electrical heart axis can be estimated and, thus, the optimal SNR for the QRS complexes in S_{PBSS} can be obtained. However, the unrestricted orientation is also susceptible to artifacts. Therefore, the damping on the movement of the projection axis is introduced, which ensures that the projection axis only fully rotates towards a new orientation if that new orientation hold for a prolong period. Although the damping causes the estimation of the electrical heart axis to be more robust against artifacts, the damping also reduces the sensitivity to fetal movement. However, the damped movement of the projection axis is still able to follow the movement of the electrical heart axis to some extend and changes in the QRS waveform in S_{PBSS} are minimal. Therefore, the damping does not influence the performance of the algorithm is in the presence of fetal movement.

The performance of the original PBSS is compared to its improved version, PBSSi, by two quantitative measures. Firstly, the number of P_{V_2} that are not annotatable in S_{PBSS} but are visible in S_{PBSSi} and, secondly, the SNR of the annotated QRS complexes.

Although the increase in the number of P_{V_2} that are annotatable in S_{PBSSi} is a subjective measure and could also be ascribed to a learning rate of the observer, this provides an intuitive measure for the improved performance of the PBSSi. The SNR on the other hand, is less intuitive, however, it does provide a quantitative measure.

Based on the large percentage of P_{V_2} that has become annotatable in S_{PBSSi} (77%) and the substantial increase in the SNR of the QRS complexes in S_{PBSSi} compared to the median (range: 5-95%) of the SNR of the QRS complexes in S_{PBSS} (8.2 (range: -6.0-18.3) for PBSS and 12.3 (range: 3.6-20.6) for PBSSi), it is concluded that the estimation of the electrical heart axis has improved with PBSSi.

6.5 fECG extraction algorithm: discussion

The algorithm developed in this thesis that consists of peak detection, QRS analysis, and PBSSi, is meant to detect all peaks in the abdominal recordings, regardless whether peaks are annotated in S_{PBSSi} or V_2. Furthermore, the algorithm is designed such that it is able to distinguish between high and low quality fECG. Therefore, the performance of the developed algorithm is evaluated using all annotated peaks (both P_{Si} and $P_{V_{2i}}$) and all files. The performance is compared to the state-of-the-art techniques of PBSS in combination with Roojakkers et al.

From Table 5.7 it is becomes clear that the developed algorithm outperforms PBSS in combination with Rooijakkers et al., regardless whether only reliable files or all files of the annotated subset of the IHDB are used. The decrease in D_e for all files (17.92% for the developed algorithm and 51.56% for PBSS combined with Rooijakkers et al.) is more substantial compared to the decrease in D_e for reliable files (6.52% for the developed algorithm and 17.21% for PBSS combined with Rooijakkers et al.). Since the algorithm can also cope with a less reliable recording of the fECG, a clinical application, such as real-time monitoring of the fECG, becomes more reliable.

The increase in D_e of the developed algorithm if all files are used compared to the D_e if only reliable files are used (from 6.52 to 17.92%), is caused by an decrease in both *PPV* and *Se*.

The decrease of the *PPV* for all files compared to the *PPV* of reliable files (from 99.44% to 95.05%), is due to an increase in falsely identified peaks (nFP). The algorithms used in this thesis have, however, already shown to occasionally outperform the annotation in S_{PBSS} or S_{PBSSi}, as can seen by the percentage of found P_{V_2}. For this reason, in combination with the high *PPV* for reliable recordings (99.44%), the decrease in *PPV* for all files might be partially ascribed to limitations of manual annotation in the recordings with a low fECG quality. In future research, a more extensive annotation database should be obtained in which the annotation is performed by multiple gynaecologists.

The decreased *Se* (from 94.02% to 86.58%) is mainly the result of two recordings for which no peak is annotated in S_{PBSS}, although numerous peaks are found in V_2. One of these recordings is in the group of 17-20+6 weeks of gestation and the other in the group of 37-40+ weeks of gestation. The reason that peaks are only found in V_2 and not in S_{PBSS} in these two recordings, is that a good quality of the fECG was only present in two out of the eight leads.

Depending on period in the pregnancy, there might be two explanations for this distribution of the quality of the fECG. In the period from 17-20+6 weeks of gestation it could occur that the fetus is located more closely to part of the electrodes, due to the small size of the fetus. This, in combination with the relatively weak fECG for these immature fetuses, could result in a high quality fECG in only part of the electrodes. In the period from 37-40+ weeks of gestation, the fECG is mostly visible through cracks arising in the vernix caseosa which could also explain the spatial differences in the fECG quality.

Since both PBSS and PBSSi assume an equal quality fECG distribution, all lead signals are used to generate the VCG. If the majority of the leads, however, only contribute noise to the VCG, the estimation of the electrical heart axis is severely disturbed.

As a solution to the limited *Se* of the developed algorithm for recordings with a high quality fECG in only part of the leads, a selection of the leads could be used for the estimation of the electrical heart axis. A techniques that allows for selection of leads is described in [124]. This method ranks the leads based on the contribution of the fECG in each lead to the combined VCG. Further research is required to implement this technique in a reliable manner.

If for these two recordings the leads that contain a good quality fECG are manually selected, the overall *Se* increases to 93.80%, which is similar to the *Se* for reliable files.

6.6 Performance of STFT and CWT

The results of the effect of simulated mis-detection on the outcome of the spectral parameters of the STFT and the CWT clearly advertise the use of CWT over STFT. The absolute LF and HF, and the normalized LF and HF are hardly influenced for CWT. In contrast, for STFT a large effect is already seen after a small mis-detection on the obtained absolute HF, normalized LF and normalized HF.

The difference in the effect on the HF power of STFT and CWT can be understood from the use of different base functions (sinuses for STFT and wavelets for CWT). For CWT, the HF component of the heart rate is analyzed with daughter wavelets that exhibit a high time resolution. As a result, a mis-detection only has a brief effect in time on the HF power and little influence is seen on the HF power of an entire 64 seconds. In contrast to the high time resolution of the CWT for the HF, the time resolution of the sinuses in the STFT is limited by the window length used by the STFT. Since the minimum window length of the STFT is determined by two times the wavelength of the lowest frequency of interest (0.04Hz), the minimum window length for the STFT is 64 seconds. Hence, a mis-detection influences the obtained HF power by STFT of the entire 64 seconds.

The number of consecutive interpolated peaks only appears to have a minor influence on the spectral parameters of both STFT and CWT. This can be understood from the fact that the interpolations mainly influences the LF. The LF is, per definition, mostly determined by slow changes in the heart rate and an effect is, thus, only seen on the LF power after numerous consecutive interpolations.

To ensure reliable results for the spectral parameters of the fetal HRV, CWT is chosen as the method for spectral analysis. Heart rate signals are included with a minimum length of 64 seconds, maximally 20% interpolated R-R intervals [100], and maximally 9 consecutively interpolation peaks.

6.7 conclusion

The developed algorithm has shown to outperform state-of-the-art techniques for reliable extraction of the fECG. Furthermore, the developed algorithm allows for automated fECG extraction, without the need for consecutive manual selection of usable fetal heart rate. Based on the comparison between the STFT and the CWT, CWT is chosen for the analysis of the fetal HRV. In the next chapter, the developed algorithm is used in combination with CWT to obtain spectral parameters of the fetal HRV from a longitudinal follow-up study.

Chapter 7

Clinical study

Using a previous implementation, we performed a clinical study as presented in Appendix C and the results are submitted for publication in The Journal Of Physiology. The percentage of usable fetal heart rate in this study is still limited. Following the optimization explained in this thesis, the study was repeated and the results are displayed in this chapter.

7.1 Introduction

One of the great challenges for obstetrician units these days is timely recognize fetal distress throughout the pregnancy and during labor. At present, CTG is used as the worldwide standard for fetal monitoring during labor. However, due to its poor specificity [7], the introduction of the CTG in the clinic has lead to an increased rate of unnecessary operative interventions, without a noticeable improvement on the fetal outcome [7]. As additional diagnostic tests to provide information in case of abnormalities in the CTG, FBS and STAN [9] have been introduced. Unfortunately, these additional techniques have only been reported to provide limited support [7, 11, 17, 18, 88]. Furthermore, these techniques are invasive and can only be used during labor.

Besides FBS and STAN, valuable information might be obtained from the fetal HRV [20–23]. Since cardiac regulation is controlled by the sympathetic and parasympathetic nervous system, fetal HRV might indirectly reflect fetal wellbeing [21]. To objectively quantify changes in the fetal HRV, spectral analysis can be used. Recent studies have already shown that spectral parameters of the HRV might be indicative for fetal distress in an early stage of labor [28, 29]. In order to use spectral analysis of the fetal HRV as a diagnostic test, more insight is required in the development of the spectral parameters throughout the pregnancy [34].

In the literature, limited research has been done on the spectral parameters of the fetal HRV during the second and third trimester of the pregnancy [30–32, 119, 123]. In these studies an increase is seen in the overall frequency power of the fetal HRV with proceeding pregnancy, which is thought to be a result of maturation of the fetal autonomic nervous system (ANS) [30,31]. However, the studies are in disagreement concerning changes in the spectral parameters of the HRV.

Of these studies, the study of Karin et al. [32] and David et al. [31] are limited regarding the developmental aspect, since no follow up study is performed. In these studies only two [32] and three [31] measurement points are obtained throughout the pregnancy, of which non before 22 weeks of gestation.

In contrast to [31,32], the studies Peters et al. [119], Van Laar et al. [123], and Van Leeuwen et al. [30] do examine the spectral parameters of the fetal HRV through the entire second and third trimester of the pregnancy.

In Van Leeuwen et al. [30], magnetocardiography (MCG) is used to examine fetal HRV throughout the second and third trimester of the pregnancy. To obtain spectral parameters of the fetal HRV, Van Leeuwen et al. uses 5 minutes recordings and Fourier-Transformation. Although the use of 5 minutes segments does not necessarily imply a limitation, Van Leeuwen et al. did not distinguish between fetal behavioral states. Since fetal behavioral states are associated with the spectral parameters of the fetal HRV [31,34], the spectral parameters obtained in a 5 minute segment might not be representative for the fetal condition. Furthermore, the adult HF frequency band (0.2-0.4Hz) is used for the HF frequency band for the fetal HRV, which is based on breathing movements. Since adult breathing movements are unrelated to fetal breathing movement, this choice for the HF frequency band seem inappropriate [31]. In accordance with [31], this thesis uses a HF frequency band of 0.4-1.5Hz.

In the previous studies performed by our group of Peters et al. [119] and Van Laar et al. [123], the same database of abdominal ECG recordings is used, that is used in this thesis (described in section 4.1). However, due to the use of less optimal fECG extraction algorithms at that time, usable fetal heart rate for spectral analysis is only extracted in 15.79% [119] and 19.74% [123] of the measurements of the IHDB. In these studies, the found trends observed for the obtained spectral parameters are in accordance with those seen in animal studies and previous literature. Despite these promising results, mostly statistically insignificant trends are observed and both studies concluded that this is probably due to insufficient extracted usable fetal heart rate [119,123].

The final goal of this study is to obtain spectral parameters of the fetal HRV in the large follow-up study to investigate maturation effects of the ANS on the fetal HRV.

7.2 Materials and Methods

The inclusion criteria for patients in this longitudinal study of the IHDB have been described previously in [123] and briefly discussed in section 4.1. In chapter 4, the new algorithm for fECG extraction that is used in this clinical study is extensively discussed and is represented by the flowchart in Fig. 4.3.

Prior to the spectral analysis, extracted heart rate signals are resampled to obtain an equidistant set of data points by the process explained in section 3.4. The CWT is used for the spectral analysis, since it has shown to be more reliable compared to STFT 5.6. Spectral parameters are obtained from fetal heart rate signals that have a minimum length of 64 seconds, maximally 20% interpolated R-R intervals [100], and maximally 9 consecutively interpolation peaks. The choice for these criteria is based on the analysis presented in section 5.6 and allows for reliable spectral analysis in short heart rate segments.

If a measurement contains multiple usable heart rate segments that meet the above criteria, the spectral parameters of that measurement are represented by their median values of all usable heart rate segments. To calculate the median values of the spectral parameters of a measurement, the heart rate segments within the measurement are accounted for weighted by the length of the segment.

Trends of the spectral parameters throughout the pregnancy, the measurements of the IHDB are divided into groups according to the weeks of gestation:

- group 1: ≤17+0
- group 2: 17+0 - 19+6
- group 3: 20+0 - 22+6
- group 4: 23+0 - 25+6
- group 5: 26+0 - 28+6
- group 6: 29+0 - 31+6
- group 7: 32+0 - 34+6
- group 8: 35+0 - 37+6
- group 9: 38+0 - 40+

Note that the length of the usable fetal heart rate extracted from a measurement might differ between measurements. Despite these differences in length of the usable fetal heart rate in each measurement, all measurements contribute equally for the calculation of median values in each gestational age group.

In this study, we focus on a first presentation of observed trends and no statistical tests is used to support obtained results. In order to estimate whether observed trends are patient independent, two randomized subset of the entire IHDB are generated and spectral parameters of the two randomized subgroups are compared to the trends observed in the entire IHDB.

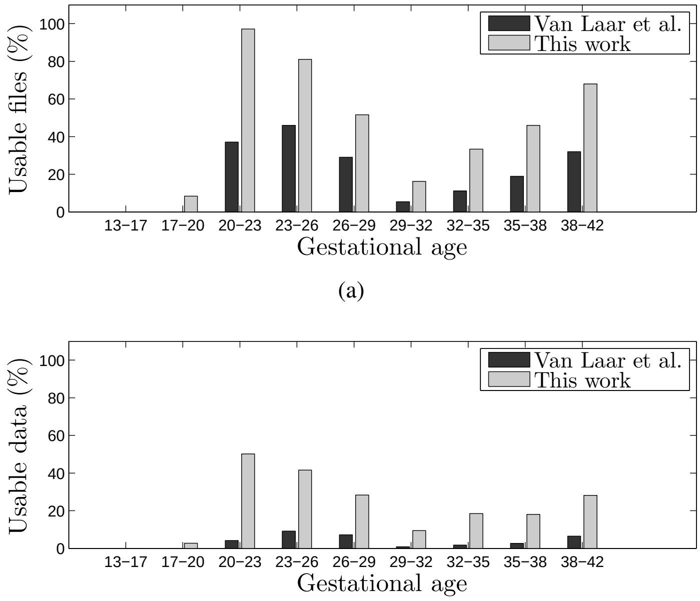

(a)

(b)

Figure 7.1 – *Results are shown for the previous study of Van Laar et al. [123] (dark gray) and the current work (gray). (a) Percentage of files that contain at least 64 seconds of usable fetal heart rate signal. (b) Percentage of usable measurement time.*

7.3 Results

Of the 304 measurements of the IHDB, in 135 (44.41%) measurements fetal heart rate could be extracted that meets the criteria described in the section 7.2. Of the total measurement time of 236 hours, in 53.4 (22.63%) hours usable heart rate signal was obtained. An overview of the percentage of usable heart rate distributed over the pregnancy for the previous study of Van Laar et al. [123] and the current work, is shown in Fig. 7.1. The median(25%-75%) of the length of the usable heart rate signals for all measurement is 24(12-35) minutes and only two measurements are included with less than 3 minutes of usable heart rate signal.

The results for the absolute LF and HF, and the normalized LF and HF for the two randomized subsets of the IHDB are used are shown in Fig. 7.2. The results for the entire IHDB are displayed in Fig. 7.3. Only results are shown for groups that contain three or more patients with usable fetal heart rate.

The absolute HF of the group 17-19+6 weeks of gestation appears to be larger compared to the absolute HF in later periods of the pregnancy. This increased absolute HF is caused by an increase in mis-detections within a QRS complex for young fetuses, as is described in section 6.3.2 and displayed in Fig. 7.4. These small mis-detection cause for corruption in the heart rate signals and result in an increased

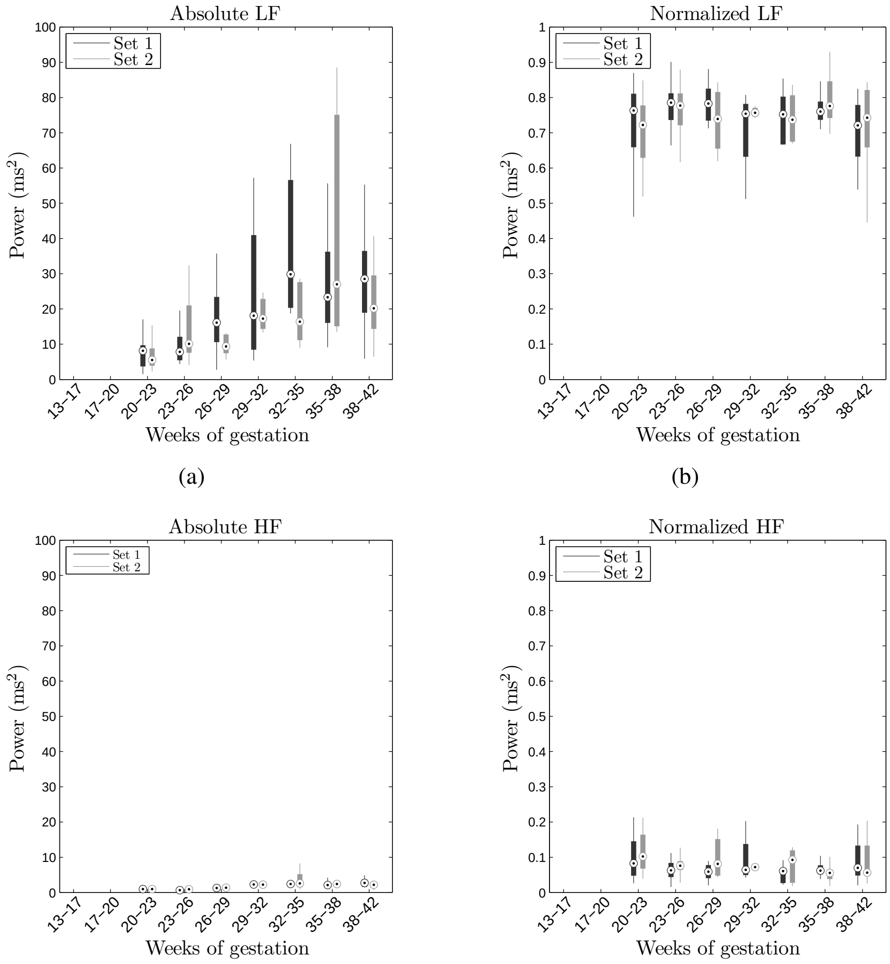

(a) (b)

(c) (d)

Figure 7.2 – *Trends of the spectral parameters throughout the pregnancy for the two randomized subsets of the IHDB.*

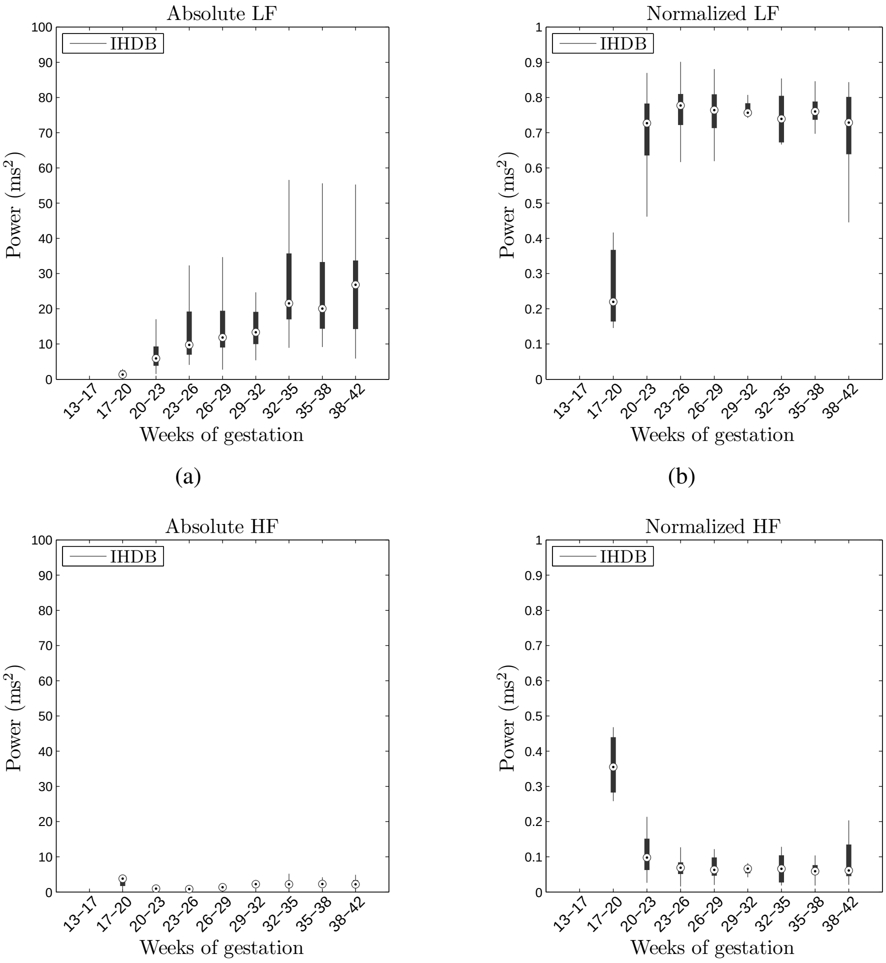

(a) (b)

(c) (d)

Figure 7.3 – *Trend of the spectral parameters throughout the pregnancy of the entire IHDB.*

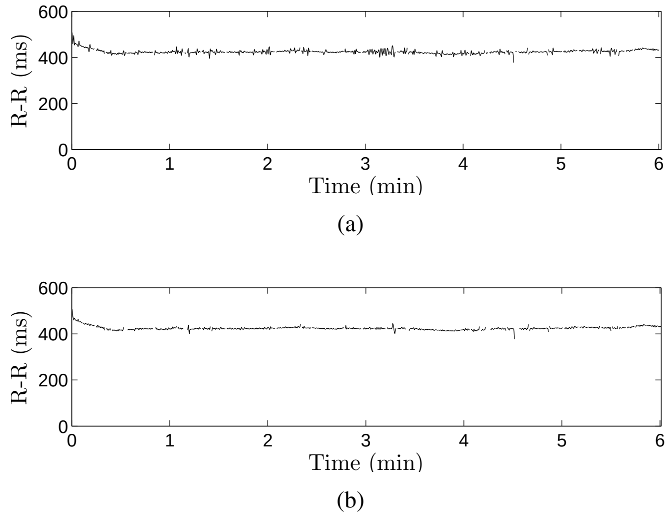

(a)

(b)

Figure 7.4 – *(a) Original heart rate signal of a fetus of 17+6 (absolute HF 3.3). (b) The same heart rate signal, corrected for mis-detected Q-, and S-peaks instead of R-peaks (absolute HF 1.4).*

absolute HF.

An example of this effect on the extracted heart rate of a fetus of 17+4 weeks of gestation is shown in Fig. 7.4. By visually correcting these corruption, the median absolute HF of the group 17-19+6 weeks of gestation decreases from 3.8 to 2.7, which value is similar compared to the median absolute HF of the other groups. The corrected results for the absolute LF and HF, and the normalized LF and HF are not displayed.

Since in measurements below 20 weeks of gestation usable fetal heart rate is only extracted in three measurements, additional heart rates are extracted from other measurements prior 20 weeks of gestation. In total, four extra annotated measurements are included. The results for the absolute LF and HF, and the normalized LF and HF including these additionally annotated measurements are displayed in Fig. 7.5. Note that, to obtain multiple data points in the region below 20 weeks of gestation, the groups of 13-16+6 and 17-19+6 weeks of gestation are split into 13-15+6, 16-17+6, and 18-19+6 weeks of gestation. Despite the additional annotation measurements, no measurements are obtained in the group of 13-16+6 weeks of gestation. Furthermore, only two measurement are obtained in the group of 16-17+6 weeks of gestation. These measurements are displayed as red markers in the graphs.

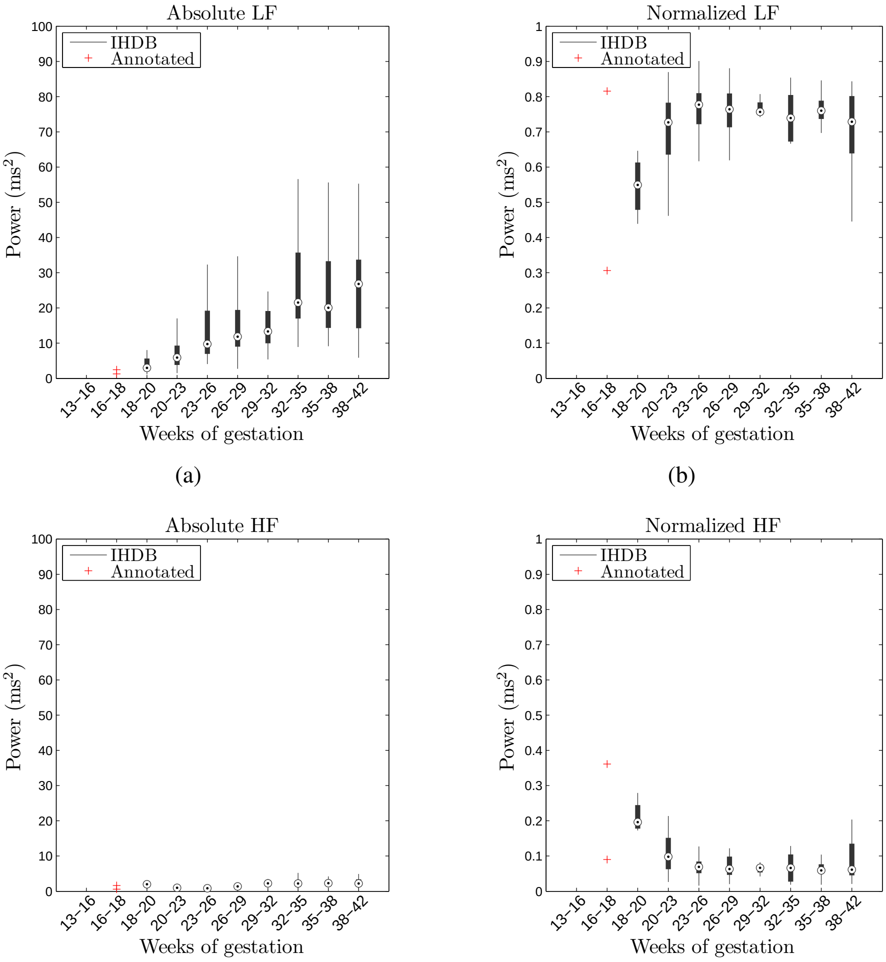

(a) (b)

(c) (d)

Figure 7.5 – *In addition to the usable heart rate segments found by the developed algorithm, the heart rate signals of four extra annotated measurements of below 20 weeks of gestation are included. The groups of 13-17 and 17-20 weeks of gestation are split into 13-16, 16-18, and 18-20 weeks of gestation. Since in group 16-18 weeks only two measurements are obtained, these are displayed as red markers.*

7.4 Discussion

In this thesis spectral parameters are obtained of the fetal HRV throughout the pregnancy. For this purpose, a longitudinal follow up study consisting of non-invasive fECG measurements is performed throughout the second and third trimester of the pregnancy. In this thesis a new algorithm is designed that enables reliable automated extraction of the fetal heart rate heart rate from the abdominal fECG recordings.

First, the percentage of extracted fetal heart rate by the developed algorithm is discussed. Then, the results of the obtained spectral parameters are discussed separately for the very preterm period (16-32 weeks of gestation) and the near term (32-40+ weeks of gestation), similarly to [123].

7.4.1 Usable extracted fetal heart rate

The previous studies of our group of Peters et al. [119] and Van Laar et al. [123] are used as reference framework, since the same database is used in these studies. Although both Peters et al. and Van Laar et al. require a minimum length of 64 seconds for the heart rate signal, Van Laar et al. uses STFT for the spectral analysis in contrast to the CWT that used in Peters et al. and the present work. Consequently, only 5% interpolation is allowed for heart rate segments in Van Laar et al. in contrast to the 20% interpolated allowed in Peters et al. and the present work. The use of STFT, however, is seen as a limitation of the study and Van Laar et al. is thus also used as a reference study.

In both the study of Peters et al. and Van Laar et al. usable fetal heart rate needed to be selected manually and usable heart rate is extracted in 15.8% and 19.7% of all measurements, respectively. Of the total measurement time of the IHDB (236 hours), Peters et al. subtracted fetal heart rate in 8.56% and Van Laar et al. in only 3.7%. Despite the higher percentage of measurements in which reliable heart rate was extracted by Van Laar et al., the percentage of the length of extracted fetal heart rate compared to the total measurement time is less compared to Peters et al. This reduction is mainly due to the strict criteria associated with the STFT in Van Laar et al..

In contrast to the low percentage of usable fetal heart rate obtained in the studies of Peters et al. and Van Laar et al., the algorithm developed in this thesis extracted fetal heart rate in 44.4% of all measurements and 22.6% of the total measurement time is usable for the spectral analysis. Besides the substantial increase in extracted fetal heart rate for the spectral analysis, the developed algorithm does not require manual selection of usable heart rate segments.

Despite the increase in usable extracted heart rate, no usable fetal heart rate is extracted for measurements prior to 16 weeks of gestation. This result is in line with the results of literature studies of Van Leeuwen et al. [30], that also was unable to extract reliable heart rate in these recordings despite the use of fMCG.

A low percentage of usable fetal heart rate is also seen for measurements from 16 to 19+6 weeks of gestation. Although fetal heart rates that are extracted by the algorithm developed in this thesis are less contaminated by residual mis-detections due to the constrains imposed by the QRS analysis, these constrains result in a low percentage of usable fetal heart rate for measurements from 16 to 20 weeks of gestation.

After 20-22+6 week of gestation, a gradual decrease is seen in the percentage of usable fetal heart rate, due to reduced quality of the fECG probably as a result of the appearance of the isolation layer of the vernix caseosa. After 32 weeks of gestation, a gradual increase is seen in the percentage of usable fetal heart rate which is could be related to the appearance of cracks in the vernix caseosa [67, 71].

Improvement to the QRS analysis and PBSSi that are suggested in section 6.3.2 and 6.5 might result in an increased percentage of usable fetal heart rate in the periods periods with a low quality fECG, however, further research is required to maintain reliability for the extracted heart rates.

7.4.2 Spectral analysis of the fetal HRV

In general, the absolute LF power displays a graduate increase in the median value and the spread for proceeding GA. The absolute HF is small, regardless of the GA and no trend is seen. The normalized LF is large compared to the normalized HF for all GA except for measurements below 20 weeks of gestation, and no trend is seen in normalized LF and HF.

Based on the similar trends observed in both subgroups for all spectral powers, it is assumed that the observed trends for the entire IHDB are patient independent. Results of the observed trends in the spectral parameters are further discussed based on Fig. 7.5.

Very preterm period (16 to 32 weeks of gestation)

For the very preterm period an increasing trend is seen in absolute LF with progressing pregnancy. No trend is observed in absolute HF. We hypothesise that the increase in absolute HF increase is mainly due to an increased in sympathetic modulation of the fetal heart as a result from maturation of the fetal autonomic nervous system. As explained in section 2.6.1, the PSNS is able to afflict both rapid and graduate changes on the heart rate, whereas the SNS is only able to afflict graduate changes. Therefore, activation of the PSNS is associated with both LF and HF power and activation of the SNS only with LF power [25, 80]. Since an increasing trend is mainly observed in the LF power and not in the absolute HF power, the increase is absolute LF can thus be associated with an increased activation of the SNS.

It is unlikely that the observed increase in absolute LF prior to 32 weeks of gestation is caused by changes in the behavioral states of the fetus. In the period from 24 to 28 weeks of gestation, a healthy fetus on average makes 150-200 movements per hour [87] and no behavioral states are observed prior to 30 weeks of gestation [89]. Therefore, it can be assumed that most extracted fetal heart rate in measurements prior to 32 weeks of gestation are measured during fetal activity.

Except for the measurements prior to 20 weeks of gestation, the absolute LF power is large compared to the absolute HF power. This is reflected in the relatively large value of the normalized LF power compared to the normalized HF power, and might be due to a relatively dominant SNS in premature fetuses which is in accordance with animal studies [84, 85].

For measurement prior to 20 weeks of gestation the absolute LF power is of the same order of magnitude as the absolute HF power. As a result a substantially lower normalized LF power is seen in the group of 18-19+6 weeks of gestation compared to later in the pregnancy. Furthermore, the large difference that is seen for the normalized LF power of the two measurements in the group of 16-17+6 weeks of gestation is also explained from the fact that the absolute LF and HF power are both of the same order of magnitude. This early in the pregnancy, both absolute LF and absolute HF are practically zero. As a result, the normalized LF and normalized HF can have any value between zero and one, depending on which of the two happens to be larger. The low values of the absolute LF and HF might be due to a low regulation of the fetal ANS. Further research is required to obtain more spectral measurements this early in the pregnancy.

The (near) term period (32 to 40+ weeks of gestation)

For the (near) term fetuses no increasing trend is observed in absolute LF and absolute HF power. However, the median value and the spread in absolute LF power have increased considerably compared to the median value and the spread in absolute LF power for the very preterm period.

After 34 weeks of gestation, fetal behavioral states are fully developed [87]. In the near term period, a fetus is mostly either in active and quiet sleep (approximately in 90% of the behavior of term fetuses [91]). Since these behavioral states are partially defined based on HRV, large differences could be seen between the spectral parameters during active an quiet sleep. The hypothesis that the large spread in absolute HF is due to the appearance of behavioral states in the third trimester of the pregnancy is further by the high absolute LF power during active sleep compared to quiet sleep found by Van Laar et al. [123].

An illustrative example of the difference in heart rate pattern for active and quiet sleep is shown in Fig. 7.6. The absolute LF values corresponding to the heart rate during active sleep and quiet sleep was 77.2 and 17.0, respectively. This large spread

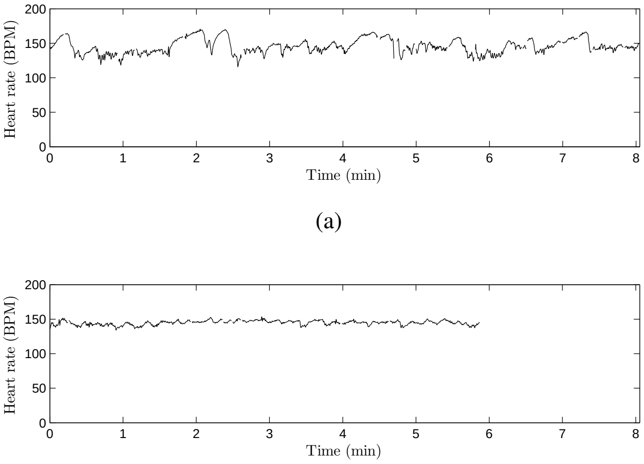

(a)

(b)

Figure 7.6 – *Two extracted fetal heart rate segments from one measurement at 36+0 weeks of gestation. The heart rate patterns are identified by a gynaecologist as (a) during active sleep and (b) during quiet sleep. The corresponding values for the absolute LF for the active and quiet sleep are 77.2 and 17.0 ms*^{2}*, respectively.*

in absolute LF within a measurement emphasizes the need to distinguish between different behavioral states. Note that, because of the large differences that are observed for the spectral parameters during active and quiet sleep, there is no use to examine trends in the spectral parameters within each patient.

In order to explain trends observed in the near term period and trends within each patient, future research should aim to relate fetal behavioral states to the obtained spectral parameters. After behavioral states have been identified, observed changes might be correlated to literature studies on invasive measurements during labour at term.

7.5 conclusion

The algorithm developed in this thesis enables reliable automated extraction of the fECG in non-invasive fECG recordings during the very preterm and term period. Improvements of signal processing might result in a larger percentage of extracted fetal heart rate for recordings with a low quality fECG. The observed changes of the spectral parameters of the fetal HRV are in accordance with those seen in animal studies. However, in order to explain trends observed in the near term period, future research should aim to relate fetal behavioral state to the obtained spectral parameters.

Chapter 8

Conclusions

In this thesis, a new algorithm is developed that allows for reliable extraction of the fetal heart rate from non-invasive fECG recordings. At present, no algorithm exists that enables reliable extraction of the fECG from abdominal recordings, despite the numerous improvements of previous studies by implementation of new signal processing techniques. For this purpose, the best performing state-of-the-art signal processing techniques have been selected and optimized. In addition, to overcome the limitations of these techniques, additional processing techniques have been implemented.

Processing errors occurring in the mECG subtraction of WAMES are resolved by implementation of improved peak detection algorithms. In order to provide a robust Source-Separation technique (based on PBSS) to enhance SNR for the fECG, an improved version of the PBSS is implemented. To increase the sensitivity and positive-predictive-value of the current peak detection algorithms, an automated QRS analysis is introduced. Finally, the performance of techniques for spectral analysis (STFT and CWT) is investigated for simulated mis-detections and consecutively interpolated R-R intervals. Based on the performance, criteria for fetal heart rate signals are determined that enable reliable spectral analysis.

The developed algorithm has shown to outperform state-of-the-art techniques for the extraction of the fetal heart rate from non-invasive recordings. The improved algorithm enables reliable automated extraction of the fetal heart rate and is used in a large longitudinal follow up study to obtain spectral parameters of the fetal HRV throughout the second and third trimester of the pregnancy. Due to the improvements of signal processing, sufficient fetal heart rate is extracted from the database and clear trends can be observed in the spectral parameters. The observed changes in the spectral parameters are in accordance with those seen in animal studies.

Chapter 9

Future directions

Timely recognition of fetal distress during labor is challenging. At present, cardiotocography (CTG) is used as the worldwide standard for fetal monitoring during labor. In case of abnormalities in the CTG, fetal scalp blood sampling (FBS) and analysis of the ST-segment (STAN) are used to provide additional information. Unfortunately, these techniques have only been reported to provide limited support.

Besides FBS and STAN, additional information about fetal well-being might also be provided by fetal cardiac activity. The mean interest in this thesis has been to reliably obtain spectral parameters of fetal heart rate variability (HRV). Recent studies have already shown that spectral parameters might be indicative for fetal distress in an early stage of labor [28, 29]. Besides the spectral parameters of the fetal HRV, morphological changes in the fECG waveform might also provide information [50]. Finally, real time tracking of the fECG could provide obstetricians with up to date information about fetal well being. Before any of these applications can be used as a diagnostic tool, further research is required regarding signal processing and clinical implications.

9.1 Technological assessment and recommendations

The most important recommendations regarding signal processing steps are discussed in this section. The performance of the algorithm has to be optimized for recordings that contain a low quality fECG in order to extract a larger percentage of usable fetal heart rate.

- Settings that are used in the developed algorithm for the peak detection and the QRS analysis currently are unrelated to different periods in the pregnancy. Future research should aim to optimize the settings for the peak detection and the QRS analysis based on the period in the pregnancy. This might result in an increase in usable fetal heart rate in periods where the quality of the fECG is reduced (prior to 20 weeks of gestation and from 28-32 weeks of gestation).

- The used Source-Separation technique assumes an equal fECG distribution over all leads, resulting in a reduced performance for recordings in which the fECG is not equally distributed. A solution to this problem could be obtained by implementation of a channel selection algorithm, such as the selection algorithm proposed in [124].

- The peak detection algorithm used in this thesis currently does not perform optimal in combination with the QRS analysis in measurements where the fetal R-peak is difficult to distinguish from the fetal Q-, or S-peak in S_{PBSS}. Implementation of a local search for the true R-peak could provide a solution.

- The algorithm is implemented in an iterative manner, mainly to enable accurate estimation of the electrical heart axis. This iterative implementation, however, also enables semi-online extraction of the fECG. In the current implementation, a buffer signal of 30 seconds is analysed during each iteration and the buffer is updated by a 2 second update rate. The buffer length and the update rate are chosen such as to match the buffer length and the update rate used for the mECG extraction of WAMES. As a consequence, the developed algorithm can be directly implemented in addition to WAMES. Since the developed algorithm is able to distinguish reliable and unreliable fECG, the extracted fECG could be clinically used. To enable real-time processing, future research should aim to decrease the computational complexity and fully implement the fECG extraction algorithm in an online manner.

- Besides real-time monitoring of the fECG, the QRS analysis enables detection of arrhythmias in the fetal heart rate. This feature of the QRS analysis is already shown in the intermezzo at the end of chapter 4, although the discussed arrhythmias are not related to pathological conditions. Future research should aim to define exact conditions for the detection of arrhythmias and examine whether certain arrhythmias might have diagnostic value.

9.2 Recommendations for clinical assessment

The main focus of this thesis has been to reliably extract fetal heart rate from non-invasive recordings and to gain more insight in the change of the spectral parameters throughout the pregnancy for normal fetuses. The results represented in the clinical study in chapter 7 are only meant as a first presentation of observed trends for the spectral parameters. For clinical diagnostic value, several aspect should be further investigated. Besides the spectral parameters of the fetal HRV, future research could also focus on evaluation of other possibly diagnostic information that is present in the fECG.

- The length of the extracted fetal heart rate differs per measurement. In the study presented in chapter 7, these differences are not accounted for to present the trends in the spectral parameters. In order to obtain statistical values for the observed trends, differences in the length of the extracted heart rate should be accounted for. Furthermore, observed trends should be supported by statistical evaluation.

- To explain observed trends in the near term period, fetal behavioral states should be related to the obtained spectral parameters. Ultra-Sound (US) measurements that have been acquired simultaneously with the non-invasive recordings can be used to identify and relate fetal behavioral states to the obtained spectral parameters. This is already done in our previous study [123] and should also be performed for the results in chapter 7.

- An interesting aspect of the acquired IHDB is the longitudinal follow up for all patients. In previous studies of our group [119, 123], the low percentage of measurements that contained usable fetal heart rate (15.79% and 19.74%, respectively) did not allow to examine the fetal ANS development of individual patients. With the developed algorithm in this thesis, fetal heart rate is extracted in a larger percentage of the measurements (44.41%), which should be suitable for a longitudinal study. For this purpose, the identification of fetal behavioral states is required, since different fetal behavioral states cause a spread within a measurement that is equal to the spread found in the entire IHDB.

- The main focus on the clinical aspect of this thesis has been to obtain spectral parameters of the fetal HRV for healthy fetuses. In addition to the spectral parameters of the fetal HRV, one should also assess the spectral parameter in growth restricted fetuses.

- The information that is contained within the non-invasive fECG recordings is not limited to the fetal HRV. From the non-invasive recordings it is also possible to obtain morphological information of the fECG. In clinical practice, STAN already analyses changes in the ST-segment of the fECG during labor. The STAN, however, invasively records the fECG by an electrode attached to the fetal scalp and can only be used during labor. In contrast, the non-invasive fECG can be used throughout the entire pregnancy. Further research is required to examine the additional diagnostic value of morphological changes in the fECG throughout the pregnancy.

Appendix A

Bayesian thresholding

A.1 Introduction into Bayesian probability

The basis of Bayesian probability lies in the dependence of two variables A and B. It enables to calculate the probability that A is true, given the occurrence of variable B. This probability is represented as $P(A|B)$. The chance that both A and B are true $P(A\&B)$, is thus given by two equations:

$$\begin{aligned} P(A\&B) &= P(A|B)P(B) && \text{(A.1)} \\ P(A\&B) &= P(B|A)P(A) && \text{(A.2)} \end{aligned}$$

From this set of equations, Bayes' theorem is then deduced as

$$\begin{aligned} P(B|A)P(A) &= P(A|B)P(B) && \text{(A.3)} \\ P(B|A) &= \frac{P(B)P(A|B)}{P(A)} && \text{(A.4)} \end{aligned}$$

For the current study, a different interpretation of Bayes' theorem is of importance. In this interpretation, the plausibility of a certain hypothesis (H) on an experimental outcome, is estimated based on the information of the outcome of the experiment (E). Bayes' theorem allows to calculate this probability, and Eq. A.4 becomes

$$P(H|E) = \frac{P(H)P(E|H)}{P(E)} \tag{A.5}$$

meaning, the probability of hypothesis H given the measurement E, expressed in the probability on E given hypothesis H. The probability $P(H)$ is called the *prior* and contains all a priori information about the system. $P(E|H)$ is the *likelihood* and describes the probability on E given the prior knowledge H and I. Finally, the factor

$P(E)$ is a normalization factor, describing the total probability on measurement E given all hypotheses. $P(E)$ is given by

$$P(E) = \sum_{i \in M} P(H_i)P(E|H_i) \tag{A.6}$$

with M all possible hypotheses. Since $P(E)$ is a normalization constant, this is typically left out in further calculations. In this context, $P(.)$ then describes the likelihood in stead of the probability.

$$P(H|E) \propto P(H)P(E|H) \tag{A.7}$$

A.2 Bayesian probability for threshold estimation

QRS detection is usually determined based on an amplitude threshold value. The R-peak locations are identified by the signals that exceed this threshold. The amplitude of the QRS-complexes can vary substantially and abruptly, hence the use of a dynamic threshold is favored over a fixed threshold.

The goal of this Bayesian approach is to design an adaptive threshold, which value is updated according to the previous and new statistical information provided by the signal. The instantaneous threshold ($\xi_{i,t}$), that is determined directly from the instantaneous information provided by the signal at each instant t, is defined by:

$$\xi_{i,t} = g \max\{|SAD_\tau|\} - (1-g)\min\{|SAD_\tau\} \tag{A.8}$$

with $|SAD_\tau| = |SAD[t-\tau]|, \ldots |SAD[t]|$, τ the time corresponding to the RR interval and g a constant that is experimentally determined. This instantaneous threshold, however, is based on ECG signal that is most likely also corrupted by noise. Furthermore, this non-optimal threshold does not uses any prior information of previously determined thresholds. Therefore, in this Bayesian approach, an optimized threshold ($\xi_{o,t}$) is estimated using the statistical instantaneous and previous information of the signal.

The connection between the instantaneous threshold $\xi_{i,t}$ and the optimal threshold $\xi_{o,t}$ can be described by the following state-space model (Figure A.1)

$$\begin{cases} \xi_{o,t+1} & = \xi_{o,t} + \nu_t \\ \xi_{i,t+1} & = \xi_{o,t+1} + \eta_{t+1} \end{cases}$$

Here, ν_t represents the variation between the optimized threshold values $\xi_{o,t+1}$ and $\xi_{o,t}$, and η_{t+1} describes the contribution of artifacts to the instantaneous threshold $\xi_{i,t+1}$. In order to create an analytic solution and small computational complexity for the threshold, both ν_t and η_{t+1} are assumed gaussian distributed with zero mean and variances $\sigma^2_{\nu,t}$ and $\sigma^2_{\eta,t+1}$ respectively.

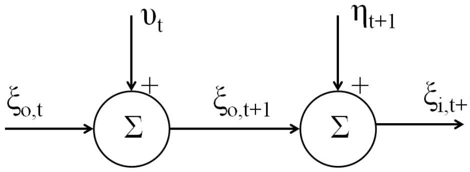

Figure A.1 – *Illustration of the state-space model that describes the evolution of the optimized threshold for QRS detection.*

The goal is to estimate the new optimal threshold value $\xi_{o,t+1}$, given the available information of the signal ($\xi_{o,t}$, $\sigma^2_{\nu,t}$, $\sigma^2_{\eta,t+1}$, and $\xi_{i,t}$). The solution to this type of problems, can be solved by Bayesian probability. Bayes' theorem states that the probability of a certain hypothesis H (in this case $\xi_{o,t+1}$) to be true, given the actual measurement E (in this case $\xi_{i,t}$) and the input information I ($\xi_{o,t}$, $\sigma^2_{\nu,t}$, and $\sigma^2_{\eta,t+1}$), is calculated by

$$p(\xi_{o,t+1}|\xi_{i,t+1}) = \frac{p(\xi_{o,t+1})p(\xi_{i,t+1}|\xi_{o,t+1})}{p(\xi_{i,t+1})} \tag{A.9}$$

In this equation, the posterior is given by the left hand side of the equation and the prior and the likelihood by the last two terms in Eq. A.10 respectively. As in section A.1 $p(\xi_{i,t+1}$ is only a normalization factor and Eq. A.9 can be written as

$$p(\xi_{o,t+1}|\xi_{i,t+1}) \propto p(\xi_{o,t+1})p(\xi_{i,t+1}|\xi_{o,t+1}) \tag{A.10}$$

From the first equation in the state-space representation in Eq. A.2 the prior can be determined. Since $\xi_{o,t+1}$ is independent of $\sigma^2_{\eta,t+1}$ and $\sigma^2_{\nu,t}$ is assumed gaussian, the prior can be written as a gaussian distribution

$$p(\xi_{o,t+1}) = \mathcal{N}(\hat{\xi}_{o,t}, \sigma^2_{\hat{\xi}_{o,t}} + \sigma^2_{\nu,t}) \tag{A.11}$$

in which $\hat{\xi}_{o,t}$ represents the mean of the distribution of $\xi_{o,t}$ and $\sigma^2_{\hat{\xi}_{o,t}}$ the variance. The notation $\mathcal{N}(x,y)$ stands for a gaussian distribution with mean x and variance y. In the same manner, now using the second equation in the state-space representation in Eq. A.2 and assuming a gaussian distribution of $\sigma^2_{\eta_{t+1}}$, the likelihood can also be described by a gaussian

$$p(\xi_{i+1,t+1}|\xi_{o,t+1}) = \mathcal{N}(\hat{\xi}_{o,t}, \sigma^2_{\eta,t+1}) \tag{A.12}$$

Substituting Eq. A.11 and A.12 into Eq. A.10 gives

$$p(\xi_{o,t+1}|\xi_{i,t+1}) = \mathcal{N}(\hat{\xi}_{o,t}, \sigma^2_{\hat{\xi}_{o,t}} + \sigma^2_{\nu,t})\mathcal{N}(\hat{\xi}_{o,t}, \sigma^2_{\eta,t+1}) \tag{A.13}$$

Since the product of two Gaussians is again a Gaussian, the posterior can thus again be written as

$$p(\xi_{o,t+1}|\xi_{i,t+1}) = \mathcal{N}(\hat{\xi}_{t+1}, \sigma^2_{\hat{\xi}_{o,t+1}}) \tag{A.14}$$

for which the mean is given by

$$\hat{\xi}_{o,t+1} = \hat{\xi}_{o,t} + \frac{\sigma^2_{\hat{\xi}_{o,t}} + \sigma^2_{\nu,t}}{\sigma^2_{\hat{\xi}_{o,t}} + \sigma^2_{\nu,t} + \sigma^2_{\eta,t+1}} (\xi_{i,t+1} - \xi_{o,t}) \tag{A.15}$$

and the variance

$$\sigma^2_{\hat{\xi}_{o,t+1}} = \frac{(\sigma^2_{\hat{\xi}_{o,t}} + \sigma^2_{\nu,t})\sigma^2_{\eta,t+1}}{\sigma^2_{\hat{\xi}_{o,t}} + \sigma^2_{\nu,t} + \sigma^2_{\eta,t+1}} \tag{A.16}$$

Rewriting the terms and introducing the Kalman gain K_t gives

$$\hat{\xi}_{o,t+1} = \hat{\xi}_{o,t} + K_t(\xi_{i,t+1} - \hat{\xi}_{o,t}) \tag{A.17}$$

$$\sigma^2_{\hat{\xi}_{o,t+1}} = \sigma^2_{\hat{\xi}_{o,t}} + \sigma^2_{\nu,t} - K_t(\sigma^2_{\hat{\xi}_{o,t}} + \sigma^2_{\nu_{o,t}}) \tag{A.18}$$

with K_t

$$K_t = \frac{\sigma^2_{\hat{\xi}_{o,t}} + \sigma^2_{\nu,t}}{\sigma^2_{\hat{\xi}_{o,t}} + \sigma^2_{\nu,t} + \sigma^2_{\eta,t+1}} \tag{A.19}$$

The interpretation o Eq. A.17 and Eq. A.18 can be found in section 3.3.1.

A.3 Incorrect implementation of Vullings et al. in previous studies

In previous studies [48,49,51], the implementation of the peak detection algorithm of Vullings et al. deviates from its theoretical description and does not perform optimal. As explained in Appendix A.2, the estimated optimal threshold value is determined by means of Eq. A.17, A.18 and A.19. In previous studies, however, the variance $\sigma^2_{\nu,t}$ is not taken into account. Due to this different implementation, the estimated threshold $\hat{\xi}_{o,t}$ is unable to rapidly decrease back to normal values after an artifact with an amplitude higher than the R-peak amplitude has occurred. This is effect is shown in Fig. A.2a. The exact reason why the optimized threshold is unable to rapidly decreased back to normal values with this previous implementation is explained here.

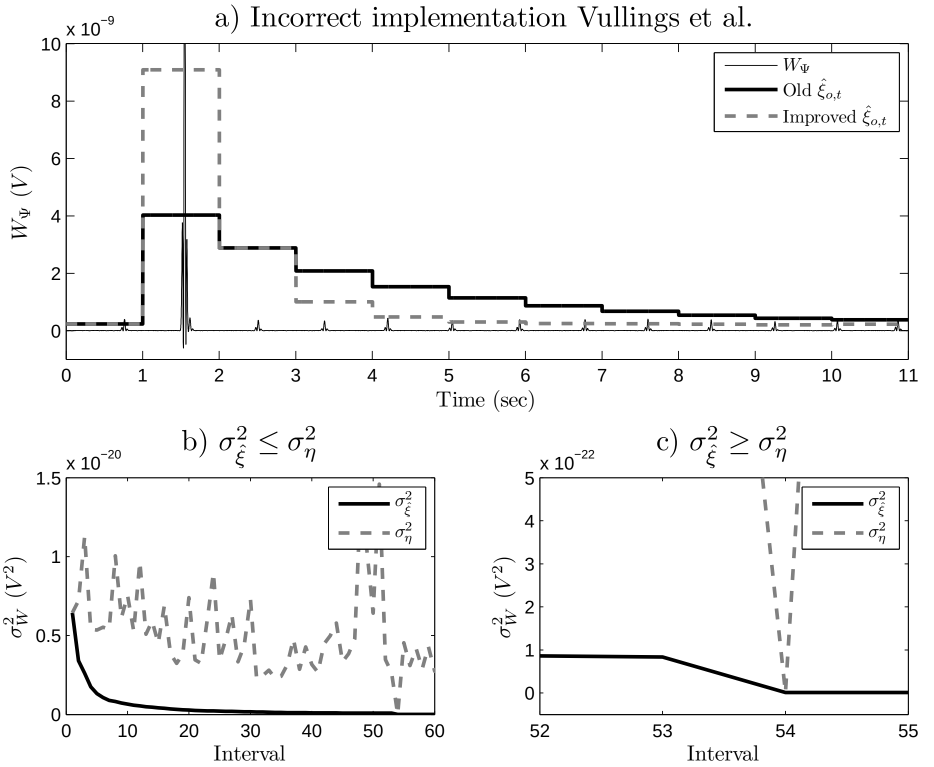

Figure A.2 – *(a) The effect of an artifact on the original and improved threshold* $\xi_{o,t}$ *of the peak detection algorithm of Vullings et al. In the implementation of previous studies,* $\xi_{o,t}$ *is unable to rapidly return to the basal threshold value after the artifact (rigid line). After correct implementation,* $\xi_{o,t}$ *is able to rapidly return to basal threshold value (dotted line). (b) The decrease of* $\sigma^2_{\hat{\xi}_{o,t}}$ *if* $\sigma^2_{\hat{\xi}_{o,t}}$ *is larger than* $\sigma^2_{\eta,t}$*. (c) The decrease of* $\sigma^2_{\hat{\xi}_{o,t}}$ *if* $\sigma^2_{\hat{\xi}_{o,t}}$ *is smaller than* $\sigma^2_{\eta,t}$*.*

In the implementation of previous studies Eq. A.18 simplified to

$$\sigma^2_{\hat{\xi}_{o,t+1}} = \frac{\sigma^2_{\hat{\xi}_{o,t}} \sigma^2_{\eta,t+1}}{\sigma^2_{\hat{\xi}_{o,t}} + \sigma^2_{\eta,t+1}} \tag{A.20}$$

and the Kalman Gain of Eq. A.19 to

$$K_t = \frac{\sigma^2_{\hat{\xi}_{o,t}}}{\sigma^2_{\hat{\xi}_{o,t}} + \sigma^2_{\eta,t+1}} \tag{A.21}$$

Furthermore, the value of K_t was bounded by an experimentally determined lower limit (K^{min}) and upper limit (K^{max}) of 0.3 and 0.7, respectively.

In previous implementations, the variance $\sigma^2_{\hat{\xi}_{o,t}}$ in Eq. A.20 would always decrease. If $\sigma^2_{\hat{\xi}_{o,t}}$ is much larger than $\sigma^2_{\eta,t+1}$, Eq. A.20 becomes

$$\sigma^2_{\hat{\xi}_{o,t+1}} \sim \sigma^2_{\eta,t+1} \tag{A.22}$$

and $\sigma^2_{\hat{\xi}_{o,t+1}}$ decreases, since $\sigma^2_{\eta,t+1} \leq \sigma^2_{\hat{\xi}_{o,t}}$. On the other hand, in case $\sigma^2_{\hat{\xi}_{o,t}}$ is much smaller than $\sigma^2_{\eta,t+1}$, Eq. A.20 becomes

$$\sigma^2_{\hat{\xi}_{o,t+1}} \sim \sigma^2_{\hat{\xi}_{o,t}} \tag{A.23}$$

and $\sigma^2_{\hat{\xi}_{o,t+1}}$ again decreases, since now $\sigma^2_{\hat{\xi}_{o,t}} \leq \sigma^2_{\eta,t+1}$. Both scenarios are displayed in Fig. 4.6b and c respectively.

As a consequence, $\sigma^2_{\hat{\xi}_{o,t}}$ is practically always smaller than $\sigma^2_{\eta,t+1}$ and, hence, K_t in Eq. A.21 is always small. The amplitude of the optimized threshold, $\hat{\xi}_{o,t+1}$ in Eq. A.17 is thus mostly determined by the previous optimized threshold $\hat{\xi}_{o,t}$.

In case a large artifact disturbs the fECG, $\sigma^2_{\eta,t+1}$ is large. The lower limit K^{min} allows the threshold value to adapt to the noise amplitude, as shown in Fig. A.2a. Due to the high value of $\sigma^2_{\eta,t+1}$, the new value of $\sigma^2_{\hat{\xi}_{o,t+1}}$ is, however, even further decreased. Therefore, the value of K still remains K^{min} in the period after the large artifact where the signal has returned to its normal value. The new (normal) value of $\hat{\xi}_{o,t+1}$ is thus still mostly determined by the old (artifact) value $\hat{\xi}_{o,t}$ and the threshold is only returned to its normal value slowly.

To allow for a rapid adaptation of the optimized threshold after a large artifact, the variance $\sigma^2_{\nu,t}$ is included in the implementation. Since in Eq. A.2 the parameter ν stands represents the change in consecutive optimized thresholds $\xi_{o,t}$ (i.e. the first derivative of $\xi_{o,t}$), the variance of ν is estimated as the second derivative of $\xi_{o,t}$. After implementation, the optimized threshold value is able to adjust rapidly after an artifact, as shown in Fig A.2.

Appendix B

Cohen's kappa test

The Cohen's kappa coefficient is a statistical measure for the inter observer agreement. The test requires a measure for the occurrence that both observers annotate a peak (N_{yy}), one of the two observers annotates a peak (N_{yn} and N_{ny}), and both observers do not annotate a peak (N_{nn}), as indicated in Table B.1. To obtain these values, all 12 annotated recordings are divided into intervals of length 430ms (assuming an average heart rate of 140BPM) and each interval is assumed to contain approximately one heart beat. In total 5580 are obtained for the Cohen's Kappa test. It is then determined for each interval whether a peak was annotated by an observer.

The κ value is calculation by correcting the percentage of agreement (P_o), with the random probability of that agreement (P_e)

$$\kappa = \frac{P_o - P_e}{1 - P_e} \tag{B.1}$$

The percentage of agreement is given by

$$P_o = \frac{N_{yy} + N_{nn}}{N_{tot}} \tag{B.2}$$

In which N_{tot} is the total number of annotations. The random probability that both observers give the same value is calculated as

$$P_e = \underbrace{\frac{N_{yy} + N_{yn}}{N_{tot}} \frac{N_{yy} + N_{ny}}{N_{tot}}}_{\text{P(both correct)}} + \underbrace{\frac{N_{yn} + N_{nn}}{N_{tot}} \frac{N_{ny} + N_{nn}}{N_{tot}}}_{\text{P(both incorrect)}} \tag{B.3}$$

Table B.1 – *Values used for the Cohen's kappa test.*

	observer2: Peak	observer1: No peak
observer1: Peak	N_{yy}	N_{yn}
observer1: No peak	N_{ny}	N_{nn}

Appendix C

Journal paper submitted to The Journal of Physiology

Fetal heart rate variability in frequency-domain during pregnancy, obtained from non-invasive electrocardiogram recordings

J.O.E.H. van Laar, G.J.J. Warmerdam, R. Vullings, C.H.L. Peters, S. Houterman, P.F.F. Wijn, P. Andriessen, C. van Pul and S.G. Oei. *Submitted for publication*

Abstract

Objective: First, to study the relation between gestational age and spectral estimates of fetal heart rate variability, determined by non-invasive electrocardiogram. Second, to study the influence of fetal rest-activity state on spectral estimates.

Design: Prospective longitudinal study.

Setting: Tertiary-care teaching hospital.

Population: 35 healthy women, with an uneventful pregnancy.

Methods: A new method was developed to measure the fetal electrocardiogram non-invasively. Measurements were performed at regular time intervals (2 to 4 weeks) from a gestational age of 14 up to 41 weeks. Simultaneous ultrasound measurements were performed to assess fetal rest-activity state. From the fetal electrocardiogram measurements beat-to-beat heart rate was obtained for spectral analysis. 64-second segments of fetal heart rate were selected. Absolute and normalised power in the low (0.04-0.15 Hz) and high frequency band (0.4-1.5 Hz) were obtained, using a Fourier transform. Median values of spectral estimates, of the available segments from each measurement, were calculated. Data were analysed using linear regression for the periods below and above 30 weeks separately. For comparison between active and quiet state an independent *t* test was used.

Main outcome measures: First, spectral estimates as a function of gestational age. Second, spectral values during the active and the quiet state.

Results: The percentage of successfully retrieved heart rate data depend on gestational age. Before 18 and between 30 and 34 weeks no segments could be retrieved. During 21 to 30 weeks a significant increase in absolute low and high frequency power was observed, while no change in normalised spectral estimates was observed. During 34 to 41 weeks a (non-significant) decrease in absolute and normalised low frequency power and a (non-significant) increase in absolute and normalised high frequency power were observed. During the active state (near) term, absolute and normalised low frequency power were significantly higher and normalised high frequency power was significantly lower compared to the quiet state.

Conclusions: The observed increase in absolute spectral estimates, in preterm fetuses, was probably due to increased sympathetic and parasympathetic modulation and might be a sign of autonomic development. The observed non-significant changes in spectral estimates in (near) term fetuses might be associated with changes in behavioural state and increased parasympathetic modulation. However, more research is needed to confirm this. We found sympathetic predominance during the active state in (near) term fetuses.

Introduction

Cardiotocography is the widespread method for fetal monitoring despite its poor diagnostic value to detect fetal distress[1]. Poor specificity of this method has resulted in increased rates of operative deliveries without a significant improvement of long term fetal outcome[1]. Additional ST-waveform analysis of the fetal electrocardiogram (ECG; STAN®, Neoventa Medical, Moelndal, Sweden) and fetal scalp blood sampling (FBS), applied in case of a non-reassuring CTG, have limited capability to improve neonatal outcome or to reduce unnecessary interventions[1,2,3,4]. Besides, these techniques can only be used during labour at term due to their invasiveness. Therefore, an urgent need exists to develop non-invasive methods that provide complementary information on fetal wellbeing and enable intra- and antepartum use during the term and preterm period.

The analysis of variations in beat-to-beat heart rate is an established non-invasive technique for investigating the autonomic cardiac control system[5]. In human adults, heart rate variability (HRV) estimated by spectral analysis reflects the modulation of the sympathetic and parasympathetic limbs of the autonomic nervous system[5]. The low frequency (LF) cardiovascular fluctuations are ascribed to the baroreceptor reflex and are under sympathetic and parasympathetic control, whereas high frequency (HF) fluctuations are associated with respiration and are under parasympathetic control only[5,6].

As in human adults, quantifying the variations in beat-to-beat fetal heart rate by spectral analysis can be used to monitor autonomic nervous system modulation and may provide an early diagnostic tool for detection of fetal distress[7]. Spectral analysis during labour was previously performed on beat-to-beat heart rate, obtained from direct fetal ECG recordings by scalp electrode[7,8,9,10]. Our previous studies during labour showed that spectral estimates are associated with severe metabolic acidosis at birth[8] and might predict fetal distress in an early stage[9]. In addition, spectral estimates are related to fetal behavioural state and gestational age (GA) during labour at term[10].

Before using spectral analysis for fetal monitoring, more insight needs to be gained into normal autonomic development. However, at present, limited research has been done on human fetal HRV in frequency-domain, during the second and third trimester of pregnancy, and thus during the development of autonomic reflex mechanisms[11,12,13]. In order to measure spectral estimates during gestation, beat-to-beat fetal heart rate should be obtained non-invasively. Van Leeuwen et al. used magnetocardiography to measure fetal beat-to-beat heart rate[11]. Although this method produces a high quality fetal cardiac signal, it cannot be used in clinical practice due to the need of heavy magnetically shielded rooms. David et al. and Karin et al., measured beat-to-beat heart rate non-invasively from fetal ECG recordings[12,13]. However, both studies are limited considering developmental aspects, since no longitudinal follow up was performed during pregnancy. The three aforementioned studies reported conflicting results concerning changes in spectral estimates during the course of pregnancy. Two studies found an increase in LF and HF spectral estimates of HRV during the second and third trimester of pregnancy[11,12], while one study found a decrease in spectral estimates of HRV in mature fetuses compared with immature fetuses[13]. This discrepancy might be explained from the fact that these studies did not account for fetal movement during the third trimester. Changes in fetal HRV due to fetal rest-activity state occur after 30 weeks of gestation[14]. Since spectral estimates of fetal HRV are known to be associated with rest-activity states at term gestation[10,12], it is difficult to interpret spectral values without classifying fetal movements.

By measuring LF and HF spectral power at regular time intervals during gestation, the development of the fetal autonomic cardiac control can be examined. We developed a new method to obtain the fetal ECG non-invasively from the maternal abdomen[15,16]. This method allows for beat-to-beat detection of the fetal R-waves and provides fetal beat-to-beat heart rate and spectral estimates non-invasively. The feasibility of this method to study the development of fetal autonomic cardiac control during gestation has not yet been investigated before.

The first objective of the current study is to present a non-invasive method for fetal ECG and beat-to-beat heart rate detection and to evaluate its clinical feasibility. The second objective is to study the relationship between GA and spectral estimates of fetal HRV and to study the influence of fetal rest-activity states on spectral estimates after 30 weeks of gestation.

Methods

Subjects

A prospective longitudinal study was performed in a tertiary-care teaching hospital. The study protocol was approved by the institutional review board at the Máxima Medical Centre, Veldhoven, the Netherlands. Patients were recruited consecutively from a healthy population, undergoing routine pregnancy follow up during one of the first outpatient visits. Only healthy women with an uneventful singleton pregnancy, not taking medication other than iron tablets or vitamins, were asked to participate before a GA of 12 weeks. Exclusion criteria were women under the age of 18 years and multiple pregnancies. Participants were included after a written informed consent form was signed. Pregnancy duration was determined from the last menstrual period and confirmed by crown rump length at 10 to 12 weeks of gestation. Pregnancies complicated by hypertension, preeclampsia, fetal growth restriction, premature labour, diabetes mellitus, or fetal congenital malformations after inclusion were excluded. Only pregnancies which progressed uneventfully resulting in the delivery of a healthy infant with a birthweight above the 10th percentile corrected for GA, maternal parity and fetal sex[17] were included in the data analysis.

Data acquisition and signal processing

Non-invasive fetal ECG measurements were repeatedly performed antenatally. A non-invasive electrophysiologic monitor for obstetrics (NEMO), shown in Figure 9.1, was used to record and store the electrical activity on the maternal abdomen.

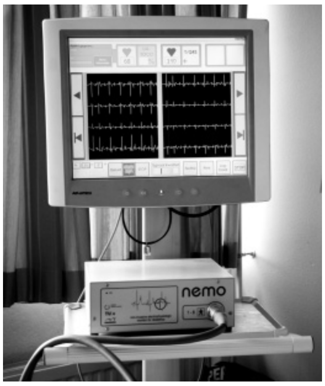

Figure 9.1. Prototype of the NEMO system.

The NEMO system was developed in the Máxima Medical Centre in cooperation with the Eindhoven University of Technology and Maastricht Instruments BV. The system was approved by the Medical Technical Service Department of the Máxima Medical Centre. Recordings were performed at approximately 14, 18, 22, 24, 26, 30, 34, 36, 38, and 40 weeks of gestation. Before starting a measurement, the woman's skin was prepared to reduce impedance by gentle excoriation of surface skin cells and by cleaning the skin with alcohol. Measurements were performed non-invasively using eight self-adhesive electrodes and one reference and one ground electrode on the maternal abdomen. The electrode configuration is shown in Figure 9.2.

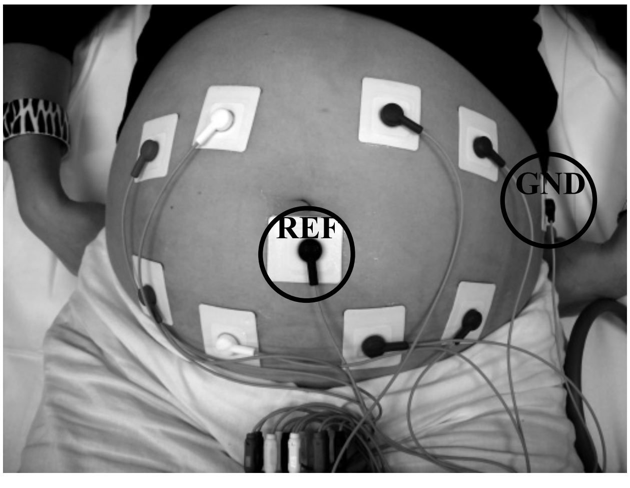

Figure 9.2. Electrode configuration for antepartum fetal ECG recording. GND: ground electrode. REF: reference electrode.

Each recording session took place between 8:00 h and 18:00 h, with the patient lying comfortable in a bed in semi recumbent position. During this time period, no important fluctuations in fetal HRV due to differences in time of the day were expected[18]. The electrode impedances were checked to ensure that they did not exceed 5 kΩ. The duration of recordings was approximately 45 minutes. Simultaneous ultrasound recordings (Aloka SSD-1000, Hitachi Aloka Medical, Tokyo, Japan) were performed to assess the fetal rest-activity state. Each fetus was visualised in a parasagittal plane. With the transducer in this position most of the fetal head and trunk and one or more limbs could be viewed.

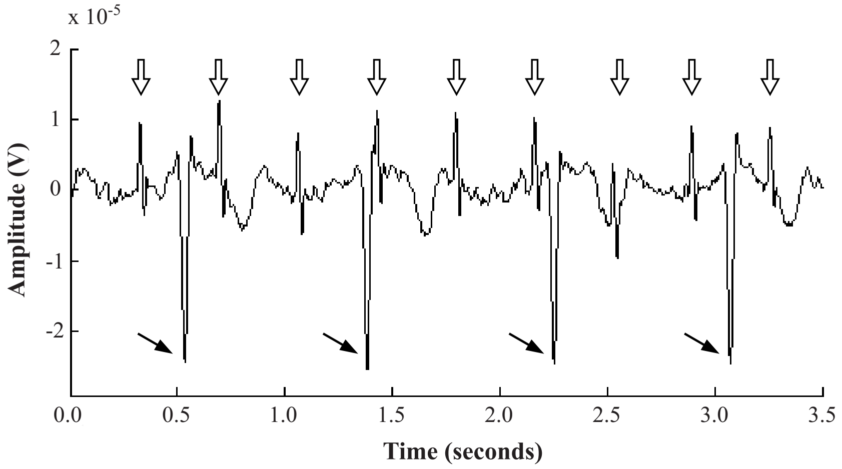

Figure 9.3. Filtered abdominal signal containing both maternal (↘) and fetal ECG (⇩).

The abdominal data were analysed off-line. The eight input signals were recorded with a sample frequency of 1000 Hz. The signals were bandpass filtered between 1.5 and 70 Hz in order to suppress high frequency noise and low frequency electronic drift. A 50 Hz notch filter was used to suppress power line interference. The maternal ECG waveform was estimated and subtracted from the signals, without affecting present fetal ECG complexes. This was done using a novel method that removed the maternal ECG by means of weighted averaging of maternal ECG segments[19]. Figure 9.3 shows an example of a filtered abdominal signal containing both maternal and fetal ECG. Figure 9.4 shows the signal after maternal ECG subtraction.

The eight resulting fetal ECG traces were processed to detect the beat-to-beat fetal heart rate. The signal-to-noise ratio of these signals is enhanced by spatially combining the signals[20]. R-peaks in the fetal ECG are detected and used to create the fetal beat-to-beat heart rate signals as described previously[20].

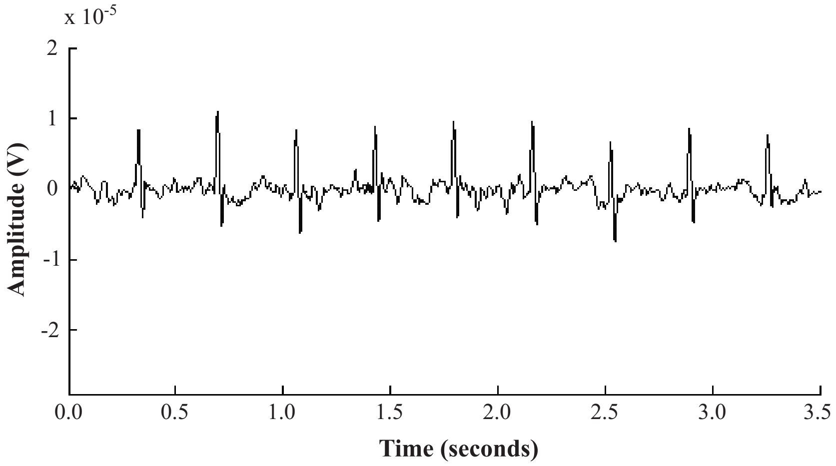

Figure 9.4. Filtered abdominal fetal signal after subtraction of the maternal ECG.

Spectral analysis

To prevent incorrect RR-intervals from dominating the spectrum, an RR-interval was automatically excluded if it exceeded the range of 0.2 to 1.3 seconds (46 to 300 beats per minute) or deviated more than 12% from preceding successive RR-intervals[9]. These incorrect RR-intervals were removed from the dataset and replaced by linear interpolation between the last preceding and the first succeeding correct RR-interval. From the beat-to-beat fetal heart rate data, 64-second segments were selected consecutively. To minimise the effect of artefact correction on the calculated spectral estimates, only segments with less than 5% artefact correction were included for analysis[21]. Visual inspection by an expert was performed to check for remaining artefacts, originating from misdetection of fetal R-peak. When a segment still contained an artefact, it was excluded for further analysis.

Spectral information about fetal beat-to-beat heart rate was obtained by using a Fourier transform. Beat-to-beat RR-intervals were resampled at 4 Hz and 256-point Fourier transforms were calculated for intervals of 64 seconds[22]. The direct current component was subtracted before calculating the Fourier transform. To reduce spectral leakage, the signal was multiplied with a Parzen window function. Based on previous studies[23], as well as the physiological range of fetal heart and respiratory movement rate, the following frequency bands were chosen: total frequency band: 0.04 to 1.5 Hz, LF: 0.04 to 0.15 Hz and HF: 0.4 to 1.5 Hz. Absolute spectral power values were expressed in squared milliseconds. After calculating the spectral power of fetal heart rate variability in these frequency bands, normalised values were calculated by dividing LF and HF power by total power.

Fetal rest-activity state

For each selected 64-second segment of fetal heart rate data, the corresponding ultrasound segment was analysed. All segments were divided into quiet sleep and active sleep, by visual inspection by a single observer with 8 years obstetric ultrasound experience. Assessment of fetal rest-activity states was based upon the presence or absence of fetal body movements. Body movements comprised the collective trunk, limb and head movements. When, after 34 weeks of gestation, the fetal rest-activity state could not be determined by ultrasound, the behavioural state was determined based on visual inspection of the fetal heart rate pattern as described by Nijhuis et al.[24]. In healthy fetuses from this GA, the relation between fetal movements and CTG pattern is so strong that the different states can be assessed reliably by visual identification of heart rate patterns alone[14].

Statistical methods

For each patient, for all available 64-second segments of heart rate data per GA group, median values were calculated for the absolute and normalised spectral power in the LF and the HF band. It is known that fetal ECG measurements are extremely difficult to obtain around 30 weeks of gestation due to the presence of the vernix caseosa, which electrically shields the fetus from its surroundings[25]. Since changes in fetal heart rate variability due to fetal rest-activity state only occur after 30 weeks of gestation[14], data were analysed separately for the periods below and above 30 weeks of gestation. The median spectral estimates were plotted as a function of GA. The median spectral values were normally distributed. Simple linear regression was used to study changes in spectral estimates over GA.

For the GA group above 30 weeks, analysis was repeated with restriction to fetal rest and activity, to examine the effect of fetal rest-activity state on the relation between spectral estimates and GA.

In addition, for the GA group above 30 weeks, the mean values of the median spectral estimates were compared during the active and quiet fetal state. For comparison between the active and quiet state an independent *t* test was used.

Statistical significance was assumed at an α level of 0.05.

Results

40 women were studied longitudinally during pregnancy. Measurements were performed from November 2006 up to August 2009. From the 40 patients under study, three patients were excluded because pregnancy was complicated by pregnancy induced hypertension. In addition, two patients were excluded because of preterm labour at a gestational age of respectively 31 and 32 weeks. The neonate born at 32 weeks of gestation was growth retarded (5th percentile for parity, GA and fetal sex) and had an anal atresia. From the remaining data, 330, 64-second segments of beat-to-beat heart rate data (2.75%) could

be used for spectral analysis. Figure 9.5 shows the percentage of usable segments, for the different GA groups.

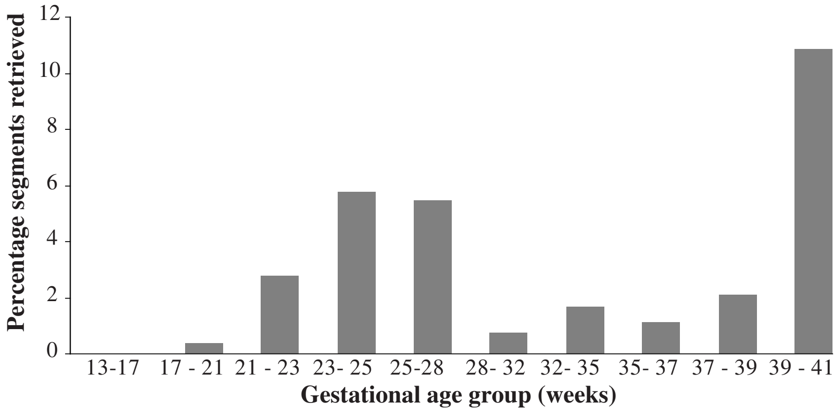

Figure 9.5. Percentage of 64-second segments, of beat-to-beat fetal heart rate data, that could be retrieved for Fourier transform, for each GA group.

The period between 17 and 21 weeks of gestation was excluded for further analysis since only five 64-second segments of heart rate data could be retrieved. Furthermore, no segment could be retrieved in the period between 30 and 34 weeks of gestation. In total, 325 segments remained for final analysis.

From the included 35 women, ten women were excluded because no good-quality fetal beat-to-beat heart rate could be retrieved from the abdominal recordings. For the remaining 25 women included for analysis, in total 213 abdominal measurements were performed (from which 325 segments could be used for analysis). The mean number of measurements per patient was 9 (standard deviation (sd) 1.6). The mean duration of each measurement was 42 minutes (sd 9). All mothers delivered at term. All neonates had a birthweight above the 10th percentile corrected for parity, GA and fetal sex. All neonates had an Apgar score of at least eight at 1 minute and at least nine at 5 minutes. All neonates had an umbilical artery pH > 7.05 and an umbilical artery base deficit ≤ 10. Patients' characteristics are shown in Table 9.1.

Figure 9.6 shows the absolute LF and HF power as a function of GA, for the GA period of 21 to 30 and 34 to 41 weeks. Linear regression lines were fitted to the data. A significant increase was seen in absolute LF and HF power, from 21 to 30 weeks of gestation. A non-significant decrease in LF and a non-significant increase in HF power were seen from 34 to 41 weeks of gestation.

Table 9.1. Characteristics of the patients included for analysis

	% or mean (standard deviation)
Maternal body mass index before pregnancy	23.6 (4.0)
Nulliparous	64%
Maternal age at birth (years)	32 (4)
Gestational age at birth (days)	279 (10)
Birthweight (grams)	3561 (543)
Apgar score at 5 minutes	10 (0.3)
Umbilical artery pH at birth	7.22 (0.08)
Umbilical artery base deficit at birth	7.3 (2.7)

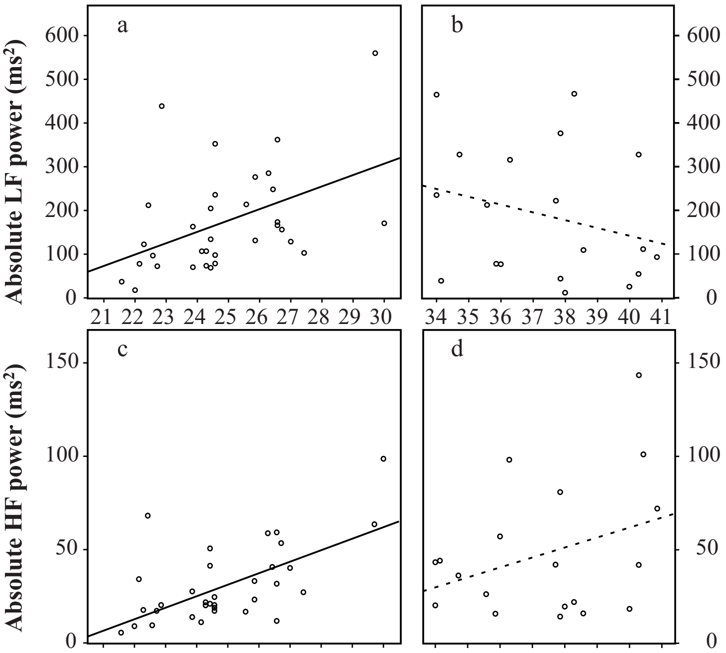

Figure 9.6. The association between absolute LF and HF power and GA, for the period of 21 to 30 and 34 to 41 weeks of gestation. a) R^2: 0.20 ($P = 0.009$), b) R^2: 0.08 ($P = 0.26$), c) R^2: 0.37 ($P = 0.0004$) and d) R^2: 0.12 ($P = 0.15$).

Figure 9.7 shows the normalised LF and HF power as a function of GA, for the GA period of 21 to 30 and 34 to 41 weeks. Linear regression lines were fitted to the data. For the normalised power, no significant trend was observed.

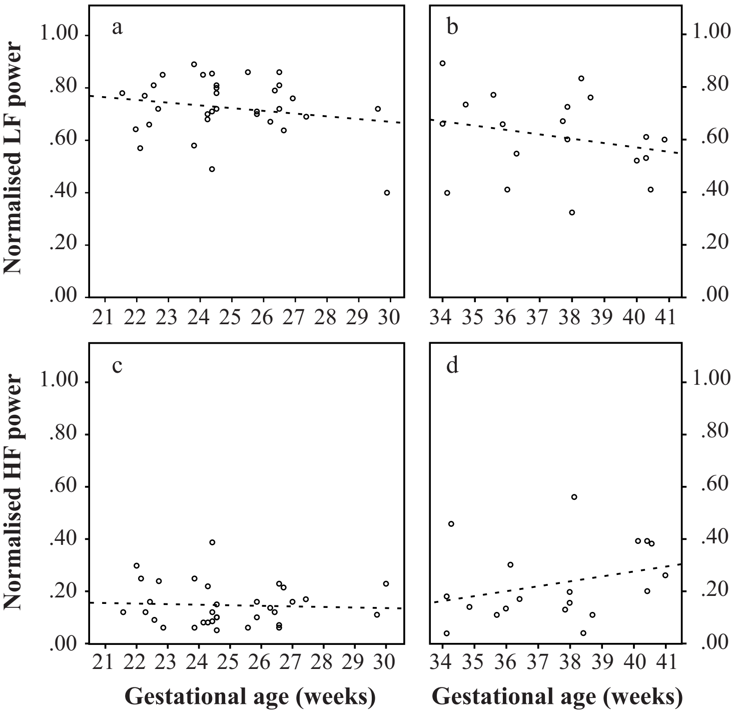

Figure 9.7. The association between normalised LF and HF power and GA, for the period of 21 to 30 and 34 to 41 weeks of gestation. a) R^2: 0.04 ($P = 0.28$), b) R^2: 0.06 ($P = 0.31$), c) R^2: 0.003 ($P = 0.76$) and d) R^2: 0.09 ($P = 0.21$).

From the available segments below 30 weeks of gestation, fetal rest-activity state could be determined based on ultrasound for 85 segments (43%). Of these, 86% was retrieved during the active state, while 14% was retrieved during the quiet state.

In the GA group of 34 to 41 weeks of gestation, rest-activity state could be classified based on ultrasound for 69 segments (54%). For the remaining 58 segments (46%), the state was assessed based on fetal heart rate pattern. From the selected segments, 38% was retrieved during active sleep and 62% during quiet sleep. Table 9.2 displays, the percentage of the selected segments in active sleep and quiet sleep for the different GA groups after 30 weeks of gestation.

Table 9.2. Percentage of segments with the fetus in the active state and in rest, for the GA groups after 30 weeks of gestation

GA	Active sleep	Quiet sleep
34-36	70%	30%
36-38	43%	57%
38-40	32%	68%
40-41	28%	72%

Table 9.3 shows the mean values of the median absolute and normalised LF and HF power, for the active and quiet state, for 34 to 41 weeks of gestation. During the active state, absolute and normalised LF power were significantly higher compared to the quiet state. During the quiet state, normalised HF power was significantly higher. To guarantee no bias was introduced by assessment of fetal rest-activity state by fetal heart rate pattern, the analysis was repeated for segments for which rest-activity state was solely assessed based on ultrasound. The results (not shown) were highly comparable and remained significant.

Table 9.3. Mean values of the median absolute and normalised LF and HF power for the active and quiet sleep state for the GA period of 34 to 41 weeks

	Active sleep	Quiet sleep	*P*-value
Absolute LF (ms^2)	555	151	0.002
Absolute HF (ms^2)	62	38	0.09
Normalised LF	0.77	0.59	0.005
Normalised HF	0.10	0.26	0.002

To study the effect of fetal behaviour on spectral estimates, the association between spectral estimates and GA was studied for rest and activity separately, for the GA period above 30 weeks. Figure 9.8 shows the absolute LF and HF power as a function of GA for the active and quiet sleep state. Linear regression lines were fitted to the data.

During the active sleep state, a non-significant increase in absolute LF and HF power was observed with progress of pregnancy. No (significant) trend was observed in normalised values during the active sleep state (results not shown). During the quiet sleep state, a non-significant decrease in absolute LF power and a non-significant increase in absolute HF power were observed. For the normalised values during the quiet sleep state a comparable (non-significant) trend was shown as for the absolute values (results not shown).

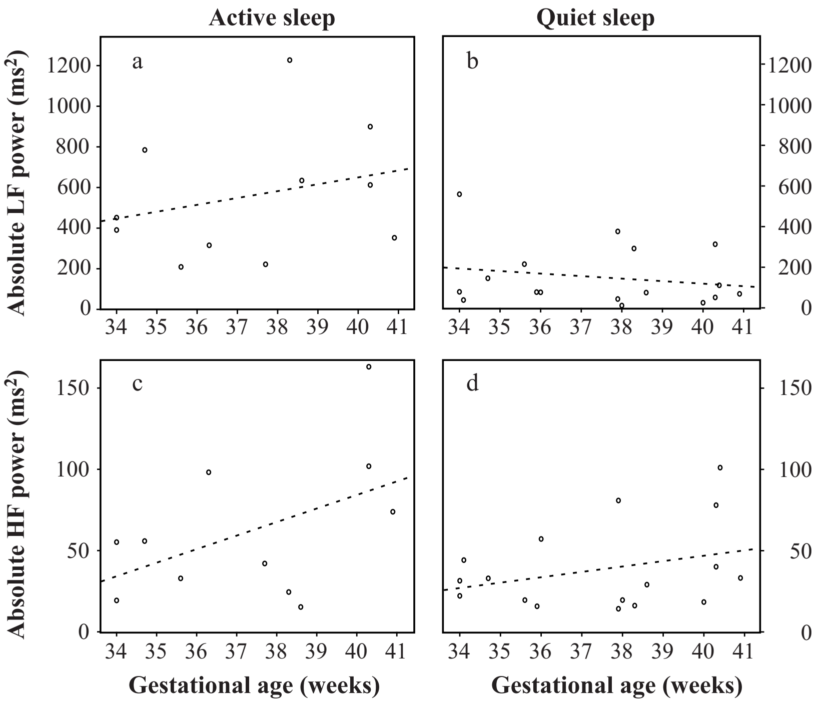

Figure 9.8. The association between the absolute LF and HF power and GA, for the active and quiet sleep state, for the period of 34 to 41 weeks of gestation. a) R^2: 0.08 ($P = 0.41$), b) R^2: 0.04 ($P = 0.44$), c) R^2: 0.23 ($P = 0.14$) and d) R^2: 0.10 ($P = 0.22$).

Discussion

Our group has developed a new method for non-invasive fetal ECG measurement[19,20]. This new method can be used during periods in pregnancy, in which other (invasive) techniques cannot be used for monitoring. Our results in a large study group showed that it is possible, yet difficult, to retrieve fetal beat-to-beat heart rate from non-invasive abdominal fetal ECG measurements. Spectral analysis was feasible in approximately 3% of abdominal data and thus further improvements need to be made in signal processing. We were not capable of retrieving fetal beat-to-beat heart rate from the abdominal measurements before 18 weeks and between 30 and 34 weeks of gestation. Below 18 weeks this was probably due to the small size of the fetal heart. This results in very low amplitude of the fetal ECG, rendering it undetectable on the maternal abdomen. Between 30 and 34 weeks of gestation, the presence of the vernix caseosa, which electrically isolates the fetal heart[25], probably caused for significant attenuation of the

ECG signal. During the very preterm period (21 to 28 weeks), approximately 5% of data was suitable for spectral analysis. At term, approximately 7% of data was suitable for spectral analysis. Probably, during the term period the disappearance of the vernix caseosa and the relatively large fetal heart, made it easier to detect the fetal signal from the combined fetal-maternal signals measured on the maternal abdomen.

Very preterm period (21 to 30 weeks of gestation)

For the very preterm period we observed a significant increase in absolute LF and HF power of fetal heart rate variability with progressing pregnancy. We hypothesise that this increase was due to increased sympathetic and parasympathetic modulation of the fetal heart resulting from maturation of the fetal autonomic nervous system. This is in accordance with animal studies that showed an increase in sympathetic and parasympathetic cardiac modulation in premature fetuses compared to immature fetuses[26].

It is unlikely that that the observed changes in spectral estimates before 30 weeks of gestation were due to changes in fetal breathing movements or rest-activity state. Although fetal breathing movements occurred as early as 10 weeks of gestation[27], the high frequency peak that was observed during breathing at term[28], could not be observed at 26 weeks of gestation[29]. In addition, the incidence of fetal breathing movements did not change between 24 and 28 weeks of gestation[30]. The incidence of fetal movements decreased as pregnancy progresses[31]. From 24 to 28 weeks of gestation a healthy fetus on average made 150 to 200 movements each hour[31]. Therefore, it was expected that most selected 64-second segments of heart rate data below 30 weeks were measured during fetal activity, as was confirmed by our analysis of the corresponding ultrasound measurements. In addition, in term fetuses during the active state, LF power was high compared to quiescence[10]. Although short rest-activity cycles were first noticed at 23 weeks of gestation, fetal heart rate variability was similar during fetal activity and rest up to 30 weeks of gestation[14] and behavioural states could not be observed[32].

The observed increase in absolute LF and HF power was not reflected in the normalised values during the very preterm period. This might be due to a comparable relative increase in both absolute LF and HF power and to the relatively dominant sympathetic system in premature fetuses. This was reflected in the high normalised LF power and is in accordance with animal studies that have shown that the sympathetic tone predominates over the parasympathetic tone during the intrauterine life[26].

The (near) term period (34 to 41 weeks of gestation)

For the (near) term fetuses a non-significant decrease in absolute LF and a non-significant increase in absolute HF power were observed. A LF power decrease, after 30 weeks was also described by David et al.[12]. Fetal activity is known to increase fetal HRV from approximately 30 weeks of gestation onwards[14], and a decrease in fetal movements with GA was reported[31]. Therefore, a LF power decrease after 30 weeks, is expected to occur due to a decrease in fetal movements. Later in pregnancy, starting in the 34th week of gestation, fetal behavioural states appear[33]. As these states are partly defined on the basis of HRV, it seems relevant to consider them in the interpretation of HRV measures.

Furthermore, absolute and normalised LF power were found significantly higher and normalised HF power significantly lower during fetal activity compared to rest. A non-significant increase in absolute HF power was observed during the active state. These results were similar to those obtained with invasive measurements during labour at term[10].

If analysis was repeated with restriction to periods of fetal rest and activity (as shown in Figure 9.8), LF power increased non-significantly as a function of GA during activity, while LF power decreased non-significantly during rest. Since for the selected segments the time spent in rest increased with GA during the (near) term period (as shown in Table 9.2), a decrease in fetal activity might explain the overall decrease in LF power as pregnancy progresses.

During fetal activity, the observed non-significant increase in absolute LF power, with advancing gestational age, might be due to a more mature autonomic nervous system, which is capable of adapting to increased metabolic demands during fetal activity. This might be a sign of autonomic functional development. However, since the trend was not significant, probably due to the limited number of usable segments, further study is necessary to confirm this hypothesis.

An increase in absolute and normalised HF power was found, in our studies, for invasive measurements during the term period during labour[10]. We observed a similar trend towards increased absolute and normalised HF power near term, in the present study. Because this trend was independent of fetal rest-activity state, it cannot be explained by changes in fetal behaviour. This trend might suggest continuing parasympathetic maturation during the term period and increasing influence of the vagal system. This is in line with Assali et al., who found a marked rise in parasympathetic tone during the neonatal period and up until the adult state[26].

For the selected segments of heart rate data in the current study, for the (near) term fetuses, 62% was in quiet sleep and 38% was in active sleep. Previous studies reported that the quiet sleep state accounts for approximately 30% and the active sleep state for 60% of the behaviour of term fetuses and that awake states appear rarely[34]. Therefore, it seems that fetal heart rate detection is more successful during rest, due to fewer disturbances caused by motion artefacts.

Limitations

The main limitation of the presented study is the very small percentage of available signals suitable for analysis. However, our new method is one of the first by which fetal HRV studies can be performed non-invasively based on indirect fetal ECG measurement. In addition, we prefer to obtain good-quality data over a high quantity of data to make sure reliable results are obtained. Improvement of both equipment and algorithm is still necessary to obtain more good-quality data. Furthermore, due to the limited amount of data for analysis, we were unable to analyse inter- and intraindividual variation in the relation of spectral estimates with GA, although the study set-up was longitudinal. In addition, due to missing data and large ranges of individual spectral estimates, statistical significance was often not reached. Therefore, we were careful in drawing conclusions on maturational aspects, although trends were visible.

Conclusions

Our non-invasive fetal ECG method enables to measure fetal HRV in frequency-domain during the very preterm and the term period. The observed changes during the premature period are in accordance with those seen in animal studies and our results in the (near) term period are fully in accordance with the previous literature on invasive measurements during labour at term. This is the first study that measures spectral estimates longitudinally and relates spectral estimates to fetal state. Further progress in signal processing will enable improved study of the relation between spectral estimates and GA and allow for longitudinal analysis.

References

1. Alfirevic Z, Devane D, Gyte GM. Continuous cardiotocography (CTG) as a form of electronic fetal monitoring (EFM) for fetal assessment during labour. Cochrane Database Syst Rev 2008.
2. Neilson JP. Fetal electrocardiogram (ECG) for fetal monitoring during labour. Cochrane Database Syst Rev 2011.
3. Mahendru AA, Lees CC. Is intrapartum fetal blood sampling a gold standard diagnostic tool for fetal distress? Eur J Obstet Gynecol Reprod Biol 2011;156:137-139.
4. Goodwin TM, Milner-Masterson L, Paul RH. Elimination of fetal scalp blood sampling on a large clinical service. Obstet Gynecol 1994;83:971-974.
5. Task Force of the European Society of Cardiology and the North American Society of Pacing and Electrophysiology. Heart rate variability: standards of measurement, physiological interpretation and clinical use. Circulation 1996;93:1043-1065.
6. Akselrod S, Gordon D, Ubel FA, Shannon DC, Berger AC, Cohen RJ. Power spectrum analysis of heart rate fluctuation: a quantitative probe of beat-to-beat cardiovascular control. Science 1981;213: 220-222.
7. Siira SM, Ojala TH, Vahlberg TJ, Jalonen JO, Välimäki IA, Rosén KG, Ekholm EM. Marked fetal acidosis and specific changes in power spectrum analysis of fetal heart rate variability recorded during the last hour of labour. BJOG 2005;112:418-423.
8. van Laar JO, Peters CH, Vullings R, Houterman S, Bergmans JW, Oei SG. Fetal autonomic response to severe acidaemia during labour. BJOG 2010;117:429-437.
9. van Laar JO, Peters CH, Houterman S, Wijn PF, Kwee A, Oei SG. Normalized spectral power of fetal heart rate variability is associated with fetal scalp blood pH. Early Hum Dev 2011;87:259-263.
10. van Laar JO, Peters CH, Vullings R, Houterman S, Oei SG. Power spectrum analysis of fetal heart rate variability at near term and post term gestation during active sleep and quiet sleep. Early Hum Dev 2009;85:795-798
11. van Leeuwen P, Geue D, Lange S, Hatzmann W, Gronemeyer D. Changes in the frequency power spectrum of fetal heart rate in the course of pregnancy. Prenat Diagn 2003;23:909-916.
12. David M, Hirsch M, Karin J, Toledo E, Akselrod S. An estimate of fetal autonomic state by time-frequency analysis of fetal heart rate variability. J Appl Physiol 2007;102:1057-1064.
13. Karin J, Hirsch M, Akselrod S. An estimate of fetal autonomic state by spectral analysis of fetal heart rate fluctuations. Pediatr Res 1993;34:134-138.
14. Pillai M, James D. The development of fetal heart rate patterns during normal pregnancy. Obstet Gynecol 1990;76:812-816.
15. Vullings R. Non-invasive fetal electrocardiogram: analysis and interpretation. PhD Thesis, Eindhoven University of Technology, Eindhoven, 2010.
16. Peters CH. Time-scale analysis of antepartum fetal heart rate variability. PhD Thesis, Eindhoven University of Technology, Eindhoven, 2011.
17. Visser GH, Eilers PH, Elferink-Stinkens PM, Merkus HM, Wit JM. New Dutch reference curves for birthweight by gestational age. Early Hum Dev 2009;85:737-744.
18. Lange S, van Leeuwen P, Geue D, Hatzmann W, Grönemeyer D. Influence of gestational age, heart rate, gender and time of day on fetal heart rate variability. Med Biol Eng Comput 2005;43:481-486.
19. Vullings R, Peters CH, Sluijter R, Mischi M, Oei SG, Bergmans JW. Dynamic segmentation and linear prediction for maternal ECG removal in antenatal abdominal recordings. Physiol Meas 2009;30: 291-307.

20. Vullings R, Peters CH, Hermans MJ, Wijn PF, Oei SG, Bergmans JW. A robust physiology-based source separation method for QRS detection in low amplitude fetal ECG recordings. Physiol Meas 2010;31:935-951.
21. Peters C, Vullings R, Bergmans J, Oei G, Wijn P. The effect of artifact correction on spectral estimates of heart rate variability. Conf Proc IEEE Eng Med Biol Soc 2008:2669-2672.
22. Peters CH, ten Broeke ED, Andriessen P, Vermeulen B, Berendsen RC, Wijn PF, Oei SG. Beat-to-beat detection of fetal heart rate: Doppler ultrasound cardiotocography compared to direct ECG cardiotocography in time and frequency domain. Physiol Meas 2004;25:585-593.
23. de Beer NA, Andriessen P, Berendsen RC, Oei SG, Wijn PF, Bambang Oetomo S. Customized spectral band analysis compared with conventional Fourier analysis of heart rate variability in neonates. Physiol Meas 2004;25:1385-1395.
24. Nijhuis JG, Prechtl HF, Martin CB, Bots RS. Are there behavioural states in the human fetus? Early Hum Dev 1982;6:177-195.
25. Oostendorp TF, van Oosterom A, Jongsma HW. The effect of changes in the conductive medium on the fetal ECG throughout gestation. Clin Phys Physiol Meas 1989;10 Suppl B:11-20.
26. Assali NS, Brinkman CR, Woods JR, Dandavino A, Nuwayhid B. Development of neurohumoral control of fetal, neonatal, and adult cardiovascular functions. Am J Obstet Gynecol 1977;129: 748-759.
27. de Vries JI, Visser GH, Prechtl HF. The emergence of fetal behavior. I. Qualitative aspects. Early Hum dev 1982;7:301-322.
28. Divon MY, Yeh SY, Zimmer EZ, Platt LD, Paldi E, Paul RH. Respiratory sinus arrhythmia in the human fetus. Am J Obstet Gynecol 1985;151:425-428.
29. Ferrazzi E, Pardi G, Setti PL, Rodolfi M, Civardi S, Cerutti S. Power spectral analysis of the heart rate of the human fetus at 26 and 36 weeks of gestation. Clin Phys Physiol Meas 1989;10 Suppl B:57-60.
30. Natale R, Nasello-Paterson C, Connors G. Patterns of fetal breathing activity in the human fetus at 24 to 28 weeks of gestation. Am J Obstet Gynecol 1988;158:317-321.
31. ten Hof J, Nijhuis IJ, Mulder EJ, Nijhuis JG, Narayan H, Taylor DJ, Westers P, Visser GH. Longitudinal study of fetal body movements: nomograms, intrafetal consistency, and relationship with episodes of heart rate patterns a and B. Pediatr Res 2002;52:568-575.
32. Drogtrop AP, Ubels R, Nijhuis JG. The association between fetal body movements, eye movements and heart rate patterns in pregnancies between 25 and 30 weeks of gestation. Early Hum Dev 1990;23:67-73.
33. Nijhuis IJ, ten Hof J, Nijhuis JG, Mulder EJ, Narayan H, Taylor DJ, Visser GH. Temporal organization of fetal behavior from 24-weeks gestation onwards in normal and complicated pregnancies. Dev Psychobiol 1999;34:257-268.
34. Pillai M, James D. Behavioural states in normal mature human fetuses. Arch Dis Child 1990;65: 39-43.

Bibliography

[1] A.K Sundström, D. Rosén, and K. G. Rosén, *Fetal surveillance*, Neoventa Medical AB, 2002.

[2] M. De Haan, J. S. Wyatt, S. Roth, F. Vargha-Khadem, D. Gadian, and M. Mishkin, "Brain and cognitive-behavioural development after asphyxia at term birth.," *Dev Sci*, vol. 9, no. 4, pp. 350–358, Jul 2006.

[3] R. Victory, D. Penava, O. Da Silva, R. Natale, and B. Richardson, "Umbilical cord ph and base excess values in relation to adverse outcome events for infants delivering at term.," *Am J Obstet Gynecol*, vol. 191, no. 6, pp. 2021–2028, Dec 2004.

[4] A. Martín-Ancel, A. Garca-Alix, F. Gay, F. Cabaas, M. Burgueros, and J. Quero, "Multiple organ involvement in perinatal asphyxia.," *J Pediatr*, vol. 127, no. 5, pp. 786–793, Nov 1995.

[5] W.M. Callaghan, M.F. MacDorman, S.A. Rasmussen, C. Qin, and E.M. Lackritz, "The contribution of preterm birth to infant mortality rates in the united states.," *Pediatrics*, vol. 118, no. 4, pp. 1566–1573, Oct 2006.

[6] J. A. Low, B. G. Lindsay, and E. J. Derrick, "Threshold of metabolic acidosis associated with newborn complications.," *Am J Obstet Gynecol*, vol. 177, no. 6, pp. 1391–1394, Dec 1997.

[7] Z. Alfirevic, D. Devane, and G M L. Gyte, "Continuous cardiotocography (ctg) as a form of electronic fetal monitoring (efm) for fetal assessment during labour.," *Cochrane Database Syst Rev*, , no. 3, pp. CD006066, 2006.

[8] P. V. Nielsen, B. Stigsby, C. Nickelsen, and J. Nim, "Intra- and inter-observer variability in the assessment of intrapartum cardiotocograms.," *Acta Obstet Gynecol Scand*, vol. 66, no. 5, pp. 421–424, 1987.

[9] K.G. Rosén and R. Luzietti, "Intrapartum fetal monitoring: its basis and current developments.," *Prenatal and Neonatal Medicine*, vol. 5, pp. 155–68, 2000.

[10] D. C. Young, J. H. Gray, E. R. Luther, and L. J. Peddle, "Fetal scalp blood ph sampling: its value in an active obstetric unit.," *Am J Obstet Gynecol*, vol. 136, no. 3, pp. 276–281, Feb 1980.

[11] A.A. Mahendru and C.C. Lees, "Is intrapartum fetal blood sampling a gold standard diagnostic tool for fetal distress?," *Eur J Obstet Gynecol Reprod Biol*, vol. 156, no. 2, pp. 137–139, Jun 2011.

[12] K. R. Greene, G. S. Dawes, H. Lilja, and K. G. Rosn, "Changes in the st waveform of the fetal lamb electrocardiogram with hypoxemia.," *Am J Obstet Gynecol*, vol. 144, no. 8, pp. 950–958, Dec 1982.

[13] K. G. Rosén, K. H. Hkegrd, and I. Kjellmer, "A study of the relationship between the electrocardiogram and hemodynamics in the fetal lamb during asphyxia.," *Acta Physiol Scand*, vol. 98, no. 3, pp. 275–284, Nov 1976.

[14] K. H. Hökegård, B. O. Eriksson, I. Kjellmer, R. Magno, and K. G. Rosn, "Myocardial metabolism in relation to electrocardiographic changes and cardiac function during graded hypoxia in the fetal lamb.," *Acta Physiol Scand*, vol. 113, no. 1, pp. 1–7, Sep 1981.

[15] J. A. Westgate, L. Bennet, C. Brabyn, C. E. Williams, and A. J. Gunn, "St waveform changes during repeated umbilical cord occlusions in near-term fetal sheep.," *Am J Obstet Gynecol*, vol. 184, no. 4, pp. 743–751, Mar 2001.

[16] K. H. Hökegård, K. Karlsson, I. Kjellmer, and K. G. Rosén, "Ecg-changes in the fetal lamb during asphyxia in relation to beta-adrenoceptor stimulation and blockade.," *Acta Physiol Scand*, vol. 105, no. 2, pp. 195–203, Feb 1979.

[17] James P. Neilson, "Fetal electrocardiogram (ecg) for fetal monitoring during labour.," *Cochrane Database Syst Rev*, vol. 4, pp. CD000116, 2012.

[18] I. Amer-Wahlin, S. Arulkumaran, H. Hagberg, K. Marsl, and G H A. Visser, "Fetal electrocardiogram: St waveform analysis in intrapartum surveillance.," *BJOG*, vol. 114, no. 10, pp. 1191–1193, Oct 2007.

[19] A. Kwee, A.H.S. Dekkers, H.P.J. van Wijk, C.W. van der Hoorn-van den Beld, and G.H.A. Visser, "Occurrence of st-changes recorded with the stan s21-monitor during normal and abnormal fetal heart rate patterns during labour.," *Eur J Obstet Gynecol Reprod Biol*, vol. 135, no. 1, pp. 28–34, Nov 2007.

[20] G. S. Dawes, M. Moulden, and C. W. Redman, "The advantages of computerized fetal heart rate analysis.," *J Perinat Med*, vol. 19, no. 1-2, pp. 39–45, 1991.

[21] R. H. Paul, A. K. Suidan, S. Yeh, B. S. Schifrin, and E. H. Hon, "Clinical fetal monitoring. vii. the evaluation and significance of intrapartum baseline fhr variability.," *Am J Obstet Gynecol*, vol. 123, no. 2, pp. 206–210, Sep 1975.

[22] F. Rochard, B. S. Schifrin, F. Goupil, H. Legrand, J. Blottiere, and C. Sureau, "Nonstressed fetal heart rate monitoring in the antepartum period.," *Am J Obstet Gynecol*, vol. 126, no. 6, pp. 699–706, Nov 1976.

[23] K.P. Williams and F. Galerneau, "Intrapartum fetal heart rate patterns in the prediction of neonatal acidemia.," *Am J Obstet Gynecol*, vol. 188, no. 3, pp. 820–823, Mar 2003.

[24] C. M. van Ravenswaaij-Arts, L. A. Kolle, J. C. Hopman, G. B. Stoelinga, and H. P. van Geijn, "Heart rate variability.," *Ann Intern Med*, vol. 118, no. 6, pp. 436–447, Mar 1993.

[25] "Heart rate variability: standards of measurement, physiological interpretation and clinical use. task force of the european society of cardiology and the north american society of pacing and electrophysiology.," *Circulation*, vol. 93, no. 5, pp. 1043–1065, Mar 1996.

[26] J.R. Huey, Jr, R.H. Paul, A.A. Hadjiev, J. Jilek, and E.H. Hon, "Fetal heart rate variability: an approach to automated assessment.," *Am J Obstet Gynecol*, vol. 134, no. 6, pp. 691–695, Jul 1979.

[27] D. Maulik, V. Saini, and S. T. Zigrossi, "Clinical significance of short-term variability computed from heart-rate waveforms.," *J Perinat Med*, vol. 11, no. 5, pp. 243–248, 1983.

[28] J.O.E.H. van Laar, C.H.L. Peters, R. Vullings, S. Houterman, J.W.M. Bergmans, and S. G. Oei, "Fetal autonomic response to severe acidaemia during labour.," *BJOG*, vol. 117, no. 4, pp. 429–437, Mar 2010.

[29] J.O.E.H. van Laar, C.H.L. Peters, S. Houterman, P.F.F. Wijn, A. Kwee, and S.G. Oei, "Normalized spectral power of fetal heart rate variability is associated with fetal scalp blood ph.," *Early Hum Dev*, vol. 87, no. 4, pp. 259–263, Apr 2011.

[30] P. Van Leeuwen, D. Geue, S. Lange, W. Hatzmann, and D. Grnemeyer, "Changes in the frequency power spectrum of fetal heart rate in the course of pregnancy.," *Prenat Diagn*, vol. 23, no. 11, pp. 909–916, Nov 2003.

[31] M. David, M. Hirsch, J. Karin, E. Toledo, and S. Akselrod, "An estimate of fetal autonomic state by time-frequency analysis of fetal heart rate variability.," *J Appl Physiol*, vol. 102, no. 3, pp. 1057–1064, Mar 2007.

[32] J. Karin, M. Hirsch, and S. Akselrod, “An estimate of fetal autonomic state by spectral analysis of fetal heart rate fluctuations.,” *Pediatr Res*, vol. 34, no. 2, pp. 134–138, Aug 1993.

[33] M. Pillai and D. James, “The development of fetal heart rate patterns during normal pregnancy.,” *Obstet Gynecol*, vol. 76, no. 5 Pt 1, pp. 812–816, Nov 1990.

[34] J.O.E.H. van Laar, C.H.L. Peters, R. Vullings, S. Houterman, and S.G. Oei, “Power spectrum analysis of fetal heart rate variability at near term and post term gestation during active sleep and quiet sleep.,” *Early Hum Dev*, vol. 85, no. 12, pp. 795–798, Dec 2009.

[35] G.D. Clifford and L. Tarassenko, “Quantifying errors in spectral estimates of hrv due to beat replacement and resampling.,” *IEEE Trans Biomed Eng*, vol. 52, no. 4, pp. 630–638, Apr 2005.

[36] C.H.L. Peters, R. Vullings, J.W.M. Bergmans, S.G. Oei, and P.F.F. Wijn, “The effect of artifact correction on spectral estimates of heart rate variability.,” *Conf Proc IEEE Eng Med Biol Soc*, vol. 2008, pp. 2669–2672, 2008.

[37] G. Baule and R. McFee, “Detection of the magnetic field of the heart.,” *Am Heart J*, vol. 66, pp. 95–96, Jul 1963.

[38] V. Kariniemi, J. Ahopelto, P. J. Karp, and T. E. Katila, “The fetal magnetocardiogram.,” *J Perinat Med*, vol. 2, no. 3, pp. 214–216, 1974.

[39] R. E. Myers, “Two patterns of perinatal brain damage and their conditions of occurrence.,” *Am J Obstet Gynecol*, vol. 112, no. 2, pp. 246–276, Jan 1972.

[40] K. G. Rosén and I. Kjellmer, “Changes in the fetal heart rate and ecg during hypoxia.,” *Acta Physiol Scand*, vol. 93, no. 1, pp. 59–66, Jan 1975.

[41] G.W. Lawson, R. Belcher, G.S Dawes, and C.W. Redman, “A comparison of ultrasound (with autocorrelation) and direct electrocardiogram fetal heart rate detector systems,” *Am J Obstet Gynecol*, vol. 147, no. 6, pp. 721–722, Nov 1983.

[42] T. Fukushima, C. A. Flores, E. H. Hon, and EC Davidson, Jr, “Limitations of autocorrelation in fetal heart rate monitoring.,” *Am J Obstet Gynecol*, vol. 153, no. 6, pp. 685–692, Nov 1985.

[43] M. Peters, J. Crowe, J. F. Piri, H. Quartero, B. Hayes-Gill, D. James, J. Stinstra, and S. Shakespeare, “Monitoring the fetal heart non-invasively: a review of methods.,” *J Perinat Med*, vol. 29, no. 5, pp. 408–416, 2001.

[44] T. F. Oostendorp, A. van Oosterom, and H. W. Jongsma, “Electrical properties of tissues involved in the conduction of foetal ecg.,” *Med Biol Eng Comput*, vol. 27, no. 3, pp. 322–324, May 1989.

[45] J. G. Stinstra and M. J. Peters, “The volume conductor may act as a temporal filter on the ecg and eeg.,” *Med Biol Eng Comput*, vol. 36, no. 6, pp. 711–716, Nov 1998.

[46] J. A. Crowe, M. S. Woolfson, B. R. Hayes-Gill, W. Peasgood, M. A. Mohd-Ali, Y. Huang, J. Herbert, X. B. Huang, A. Harrison, N. M. Gibson, E. M. Symonds, N. Reed, and M. Mohajer, “Antenatal assessment using the fecg obtained via abdominal electrodes.,” *J Perinat Med*, vol. 24, no. 1, pp. 43–53, 1996.

[47] J. F. Piri, J. A. Crowe, B. R. Hayes-Gill, C. J. Spencer, K. Bhogal, and D. K. James, “Compact long-term recorder for the transabdominal foetal and maternal electrocardiogram.,” *Med Biol Eng Comput*, vol. 39, no. 1, pp. 118–125, Jan 2001.

[48] R. Vullings, C.H.L. Peters, R.J. Sluijter, M. Mischi, S.G. Oei, and J.W.M. Bergmans, “Dynamic segmentation and linear prediction for maternal ecg removal in antenatal abdominal recordings.,” *Physiol Meas*, vol. 30, no. 3, pp. 291–307, Mar 2009.

[49] R. Vullings, C.H.L. Peters, M.J.M. Hermans, P.F.F. Wijn, S.G. Oei, and J.W.M. Bergmans, “A robust physiology-based source separation method for qrs detection in low amplitude fetal ecg recordings.,” *Physiol Meas*, vol. 31, no. 7, pp. 935–951, Jul 2010.

[50] R. Vulling, *Non-invasive fetal electrocardiogram: analysis and interpretation*, Ph.D. thesis, Technische Universiteit Eindhoven, The Netherlands, 2010.

[51] M.J. Rooijakkers, C. Rabotti, S.G. Oei, and M. Mischi, “Low-complexity r-peak detection for ambulatory fetal monitoring.,” *Physiol Meas*, vol. 33, no. 7, pp. 1135–1150, Jul 2012.

[52] A.C. Guyton and J.E. Hall, *Textbook of Medical Physiology*, W.B. Saunders complany,Philidelphia, USA, 10 edition, 2000.

[53] J.A. Bernhards and L.N. Bouman, *Fysiologie van de mens*, Bohn Stafleu Van Loghum, 6 edition, 1994.

[54] G. Mielke and N. Benda, “Cardiac output and central distribution of blood flow in the human fetus.,” *Circulation*, vol. 103, no. 12, pp. 1662–1668, Mar 2001.

[55] N.P. Depasquale and G.E. Burch, "The electrocardiogram, ventricular gradient and spatial vectorcardiogram during the first week of life.," *Am J Cardiol*, vol. 12, pp. 482–493, Oct 1963.

[56] M. Artman, L. Mahony, and D.F. Teitel, *Neonatal cardiology*, McGraw-Hill companies, USA, 2002.

[57] S. Yagel, N.H. Silverman, and U. Gemburch, *Fetal cardiology: embryology, genetics, physiology, echocardiographic evaluation, diagnosis and perinatal management of cardiac diseases*, Informa Healthcare Inc, New York, USA, 2 edition, 2009.

[58] J. Stinstra, *Reliability of the fetal magnetocardiogram*, Ph.D. thesis, Universiteit Twente, Enschede, The Netherlands, 2001.

[59] T.G. Laske and P.A. Iaizzo, *The Cardiac Conduction System. In: Handbook of cardiac anatomy, physiology, and devices.*, Humana Press, 2005.

[60] T.G. Laske and P.A. Iaizzo, *Handbook of Cardiac Anatomy, Physiology, and Devices: The cardiac conduction system*, Humana Press,, 2005.

[61] D.B. Geselowitz, "Dipole theory in electrocardiography.," *Am J Cardiol*, vol. 14, pp. 301–306, Sep 1964.

[62] H. C. Burger and J. B. Van Milaan, "Heart-vector and leads," *Br Heart J*, vol. 8, no. 3, pp. 157–161, Jul 1946.

[63] E. Frank, "General theory of heat-vector projection.," *Circ Res*, vol. 2, no. 3, pp. 258–270, May 1954.

[64] J. Malmivuo and R. Plonsey, *Bioelectromagnetism principles and applications of bioelectric and biomagnetic fields*, Oxford University Press,New York, 1995.

[65] W. Einthoven, "Weiteres ber das elecktrokardiogram," *Pflger Arch ges Physiol*, vol. 122, pp. 517–48, 1908.

[66] T.F. Oostendorp, *Modeeling the foetal ECG*, Ph.D. thesis, K.U.Nijmegen, The Netherlands, 1989.

[67] T. F. Oostendorp, A. van Oosterom, and H. W. Jongsma, "The effect of changes in the conductive medium on the fetal ecg throughout gestation.," *Clin Phys Physiol Meas*, vol. 10 Suppl B, pp. 11–20, 1989.

[68] R. A. Brace and E. J. Wolf, “Normal amniotic fluid volume changes throughout pregnancy.,” *Am J Obstet Gynecol*, vol. 161, no. 2, pp. 382–388, Aug 1989.

[69] E. F. Magann, J. D. Bass, S. P. Chauhan, R. A. Young, N. S. Whitworth, and J. C. Morrison, “Amniotic fluid volume in normal singleton pregnancies.,” *Obstet Gynecol*, vol. 90, no. 4 Pt 1, pp. 524–528, Oct 1997.

[70] P. N. Baker, I. R. Johnson, P. A. Gowland, J. Hykin, V. Adams, P. Mansfield, and B. S. Worthington, “Measurement of fetal liver, brain and placental volumes with echo-planar magnetic resonance imaging.,” *Br J Obstet Gynaecol*, vol. 102, no. 1, pp. 35–39, Jan 1995.

[71] J. T. Oldenburg and M. Macklin, “Changes in the conduction of the fetal electrocardiogram to the maternal abdominal surface during gestation.,” *Am J Obstet Gynecol*, vol. 129, no. 4, pp. 425–433, Oct 1977.

[72] H. E. Cohn, E. J. Sacks, M. A. Heymann, and A. M. Rudolph, “Cardiovascular responses to hypoxemia and acidemia in fetal lambs.,” *Am J Obstet Gynecol*, vol. 120, no. 6, pp. 817–824, Nov 1974.

[73] L. L. Peeters, R. E. Sheldon, MD Jones, Jr, E. L. Makowski, and G. Meschia, “Blood flow to fetal organs as a function of arterial oxygen content.,” *Am J Obstet Gynecol*, vol. 135, no. 5, pp. 637–646, Nov 1979.

[74] M. Hanson and P. Kumar, “Chemoreceptor function in the fetus and neonate.,” *Adv Exp Med Biol*, vol. 360, pp. 99–108, 1994.

[75] J. L. Evers, J. De Haan, H. W. Jongsma, A. J. Crevels, T. H. Arts, and CB Martin, Jr, “The preejection period of the fetal cardiac cycle. i. umbilical cord occlusions.,” *Eur J Obstet Gynecol Reprod Biol*, vol. 11, no. 6, pp. 401–418, May 1981.

[76] J. T. Parer, *Handbook of fetal heart rate monitoring*, WB Saunders, Philadelphia, USA, 2009.

[77] H. Asano, J. Homan, L. Carmichael, S. Korkola, and B. Richardson, “Cerebral metabolism during sustained hypoxemia in preterm fetal sheep.,” *Am J Obstet Gynecol*, vol. 170, no. 3, pp. 939–944, Mar 1994.

[78] B. S. Richardson, L. Carmichael, J. Homan, L. Johnston, and R. Gagnon, “Fetal cerebral, circulatory, and metabolic responses during heart rate decelerations with umbilical cord compression.,” *Am J Obstet Gynecol*, vol. 175, no. 4 Pt 1, pp. 929–936, Oct 1996.

[79] R.M. Berne and M.N. Levy, *The autonomic nervous system and its central control*, Mosby Inc., St Louis, USA, 4 edition, 1998.

[80] S. Akselrod, D. Gordon, J. B. Madwed, N. C. Snidman, D. C. Shannon, and R. J. Cohen, "Hemodynamic regulation: investigation by spectral analysis.," *Am J Physiol*, vol. 249, no. 4 Pt 2, pp. H867–H875, Oct 1985.

[81] R.M. Berne and M.N. Levy, *Regulation of the heartbeat*, Mosby Inc., St Louis, USA, 4 edition, 1998.

[82] A. J. Pappano, "Ontogenetic development of autonomic neuroeffector transmission and transmitter reactivity in embryonic and fetal hearts.," *Pharmacol Rev*, vol. 29, no. 1, pp. 3–33, Mar 1977.

[83] D. Walker, "Functional development of the autonomic innervation of the human fetal heart.," *Biol Neonate*, vol. 25, no. 1-2, pp. 31–43, 1974.

[84] B. Nuwayhid, C.R. Brinkman, 3rd, C. Su, J. A. Bevan, and N. S. Assali, "Development of autonomic control of fetal circulation.," *Am J Physiol*, vol. 228, no. 2, pp. 337–344, Feb 1975.

[85] N. S. Assali, C.R. Brinkman, 3rd, JR Woods, Jr, A. Dandavino, and B. Nuwayhid, "Development of neurohumoral control of fetal, neonatal, and adult cardiovascular functions.," *Am J Obstet Gynecol*, vol. 129, no. 7, pp. 748–759, Dec 1977.

[86] J. Itskovitz, E. F. LaGamma, and A. M. Rudolph, "Heart rate and blood pressure responses to umbilical cord compression in fetal lambs with special reference to the mechanism of variable deceleration.," *Am J Obstet Gynecol*, vol. 147, no. 4, pp. 451–457, Oct 1983.

[87] I. J. Nijhuis, J. ten Hof, J. G. Nijhuis, E. J. Mulder, H. Narayan, D. J. Taylor, and G. H. Visser, "Temporal organization of fetal behavior from 24-weeks gestation onwards in normal and complicated pregnancies.," *Dev Psychobiol*, vol. 34, no. 4, pp. 257–268, May 1999.

[88] M.E.M.H. Westerhuis, A. Kwee, A. A. van Ginkel, A. P. Drogtrop, W.J.A. Gyselaers, and G.H.A. Visser, "Limitations of st analysis in clinical practice: three cases of intrapartum metabolic acidosis.," *BJOG*, vol. 114, no. 10, pp. 1194–1201, Oct 2007.

[89] J. G. Nijhuis, H. F. Prechtl, CB Martin, Jr, and R. S. Bots, "Are there behavioural states in the human fetus?," *Early Hum Dev*, vol. 6, no. 2, pp. 177–195, Apr 1982.

[90] M. Pillai and D. James, “Behavioural states in normal mature human fetuses.,” *Arch Dis Child*, vol. 65, no. 1 Spec No, pp. 39–43, Jan 1990.

[91] E. J. Mulder, G. H. Visser, D. J. Bekedam, and H. F. Prechtl, “Emergence of behavioural states in fetuses of type-1-diabetic women.,” *Early Hum Dev*, vol. 15, no. 4, pp. 231–251, Jul 1987.

[92] C.H.L. Peters, R. Vullings, J.W.M. Bergmans, S.G. Oei, and P.F.F. Wijn, “Heart rate detection in low amplitude non-invasive fetal ecg recordings.,” *Conf Proc IEEE Eng Med Biol Soc*, vol. 1, pp. 6092–6094, 2006.

[93] M. Kotas, J. Jezewski, T. Kupka, and K. Horoba, “Detection of low amplitude fetal qrs complexes.,” *Conf Proc IEEE Eng Med Biol Soc*, vol. 2008, pp. 4764–4767, 2008.

[94] S. Abboud and D. Sadeh, “Spectral analysis of the fetal electrocardiogram.,” *Comput Biol Med.*, vol. 19, no. 6, pp. 409–415, 1989.

[95] E.C. Karvounis, M.G. Tsipouras, and D.I. Fotiadis, “Detection of fetal heart rate through 3-D phase space analysis from multivariate abdominal recordings,” *IEEE Trans Biomed Eng*, vol. 56, no. 5, pp. 1394–406, May 2009.

[96] S. Waldert, M. Bensch, M. Bogdan, W. Rosenstiel, B. Schölkopf, C.L. Lowery, H. Eswaran, and H. Preissl, “Real-time fetal heart monitoring in biomagnetic measurements using adaptive real-time ICA,” *IEEE Trans Biomed Eng*, vol. 54, no. 10, pp. 1867–1874, Oct 2007.

[97] G.E. Dower, H.B. Machada, and J.A. Osborne, “On deriving the electrocardiogram from vectorcardiographic leads,” *Clin Cardiol*, vol. 3, pp. 87–95, 1980.

[98] K.G. Rosén, A. Dagbjartsson, B.A. Henriksson, H. Lagercrantz, and I. Kjellmer, “The relationship between circulating catecholamines and ST waveform in the fetal lamb electrocardiogram during hypoxia,” *Am J Obstet Gynecol*, vol. 149, no. 2, pp. 190–5, May 1984.

[99] S.J. Ahn, W. Rauh, and H.-J. Warnecke, “Least-squares orthogonal distances fitting of circle, sphere, ellipse, hyperbola, and parabola,” *Pattern Recognition*, vol. 34, pp. 2283–2303, 2001.

[100] C.H.L. Peters, R. Vullings, M.J. Rooijakkers, J.W.M. Bergmans, S.G. Oei, and P.F.F. Wijn, “A continuous wavelet transform-based method for time-frequency analysis of artefact-corrected heart rate variability data.,” *Physiol Meas*, vol. 32, no. 10, pp. 1517–1527, Oct 2011.

[101] B. Köhler, C. Hennig, and R. Orglmeister, “The principles of software qrs detection.,” *IEEE Eng Med Biol Mag*, vol. 21, no. 1, pp. 42–57, 2002.

[102] J. Stinstra, E. Golbach, P. van Leeuwen, S. Lange, T. Menendez, W. Moshage, E. Schleussner, C. Kaehler, H. Horigome, S. Shigemitsu, and M.J. Peters, “Multicentre study of fetal cardiac time intervals using magnetocardiography,” *BJOG*, vol. 109, pp. 1235–1243, Nov. 2002.

[103] I.E.G. Richardson, *H.264 and MPEG-4 Video Compression: Video Coding for Next-generation Multimedia*, John Wiley & Sons Ltd, Chichester, 2003.

[104] C. Li, C. Zheng, and C. Tai, “Detection of ecg characteristic points using wavelet transforms.,” *IEEE Trans Biomed Eng*, vol. 42, no. 1, pp. 21–28, Jan 1995.

[105] P.S. Addison, *The Illustrated Wavelet Transform Handbook*, IOP Publishing Ltd, 2002.

[106] M.G.E. Schneiders, “Wavelets in control engineering,” M.S. thesis, Technische Universiteit Eindhoven, The Netherlands, 2001.

[107] R. Polikar, “The wavelet tutorial,” 1999.

[108] C.H.L. Peters, E.D.M. ten Broeke, P. Andriessen, B. Vermeulen, R.C.M. Berendsen, P.F.F. Wijn, and S.G. Oei, “Beat-to-beat detection of fetal heart rate: Doppler ultrasound cardiotocography compared to direct ecg cardiotocography in time and frequency domain.,” *Physiol Meas*, vol. 25, no. 2, pp. 585–593, Apr 2004.

[109] J.O.E.H. Van Laar, M.M. Porath, C.H.L. Peters, and S.G. Oei, “Spectral analysis of fetal heart rate variability for fetal surveillance: review of the literature.,” *Acta Obstet Gynecol Scand*, vol. 87, no. 3, pp. 300–306, 2008.

[110] U. Wiklund, M. Akay, and U. Niklasson, “Short-term analysis of heart-rate variability by adapted wavelet transforms.,” *IEEE Eng Med Biol Mag*, vol. 16, no. 5, pp. 113–8, 138, 1997.

[111] Y. Kimura, K. Okamura, T. Watanabe, N. Yaegashi, S. Uehara, and A. Yajima, “Time-frequency analysis of fetal heartbeat fluctuation using wavelet transform.,” *Am J Physiol*, vol. 275, no. 6 Pt 2, pp. H1993–H1999, Dec 1998.

[112] V. Pichot, J. M. Gaspoz, S. Molliex, A. Antoniadis, T. Busso, F. Roche, F. Costes, L. Quintin, J. R. Lacour, and J. C. Barthlmy, “Wavelet transform to quantify heart rate variability and to assess its instantaneous changes.,” *J Appl Physiol*, vol. 86, no. 3, pp. 1081–1091, Mar 1999.

[113] W. De Jong, *Blood pressure variability in neonates*, Ph.D. thesis, Technische Universiteit Eindhoven, The Netherlands, 2000.

[114] O. Rioul and Vetterli M., “Wavelets and signal processing,” *IEEE Signal Processing Magazine*, vol. 8, pp. 14–38, 1991.

[115] P. van Leeuwen, B. Hailer, W. Bader, J. Geissler, E. Trowitzsch, and D. H. Grnemeyer, “Magnetocardiography in the diagnosis of fetal arrhythmia.,” *Br J Obstet Gynaecol*, vol. 106, no. 11, pp. 1200–1208, Nov 1999.

[116] G.B. Moody, “Mit/bih arrhythmia database,” 1997.

[117] J.P.V. Madeiro, P.C. Cortez, F.I. Oliveira, and R.S. Siqueira, “A new approach to qrs segmentation based on wavelet bases and adaptive threshold technique.,” *Med Eng Phys*, vol. 29, no. 1, pp. 26–37, Jan 2007.

[118] C. Meyer, J. Fernndez Gavela, and M. Harris, “Combining algorithms in automatic detection of qrs complexes in ecg signals.,” *IEEE Trans Inf Technol Biomed*, vol. 10, no. 3, pp. 468–475, Jul 2006.

[119] C.H.L. Peters, *Time-scale analysis of antepartum fetal heart rate variability*, Ph.D. thesis, Technische Universiteit Eindhoven, The Netherlands, 2011.

[120] G.G. Landis, J.R.; Koch, “The measurement of observer agreement for categorical data,” *Biometrics*, vol. 33, pp. 159–174, 1977.

[121] J.L. Fleiss, *Statistical Methods for Rates and Proportions 2nd edition*, John Wiley & Sons, New York, USA, 1981.

[122] J. Pan and W. J. Tompkins, “A real-time qrs detection algorithm.,” *IEEE Trans Biomed Eng*, vol. 32, no. 3, pp. 230–236, Mar 1985.

[123] J.O.E.H. Van Laar, *Fetal autonomic cardiac response during pregnancy and labour*, Ph.D. thesis, Technische Universiteit Eindhoven, The Netherlands, 2012.

[124] M.J.M. Hermans, “Non-invasive fetal electrocardiogram classification using spatial correlation,” M.S. thesis, Eindhoven University of Technology, 2009.